INVESTIGATION OF SINGLE CRYSTAL DIAMOND FOR SWIFT HEAVY ION BEAM DETECTORS AND STUDY OF DIAMOND GROWTH FOR IMPROVEMENT OF DIAMOND MATERIAL FOR DETECTORS

By

Ayan Bhattacharya

A DISSERTATION

Submitted to
Michigan State University
in partial fulfillment of the requirements
for the degree of

Electrical Engineering—Doctor of Philosophy

2018

ABSTRACT

INVESTIGATION OF SINGLE CRYSTAL DIAMOND FOR SWIFT HEAVY ION BEAM DETECTORS AND STUDY OF DIAMOND GROWTH FOR IMPROVEMENT OF DIAMOND MATERIALS FOR DETECTORS

By

Ayan Bhattacharya

Diamond is a material with outstanding mechanical, electrical and optical properties. Single crystal diamond has a large bandgap (~ 5.47 eV), large atomic displacement energy (~ 43eV), high electric breakdown field (10^7 V cm^{-1}) and high thermal conductivity at room temperature. All these superior properties make diamond inherently a superb radiation tolerant material for harsh radiation environments.

In this study, single crystal diamond (scd) substrates grown at Michigan State University (MSU) by microwave plasma-assisted chemical vapor deposition (MPACVD) are tested to develop detectors for swift heavy ion beam. Prior to beam irradiation, the material properties of the diamond were characterized by UV-VIS spectroscopy and FTIR (Fourier Transform Infrared Spectroscopy). After fabrication of detectors, their performance was tested by irradiating with swift heavy ion (SHI) beams in the range of 100-150 MeV/u at the National Superconducting Cyclotron Laboratory (NSCL) at MSU. In addition to MSU grown samples, commercial electronic grade samples (Microwave Enterprises Ltd.) were also investigated under the same radiation environment.

Post irradiation, samples ware characterized by the transient current technique (TCT) to understand how charge transport properties get affected by the beam irradiation. The charge collection efficiency (CCE) and the lifetime of the holes and electrons created were studied. A completely non-irradiated commercially available electronic grade diamond was also tested in the

same testing configuration to generate a reference. Beam irradiated samples were also characterized by X-ray diffraction and Raman spectroscopy to characterize for any structural damage. The overall characterizations mostly confirmed a deterioration of charge transport properties. However, any evidence of substantial structural damage by the irradiation could not be found. One relevant observation was that the MSU lab grown diamond had a shorter carrier lifetime primarily due to more nitrogen impurities present in the grown diamond.

Next, to improve charge transport performance of MSU lab grown diamond substrates for electronic applications, single crystal diamond was deposited in a low nitrogen environment to grow thick layers ($\geq$ 200 μm). In general, epitaxial growth on surface close to the (001) crystallographic plane at a low nitrogen environment often suffers from defects forming on the surface. Such defects arise from dislocations (already present in the substrate), twining during the growth process. A possible solution to this issue is to grow samples on misoriented substrates (i.e. on surfaces that are slightly tilted from the (001) plane). The resulting surface profile largely depends on the growth condition (i.e. temperature, pressure, methane concentration), as well as the substrate misorientation angle. The deposition on a misoriented surface happens with a step flow growth process. It is found in research literature that impurities present in the deposition gas generally tend to concentrate at steps more than on terrace. Hence the spatial size of the step height and terrace width distribution produced as a result of misorientation angle variation is important for the quality of the deposited diamond. A detailed study of the distribution of step height and terrace width with respect to misorientation angle for thick layers (~ 200 μm) was performed. The step height and terrace width distributions can help decide the selection of offcut angle, doping concentration and growth layer thickness, which otherwise may create localized and non-uniform distribution of impurities and non-uniform breakdown electric fields.

ACKNOWLEDGEMENTS

I would like to begin with expressing my sincere appreciation and gratitude to my major advisor Dr. Timothy A. Grotjohn for providing me with this opportunity and his mentorship and support in this journey of my PhD. His patience and thoughtful suggestions always helped me to keep things rolling when everything appeared to hit almost a dead end. Next, I would like to extend my thanks to Dr. Andreas Stolz, one of my committee members, for his guidance and help to conduct my most important experiments. Without his strong support, this work could not have been accomplished. I would also like to thank my other committee members, Dr. Timothy P. Hogan and Dr. Qi Hua Fan, for their valuable advices and suggestions. I would also like to thank National Superconducting Cyclotron Laboratory (NSCL) at Michigan State University (MSU) for providing me their outstanding facility to conduct some experiments, which are the integral part of my PhD dissertation.

I would also like to extend my sincere thanks to Dr. Jes Asmussen for his valuable suggestions and guidance during my exploration of the interesting and exciting work of single crystal diamond deposition. I am also thankful to Dr. Donnie Reinhard for being in my committee for few years before his retirement.

My sincere appreciation also goes to Dr. Per Askeland of Composite Material and structure center (CMSC), MSU and Dr. Baokang Bi of W. M. Keck Microfabrication Facility at MSU for their valuable guidance in operating different instrument for characterization. My sincere thanks are also extended to Mr. Brian Wright and Mr. Karl Dersch for their help in troubleshooting and fixing complex technical issues in the CVD reactors. Last but not the least, I am also thankful to all the fellow graduate students and colleagues at Fraunhofer CCD, USA.

Finally, this work could not have been completed without the unconditional support of my family members, my in-laws, especially my wife Dr. Aparajita Banerjee for her support to fight and handle all the extreme stressful moments during this journey. I do not have any words to express my gratitude to my late mother, who had been my strong pillar of support, however, could not witness the end of this long journey. I would like to thank all my friends within and outside MSU for the important role they played in this journey.

TABLE OF CONTENTS

LIST OF TABLES

LIST OF FIGURES

KEY TO ABBREVIATIONS

AFM	Atomic force microscopy
CCD	Charge collection distance
CERN	European Organization for Nuclear Research
CMS	Compact muon solenoid
CVD	Chemical vapor deposition
DF	Dark field
DICM	Differential interference contrast imaging
FH	Flat head hillocks
FTIR	Fourier-transform infrared
FWHM	Full width half maximum
HFCVD	Hot filament chemical vapor deposition
HL-LHC	High Luminosity Large Hadron Collider
HPHT	High pressure high temperature
HPMS	High Pressure Microwave Source
HRXRD	High resolution X-ray diffraction
IBIC	Ion beam induced current
LED	Light emitting diaode
LHC	Large Hadron Collider
MCPR	Microwave cavity plasma reactor
MFC	Mass flow controllers
MIP	Minimum ionizing particles
MPACVD	Microwave plasma assisted chemical vapor deposition

NIRIM	National Institute for Research in Inorganic Materials
NSCL	National Superconducting Cyclotron Laboratory
PACVD	Plasma Assisted Chemical Vapor Deposition
pcd	Polycrystalline diamond
pCVD	Polycrystalline chemical vapor deposition
PECVD	Plasma enhanced chemical vapor deposition
PH	Pyramidal hillocks
scCVD	Single crystal chemical vapor deposition
scd	Single crystal diamonds
SHI	Swift heavy ion
TCT	Transient current technique
TE	Transverse electric
TEM	Transmission electron microscopy
TM	Transverse magnetic
UC	unepitaxial crystals
UV-VIS	ultra violet-visible

Chapter 1. Introduction

1.1 Research motivation

Carbon has many different allotropes out of which diamond stands as the most cherished one among all due to its forever high demand and popularity. The sp^3 bonding of carbon atoms in diamond attributes to its several extreme properties in terms of electrical, mechanical or thermal behavior. It is one of the hardest and most chemically inert materials. Diamond has become a true engineering material with many of its electronic properties superior in comparison to some other contemporary electronic materials. It is already being steadily explored in the domain of power electronics and heat sinks, as diamond-based devices can be operated with minimal cooling or without additional cooling. However even with many potential advantages, the cost of production and a reliable quality control of diamond substrates still limits diamond in comparison with the well-established silicon-based technology. Natural diamond already carries a great cost with it due to the complexity of excavation and related costs and limited worldwide resources. Hence their application hardly expanded outside the jewelry business. It was only after many decades of trials and failures, that the first reliable report from General Electric Company from Schenectady, New York in 1954 showed a pathway towards producing lab grown diamonds and opened a platform towards engineering applications of diamond [1].

In the last couple of decades, diamond has emerged as a semiconductor material. At present, industrial applications of diamond ranges beyond its traditional application as abrasives to the fields of optics, RF MEMS technology, heat sinks, power electronics and high energy particle detectors [2].

The first diamond synthesis process mimicked the natural process of diamond growth, i.e. carbon was crystallized into diamond at a pressure of 70 Kbar/inch^2 and a temperature close to 2500 °C by using a belt press. This technique evolved as the "High Pressure High Temperature (HPHT)" method of diamond growth. Diamond growth technology has gone through many transformations and advancements. Currently, the microwave plasma assisted chemical vapor deposition (MPACVD) technique stands as a very efficient and popular method of diamond growth for the highest quality diamond.

Although advancement of diamond growth still has many obstacles to overcome to make diamond based electronic devices scalable for mass production, there are a few areas where diamond has already shown superiority and radiation detectors for high energy particles is one such case. This application of diamond is based upon the inherent strength of sp^3 bonds in the diamond crystal structure, and the related high radiation hardness of diamond, something which silicon-based technology does not offer. As silicon is not as radiation hard as diamond, beyond a certain harsh radiation environment threshold the well-established Si based detection systems need to be upgraded by relatively new diamond-based detection systems. Some studies on diamond based detection systems at CERN (European Nuclear Research Center, Geneva, Switzerland) have already shown promise that diamond-based detectors will survive in harsh environments for years [3]. This has generated many collaborations between industry and particle physics groups to come up with a special quality of diamond called “detector grade" diamonds, which can offer almost 100% charge collection at the initial stage of irradiation. It is already an accepted fact that diamond`s extreme radiation hardness will be a great advantage to push the limit of higher particle energy and fluence. Hence in the near future at CERN the target is to push the integrated luminosity by two orders of magnitude higher than its current state [4]. This higher luminosity is a challenge

for detectors which need to survive fluences of 1 MeV neutron equivalent on the order 10^{16} cm^{-2} [5]. Diamond with its higher radiation hardness is expected to meet such challenges.

As it is important to understand the performance of diamond detectors in radiation harsh environments over a long-time frame, it is also important to know the lifespan and process of degradation of detectors in different types of high energy beams, especially the physical state of the material diamond after being exposed to heavy ion irradiation for a prolong time. The RD42 collaboration at CERN has made some significant studies over the last two decades to understand such phenomena. Some of their extensive study shows the change in detector properties under different energies of proton and neutron beams. However, a global parametric distribution is still hard to establish as the material degradation at different energy regimes requires different physical models for explanation. In this proposed study one of the main goals is to look at how single crystal diamond degrades in swift heavy ion (SHI) beams [6] generated at the National Superconducting Cyclotron Laboratory (NSCL) at Michigan State University. In this type of beam, it is the mass of the particle together with the kinetic energy and finally the charged state of the particles that determines the interaction of the particles with the diamond detector material.

The major goal of this work has been dedicated in understanding how the quality of diamond material affects the radiation induced degradation process. Although higher quality of diamond (with very low nitrogen impurities) is always desired for any electronic applications, the cost of such diamond plates are very high. Therefore, comparisons of performance have been made between commercially available electronic grade diamond and lab grown diamonds at MSU to establish a more cost-effective research pathway on detectors. However due to presence of much higher nitrogen impurities in some of our own lab grown diamonds, the lifetime of the hole and

electron carriers generated by high energy particles was shorter than in lower nitrogen impurities diamond substrates.

As a next step to upgrade the MSU lab grown diamonds work was performed to establish diamond growth in a low nitrogen environment. However, growing thick diamond plates using a homoepitaxial process in a low nitrogen environment with a top growth surface close to [001] crystallographic plane is a challenge. Several research literatures show that controlling defects generated from dislocations and associated twinning is an extensive challenge when growth is done with a low nitrogen impurity level. As a method to overcome this problem misoriented substrates (with misorientation angle from the (100) plane along either the [100] or [110] directions) are used to deposit single crystal diamond, which allows step flow growth across the surface. However, a selection of the growth condition (feed gas ratio, temperature, etc.) combined with selection of the misoriented angle has a strong influence in the appearance of the top growth surface during deposition and the final surface structure, i.e. the surface has steps and terraces in the order of nanometers to micrometers dimensions. Therefore, it is important to have an idea of step height and terrace width distribution with respect to misorientation angle because the incorporation of impurities is higher in the step regions. This can also play a crucial role when selective impurity/dopant are added to feed-gas to create p-type or n-type diamond. Hence a second major part of this thesis explores systematically the step height and terrace width distribution with varied misorientation angle for a set of growth condition in MPACVD diamond deposition.

1.2. Objectives

The purpose of this study was to investigate and improve the performance of single crystal diamond detectors in swift heavy ion (SHI) beams. A focus of this study is understanding the

material degradation of the detectors after a high flux of SHI particle irradiation in the energy range of 120 MeV/u. The key objectives are:

- Quantify and understand the performance of diamond detectors made from both MSU lab grown and commercial electronic grade diamonds. This study serves a purpose of understanding the use of CVD grown diamond of various qualities for SHI beam detection.
- Quantify the lifetime of diamond detectors for SHI beam detection and to understand their eventual degradation. An important aspect of this work is to predict the typical span of time that these detectors can produce a reasonable quality of detection signal. A study of the detector`s output at different fluences of high energy particles is used as an estimation for life span prediction.
- Measure the effect of SHI beam irradiation on the electrical, optical and structural properties of the diamonds. The effect of irradiation on diamond material is determined by the energy and type of the beam and the type of interaction that goes on inside the material. This work looks to understand the type of the degradation that happens in the diamond detectors.
- Explore pathways of improvement in lab grown diamond for detector applications. It is always desired to have a diamond with very low impurities and minimal defects for detectors. Specifically, both low impurity levels and minimal defects enhances the charge collection distance of the diamond detector. However, for lab grown diamonds, it is still a great challenge to get both impurities and defects well under control, as there is a high probability of defects propagating from the seeds used to grow single crystal diamond plates. Research literatures show that some control in defect propagation can be achieved by off axis growth of the plates from the crystallographic axis (001). This proposed work will further investigate off-axis

growth of thick diamond plates and then characterize them to establish better growth techniques of lab grown diamonds applicable for detector fabrication.

1.3. Dissertation outline

The plan mentioned in previous section of this thesis work has been conducted, divided and explained in the next six chapters.

The chapter 2 begins with listing important properties of diamond which makes it an interesting material, especially for radiation detectors. The chapter next covers the working principles of radiation detectors and their types. Then the discussion moves to the kind of interactions that takes place when energetic particles impinge and penetrate a host material. Here a simplified scenario is described for the sake of the general aim of this thesis. However, this area of interaction of heavy ion beams with materials (especially with diamond) is still an evolving field. This chapter finally covers the state of worldwide research that has been going towards exploration of single crystal and polycrystalline diamond as a material for radiation detector.

The basic structure of radiation detector made from single crystal diamond plates is discussed in the first section of chapter 3. The detector fabrication relies on a parallel plate capacitance structure where a dielectric material (diamond plate) is grown with electrodes in two flat surfaces. The next section discusses how these detectors are irradiated with a swift heavy ion beam of energy 120-150 MeV/nucleon at the National Superconducting Cyclotron Laboratory (NSCL) at MSU. Further this section describes how the response of the detector is measured (output voltage) and eventually translated into analyzing/quantification of degradation and the basic parametric nature that the degradation curve follows.

Chapter 4 investigates the effect of beam irradiation on the electrical, optical and structural properties of diamond. The first broad section covers electrical characterization. The basis of this work is built upon the transient current technique, where a small-scale irradiation on one side of the sample generates charges, which are swept across the sample with an externally applied electric field. The first section discusses how transient current signals are measured with an external circuit and eventually how charge collection and lifetime of charges are calculated from the signal curves. The second section of electrical characterization investigates if any significant change takes place in the leakage current of the detectors, which is expected to stay in the picoampere ranges within a range of applied electric field for a good quality of diamond. In the next broad section, the optical properties of beam irradiated diamonds were studied. The optical transmission of diamond and its absorbance were measured in the UV-Vis and infrared region. This study helped to compare between pre-irradiated and post irradiated optical properties of diamond plates. The last section in this chapter looks for evidence of any structural damages that might have happened due to the beam irradiation. A rocking curve study of the (004) plane in the diamond was measured by a high-resolution x-ray diffraction system and Raman spectroscopy of the irradiated diamond plates was also investigated.

An important area directly related to this work is the growth of single crystal diamond. Chapter 5 comprises a general discussion of single crystal diamond deposition by the chemical vapor deposition technique. The chapter begins with chronological events through which diamond deposition by chemical vapor deposition technique has reached its current state. The next section describes a general overview of processes associated with chemical vapor deposition of diamond. Finally, the chapter discusses the microwave plasma assisted chemical vapor deposition (MPACVD) technique. In particular, different types of MPACVD reactors available worldwide

are described with an expanded emphasis on reactors designed at Michigan State University (MSU) and their operation.

The importance of diamond deposition on misoriented substrates (i.e. substrates with the top growth surface prepared at a miscut angle from the (001) crystallographic plane) is discussed at chapter 6. The chapter begins with a detailed literature review on the aspects of diamond deposition on misoriented substrates. The next section discusses the relevance of this growth strategy with this current work. The specific reason is to reduce the nitrogen content in the diamond which will give a better performance of diamond detectors. This section is followed by a detailed explanation of specific steps associated with growth on misoriented substrates, especially the preparation of offcut angled substrates. The next section in this chapter covers the characterization of the growth samples examined using an optical microscope, i.e. discussion on the different features present on the surface of the grown layer. The final broad section describes in detail how step and terraces appear on misoriented substrates. Their dependence on growth time and the offcut angle is carefully explored. This section ends with building up an overall distribution of step heights and terrace widths for grown layers on different misoriented substrates.

Finally, chapter 7 concludes and summarizes the overall work performed in this thesis. It also provides future direction towards growth of thick single crystal plates in a low nitrogen impurity environment by using misoriented substrates for future applications of lab grown diamonds for radiation detectors and other electronic devices.

Chapter 2. Introduction to radiation detectors

2.1. Properties of diamond material

Diamond is comprised of carbon atoms forming a tetrahedral structure, connected by strong sp^3 hybrid bonds (Figure 2.1) [7]. The strong sp^3 bond results in diamond's many exceptional properties. Single crystal diamond has a very high atomic density, highest bulk modulus and highest thermal conductivity. It is also highly transparent in far infra-red to visible and partially in UV range. Diamond has been traditionally used as an abrasive material and it still enjoys the status of being one of the hardest materials. Diamond is a wide bandgap semiconductor in the semiconductor materials group with high carrier mobility. Table 1.1 [8] shows some of the very outstanding properties of diamond as a semiconducting material.

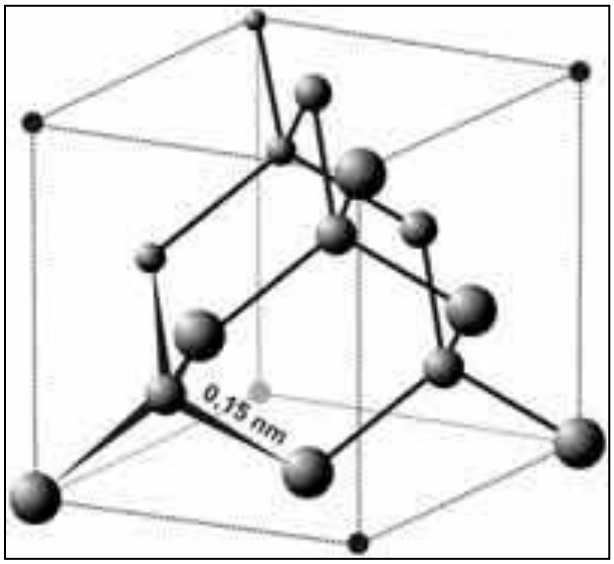

Figure 2.1. Bond of carbon atoms in diamond structure

Table 1.1. Some important material properties of diamond [8]

Mechanical hardness ~ 100 GPa
Highest bulk modulus (1.2×10^{12} N m^{-2})
Highest thermal conductivity @ room temperature (2×10^{3} W m^{-1} K^{-1})
Thermal expansion coefficient @ room temperature (0.8×10^{-6} K^{-1})
Wide bandgap (~5.47 eV)
High breakdown field (~ 10^{7} V cm^{-1})
Displacement energy 40-50 eV/atom
Carrier mobility (2400 cm^2 V^{-1} s^{-1} for electrons and 2100 cm^2 V^{-1} s^{-1} for holes
Energy required to create e-h pair 13 eV

An application of single crystal diamond is radiation beam detection in harsh radiation environments. The idea behind this application is to develop detectors for high radiation environments where silicon-based detector technology fails quickly. Single crystal diamond is considered to be a radiation hard material due to its high atomic displacement energy of 40-50 eV (compared to 13-20 eV for Si) and its high breakdown electric field. In addition, the higher carrier mobility helps in the better realization of fast detectors. Diamond is considered as a wide bandgap semiconductor which behaves almost like an insulator in undoped condition. Therefore, while used as a detector it doesn`t require the formation of p-n junctions by doping. Instead single crystal undoped diamond material can perform quite well as solid state detector.

2.2. Radiation detection basics

The term "radiation" expresses the phenomenon of transportation of energy and mass through space. This energy originates from a source and travels through space till it gets partially or fully absorbed by any material. Radiation can be broadly classified into two forms including electromagnetic radiation and particle radiation. Radiation can be of either ionizing or non-ionizing. Ionizing radiation can create unbound charges in a material by liberating electrons from the atom. The amount of charge generated depends on many factors like the type of radiation, the energy of the radiation with which it strikes the material, the target material itself and the depth it can penetrate. Some ionizing radiation type are α-radiation, β-radiation, γ-rays and X-rays. There are numerous natural sources which emit γ-rays and there are also sources which also emit α and β- particles with γ-rays. Also bombarding any stable nuclei with high energy particles produced in accelerators can yield these kinds of radiations. A schematic in figure 2.2. shows the penetration depths of different ionizing radiations[9].

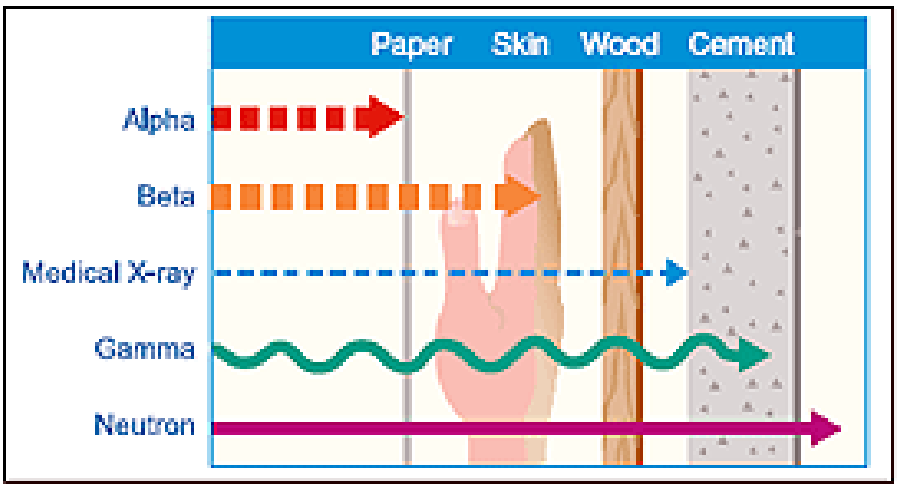

Figure 2.2. Penetration depths of different ionizing sources [9]

The basis of detection of radiation relies on the interaction of the radiation beam with a suitable material build into a detector device. Thus, material selection plays an important role in the fabrication of radiation detectors. The interaction of the beam with the detector material is converted to electrical signals sensed through external circuit elements. Currently, most of the radiation detectors depend on ionization as the principle of operation. Charges are generated through ionization and any movement of the charges produced by an applied electric field before they recombine is sensed through the external circuit (as shown in a schematic in figure 2.3). The number of quanta of radiation that interacts with the material within a particular time span generally determines the external signal that is generated.

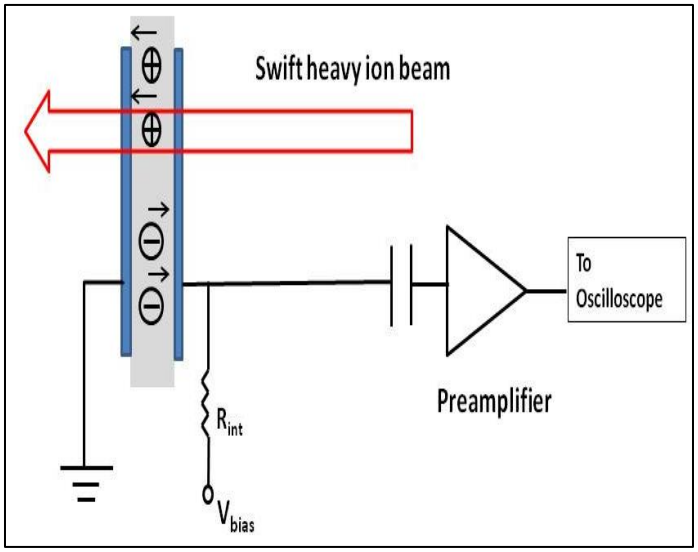

Figure 2.3. A schematic of detector`s circuitry

The modes of detection can be broadly classified into two main mechanisms, **(i) current mode detection and (ii) pulse mode detection** [10]. In the **(i) current measurement mode** of detection a current meter or more precisely a nano/pico ammeter is attached to the output terminals of the radiation detector. A schematic of the mechanism is shown below in figure 2.4,

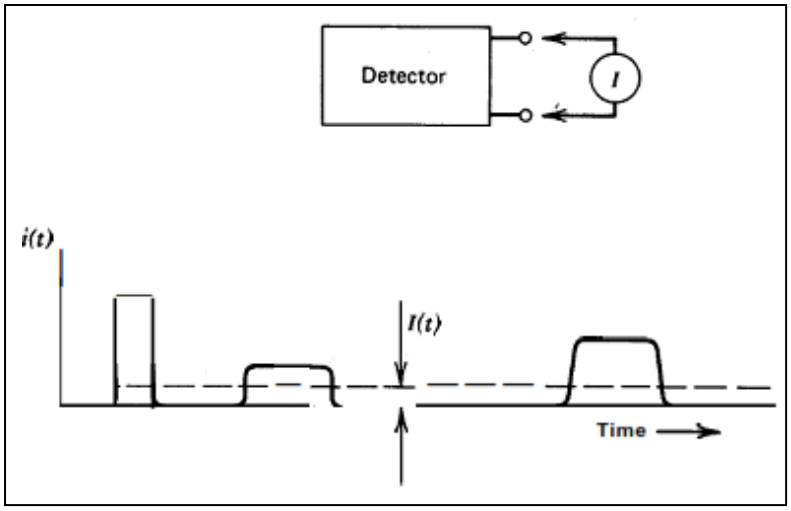

Figure 2.4. Current measurement mode of a detector [10]

The final output from this measuring device can be expressed as,

$$I(t) = \frac{1}{T}\int_{t-T}^{t} i(t')\,dt'$$

where the device has a response time T, where i(t') is the current generated by a single particle interacting with the detector. The actual output I(t) is calculated by averaging many of the events that happen within the time frame, T.

A steady-state irradiation of a detector can be expressed as combination of a constant current I_o and a time dependent fluctuating component $\sigma_i(t)$, arising from the random nature of radiation as shown in the figure 2.5.

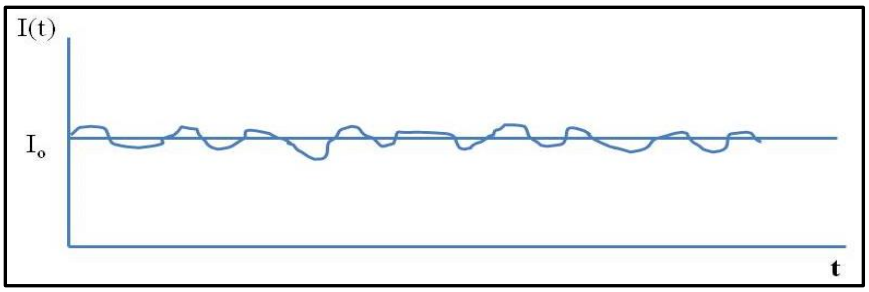

Figure 2.5. Current in a detector due to steady state irradiation [10]

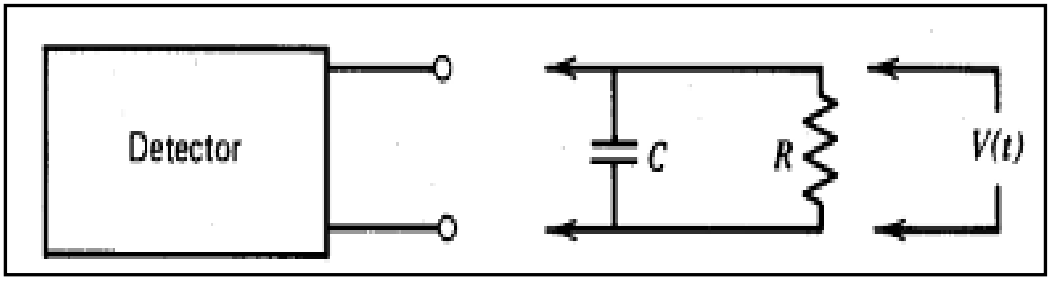

Figure 2.6. Operation of a detector in pulse mode [10]

The **(ii) pulse mode detection** provides information about the amplitude and timing of an individual radiation event. The nature of the response is guided by the circuit (preamplifier) the detector is connected to. The equivalent circuit diagram is shown in figure 2.6. The effective input resistance is R and the equivalent detector and circuit capacitance is represented by C. It is the time-dependent voltage v(t) on which the pulse mode operation is centered. The time constant τ of the measuring circuit is given as $\tau = RC$. There can be two different regimes the pulse mode operation can work.

For time constant τ being small so that ($\boldsymbol{\tau << t_c}$, where t_c is the charge collection time), the current flowing through the external load follows the exact shape of the instantaneous current in the detector. Hence the voltage v(t) across the resistor also takes nearly the same shape of the time

dependent current, as shown in figure 2.7 (b). When timing information or high event rate becomes an important issue then radiation detectors are operated in such conditions.

In the other extreme case, the time constant τ is adjusted to a larger value compared to the detector`s charge collection time, i.e **($\tau >> t_c$).** In this case the signal pulse current i(t) charges the capacitor and increases load voltage v(t). Then the capacitor will slowly discharge through the resistor and v(t) will gradually reach back to zero. The voltage variation is shown in figure 2.7 (c).

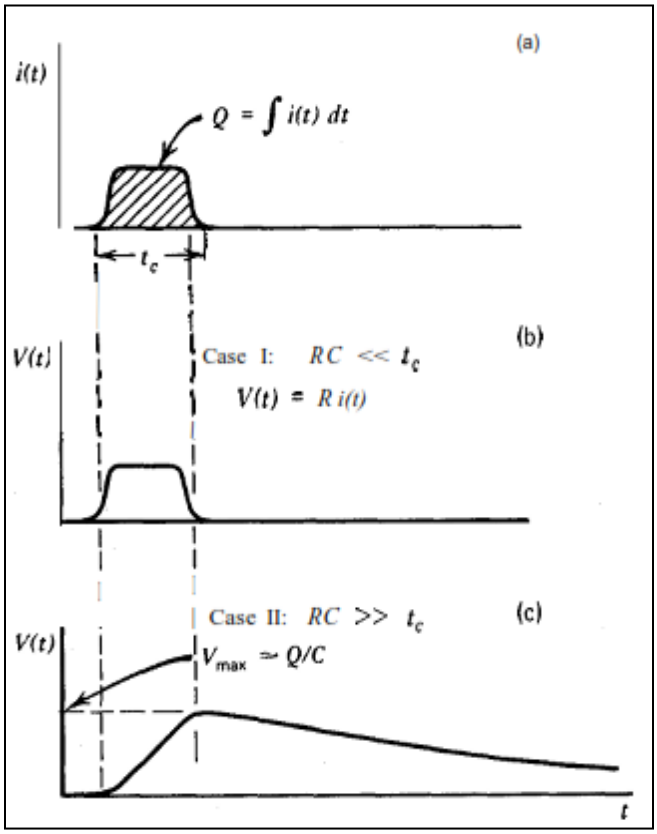

Figure 2.7. The output signal for a detector circuit with small time constant (b) and for a circuit with large time constant (c) given a particle interaction (a) [10]

It is observed that the rise time for the signal to reach the maximum value is dependent on the detector's response (i.e. its charge collection time), and not influenced by the load circuit. In

contrast, the decay time is only determined by the time constant of the external circuit. Also, the ratio of the total charge generated in the detector Q and the capacitance of the load circuit C decides the maximum value of the external voltage, i.e. V_{max}. Therefore, if the capacitance C remains constant for each pulse, the voltage maintains a linear dependence on the generated charge. In such cases, a charge sensitive preamplifier circuit is used which can eliminate the variation of capacitance on output voltage. Pulse mode operation is the most widely used detector configuration for radiation as it holds more information through the detection of individual pulses.

2.3. Types of radiation detectors

Radiation detectors are classified based upon the type of medium used for the radiation beam to interact with and the way the interaction is captured to convert it into a measurable physical quantity [11]. On some occasion, some devices may only count the rate of impinged particles and hence known as counters, however the major goal of detectors is to quantify the energy or study the beam profile both in terms of spatial and temporal distribution. In a **gas-filled detector** the ionization happens in a gaseous medium, i.e. when a radiation beam passes through, a small volume of gas gets ionized and produce free electrons and ions [12]. An applied electric field drives the electrons and ions to respective electrodes to generate a current signal in the output. The generated current amplitude depends on amount of generated charges, strength of the field, geometry of electrodes and recombination of charges. There are few different types of gas filled detectors, namely; **ionization chambers, proportional counters** and **Geiger counters** as their mode of operation is decided based upon the range of applied voltage, as seen in figure 2.8. In an **ionization chamber** a weak electric field is applied between parallel plates to collect most of the ions produced by the incident radiation. Ionization chambers are used to detect mostly x-rays and

γ-rays. Ionization chambers work in either current detection mode or pulse counting mode. In proportional and Geiger counters a wire along the axis of the hollow cylinder acts as the positive electrode and the hollow cylinder surrounding the wire is used for the negative electrode. When the gas is ionized the electrons and the ions are swept away from the sensing volume to respective electrodes. In proportional counter the amount of collected charges is larger than that by ionization chamber. Proportional counters use stronger electric drift fields and primary charges are accelerated to high enough energies to cause secondary ionization. This gas amplification process generates a larger amount of total charge which is still proportional to the amount of primarily generated ions.

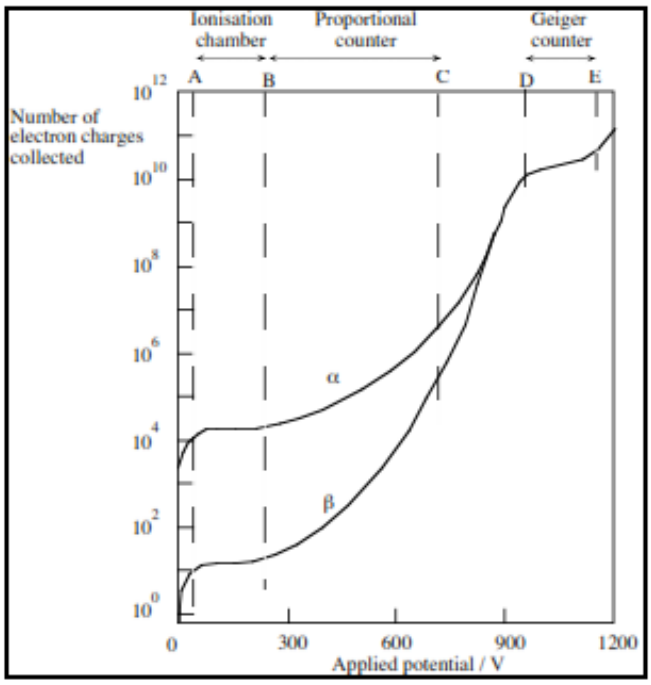

Figure 2.8. Charge collected by different gas filled detectors [5]

In Geiger counters the gas amplification process takes place over a larger volume through photons generated through secondary collisions over the entire volume. The gas amplification is eventually limited when the field due to the secondary electrons are strong enough to interact with the applied field and the effective field is barely strong enough to support any gas amplification. In this scenario the output current no longer is proportional to the number of primarily generated ions and it gets saturated to a value depending on the detector geometry and the applied field. Generally, Geiger counter works in a pulse mode and the pulse rate is counted through an external circuit. Figure 2.8 depicts the respective ranges of operation of different gas filled detectors.

A Scintillation detector is another type of radiation detector which converts interaction of ionizing radiation into luminescence. Through ionization, an electron can get excited from valence band to conduction band or to any mid-gap states created due to impurity. An exciton is formed when the hole and the electron form an electrostatically bonded pair. The excited electron decays to the ground state and releases the energy in the visible to UV range. This released energy spectra is directed to a photocathode in a photomultiplier where electrons are emitted due to photoelectric effect. The electrons generate a current in the external circuit by a multiplication process. Scintillation detectors are characterized by a fast response and significant intensity of the generated signal. Scintillation detectors are comprised of either organic or inorganic material as detection material. Generally inorganic scintillators are slightly slower in response as compared to organic ones, however inorganic scintillators are more efficient due to having denser structure and higher atomic number. Scintillation detectors are quite widely used for medical purposes, high-energy physics experiments and security purposes.

Semiconductor detectors [13] are another widely used detector type that work almost like ionization chambers. These are solid state detectors where the radiation creates electron and hole

pairs that are swept away under the influence of an external electric field to generate a pulsed signal through external electronics. The major advantage of semiconductor detectors is that these devices offer excellent energy resolution as it requires less energy to create an e-h pair for semiconductors (~3.6 eV for Si, 2.6 eV for Ge and 13.4 eV for diamond) which is generally less as compared to energy required to create an electron-ion separation. Si and Ge are the most used materials for semiconductor detectors.

In general, for a semiconductor radiation detector a p-n junction is used to generate a charge depleted region. For this detection purpose, the p-n junction is operated in a reverse bias mode, which results to an increase of depletion region width as well as a drop for junction capacitance. When a radiation beam impinges in the junction region it creates electron hole pairs which can get swept across the junction by an external applied field and reach respective electrode to generate a current in the external circuit. A schematic of the basic operation is shown in figure 2.9.

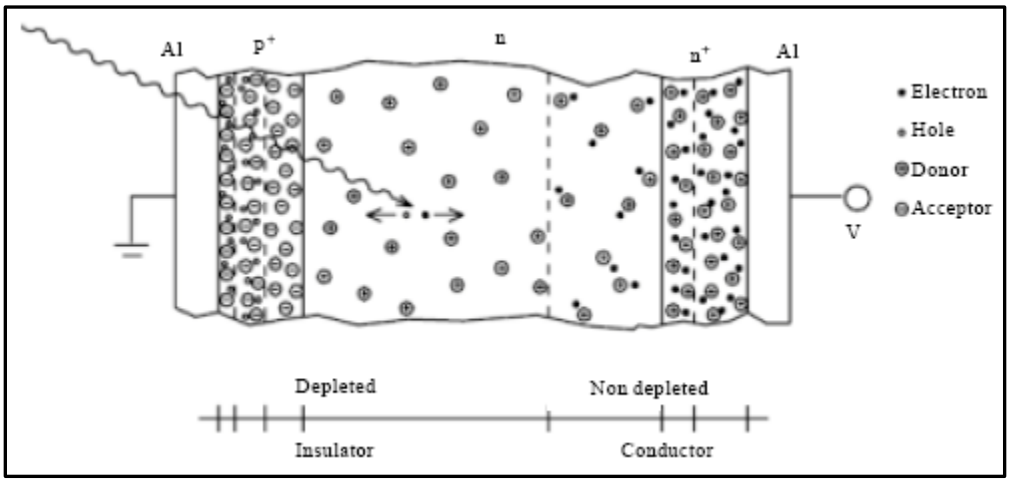

Figure 2.9. A p-n junction acting as a radiation detector [12]

The probability of thermal generation electron -hole pair P(T) is expressed as

$$P(T) = CT^{3/2}\, e^{-E_g/2kT}$$

where T is absolute temperature, E_g is the band gap of an intrinsic semiconductor, k is the Boltzmann constant and C is a proportionality constant characteristic of the material, kT= 0.025 eV at room temperature. Comparing between two popular semiconductors, Si (E_g = 1.1 eV) and Ge (E_g = 0.67 eV), it is quite essential that Ge based semiconductor detectors require cooling to minimize the dark current`s effect due to its small band gap which is not necessarily required for Si. Wide bandgap semiconductors like diamond with E_g = 5.45 eV not only need no cooling, it has a very low intrinsically carrier concentration which offers low dark current without forming a pn junction. For Si based detector, a junction formation is necessary to create a large resistive path. So single crystal diamonds for radiation beam detectors acts like a solid-state ionization chamber. For diamond semiconductors, a simple parallel plate capacitance structures can be used for radiation beam detectors.

2.4. Interaction of radiation beams with material

The detection mechanism in any type of detector relies on the interaction (and interaction volume) of the radiation beam with the material used in the detector [14]. When a beam of radiation penetrates into a material either part of it or the full beam might pass through the material, with some possible scattering. Therefore, in all practical events the interaction of the beam with the material results into partial translation of energy into the electrons or the nuclei of the atoms. Generally, charge particles interact with host/absorber material through electromagnetic interaction, whereas for neutral particles the nuclear interaction predominates which further generates charge particles.

The electromagnetic interaction between a charged particle beams and host atoms comprises of two steps (i) excitation and ionization of atoms and (ii) bremsstrahlung [15],[16].

The bremsstrahlung process is mostly associated with radiation losses for electrons, as the interaction is inversely proportional to squared mass of incident particle. Each charged particle goes through several events of scattering and deflection at each interaction before it comes to rest. The electromagnetic interaction causes transfer of energy even without any direct collision, i.e. even the charged particles can interact with the atoms while passing through its vicinity. The result of the transfer of energy would lead to either raising the atom to higher energy level, i.e. excitation or removal of an electron from its parent atom by ionization. For interaction of heavy ions, beside excitation and ionization, other phenomena like redistribution of charges, creation of secondary electrons and occasionally some structural modifications of the host material can occur. The secondary electrons are only generated if the primary electrons (generated from ionization) have enough energy to further knock out electrons from atom. The secondary electrons are also referred as δ-ray.

An important parameter, which helps to characterize the interaction of charge particle beam, is energy loss per unit length or **stopping power** [17] of the material. The stopping power depends on both the incident particle and the target material. The major contribution to stopping power arises due to electronic and nuclear interactions. Hence the total stopping power (S) is the sum of the electron stopping power and nuclear stopping power.

$$S = -\frac{dE}{dX} = S_{electronic} + S_{nuclear} \qquad \text{(a)}$$

The negative sign indicates the drop of energy of the particle with increase in penetration length in the material. A detailed expression of the energy (E) loss over a distance (x) for the charged particle passing through a material is expressed by Bethe-Bloch distribution[18],[19] given as;

$$-\frac{dE}{dx} = 2\pi N_a r_e^2 m_e c^2 \rho \frac{Z}{A} \frac{z^2}{\beta^2} \left[\ln\left(\frac{2m_e \gamma^2 W_{max}}{I^2} \right) - 2\beta^2 \right] \quad \text{(b)}$$

where the terms are defined as

r_e : classical electron radius = 2.817 $\times 10^{-13}$ cm.

m_e : electron mass, N_a: Avogadro`s number = 6.022 $\times$ 10^{-23} mol^{-1}

I: mean excitation potential., Z: atomic number of absorbing materials

A: atomic weight of absorbing material. ρ: density of absorbing material

e: electron charge, z : charge of incident particle., γ : $\left(1 \Big/ \sqrt{1-\beta^2} \right)$

β = v/c = speed of particle with respect to c and

W_{max} : maximum energy transfer in a single collision.

For simplicity of discussion the Bethe-Block distribution can be qualitatively expressed as;

$$\frac{dE}{dx} \alpha \rho z^2 / v^2 \quad \text{(c)}$$

Hence the particle velocity is a prime parameter for the energy loss distribution, i.e. for non-relativistic regime, dE/dx varies inversely with kinetic energy. This can be interpreted as, that at low particle velocity the charge particles have a higher chance to stay near the electrons and therefore higher is the transfer of energy. On the other hand, for different particles moving at the same velocity the charge state z will be the factor for energy loss. The energy loss diagram for different charged particle versus kinetic energy with Bethe-Bloch distribution is shown in figure 2.10. As seen here, α-particles loose energy at much higher rate than protons at the same kinetic energy level due to its charge state. The distribution also shows that for some of the particles above

several hundreds of MeV energy range the stopping power reaches a near minimum value. At this condition these particles act as "minimum ionizing particles" (MIP). The electrons also act the same way at an energy level close to or lower than 1 MeV.

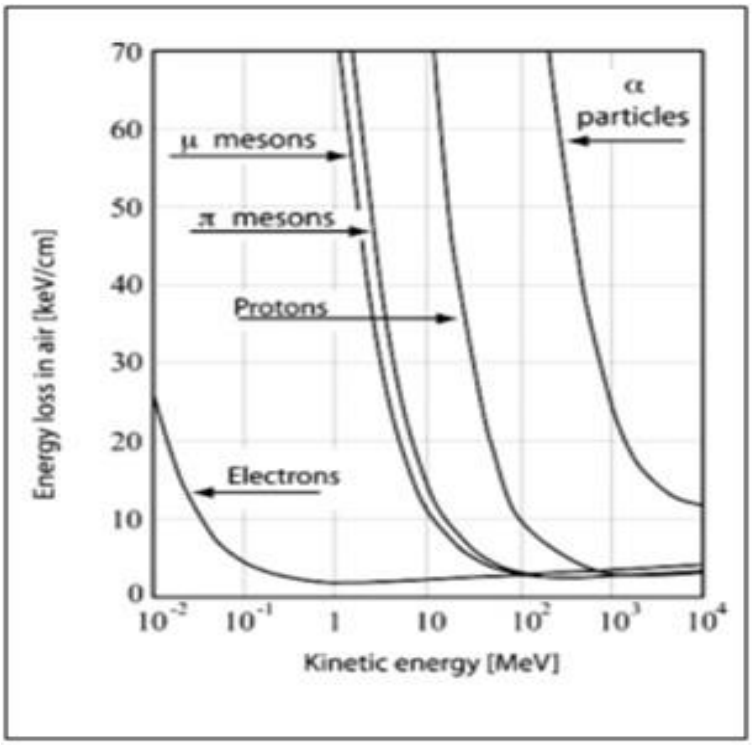

Figure 2.10. Energy loss diagram of different particles [5]

Figure 2.11 shows that for a given particle with specific charge, the rate of energy loss has a similar value for different materials except hydrogen. However, there is a marginal drop happening in the rate of energy loss with increase in the host materials atomic number Z. Other than hydrogen, the minimum ionizing energy has minimal variation, ranging between 1-2 MeV/g.cm^2 with change in Z from 7 to 100. Beyond minimum ionizing point, with increase in energy the energy loss rises slowly [20].

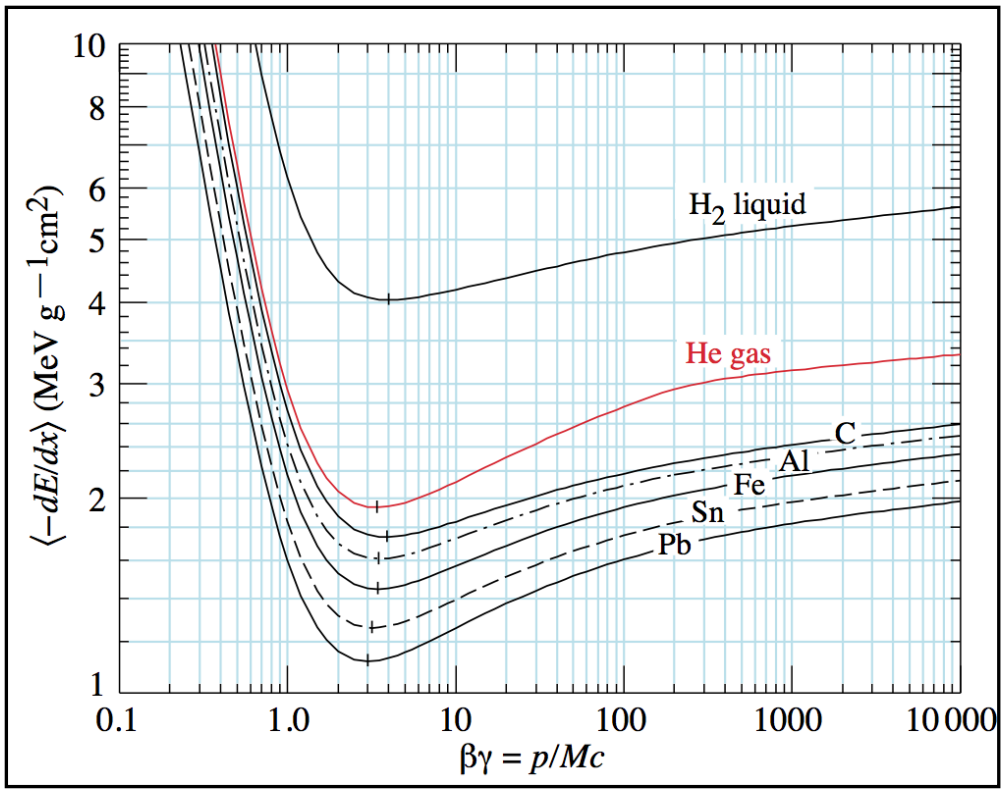

Figure 2.11. Mean energy loss rates for particles in different medium [19]

As a heavy charged particle moving with low energy (~MeV) goes deeper inside a material it further loses energy and stopping power changes accordingly. As stopping power is a measurement of ionization capability of the particles inside the material, any change in stopping power is equivalent to alteration of ionization capability. The following simplified expression of Bethe-Block distribution shows the stopping power distribution of α-particles inside a material.

$$-\frac{dE}{dx} = \frac{K}{\beta^2}\left[\ln\left(\frac{W_{max}}{10^{-4}}\right) - \beta^2\right] MeVcm^{-1} \qquad \text{(e)}$$

where $K = 0.30548\frac{\rho Z q^2}{A}$ is a constant for a given material and I is considered as 10^{-4} MeV, a typical number for low Z materials. The corresponding plot is shown in figure 2.12.

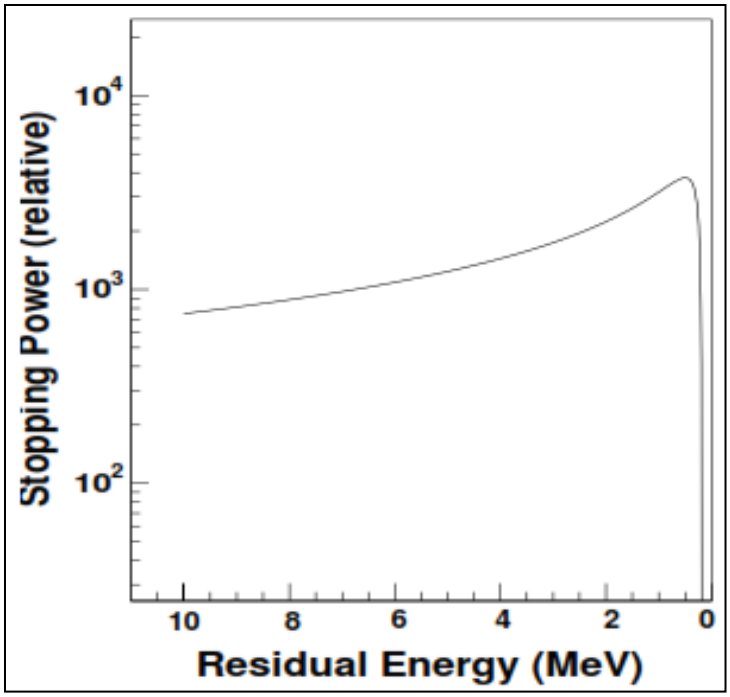

Figure 2.12. Stopping power vs Energy [16]

As seen, with the gradual increase in stopping power, the ionization increases until it reaches to a maximum point known as **Bragg peak** [21]. Beyond this point the particle sharply loses all the energy and becomes neutralized. This overall phenomena (plot) is known as Bragg curve.

For heavy charged particles, there appears a point where the particles do not have sufficient energy for ionization and the loss of energy mainly happens due to nuclear collisions. In an overall situation the electronic stopping dominates the particles interaction with material as long as the particle velocity is in the relativistic range. In case of electronic stopping the particle beam nearly follows a straight trajectory with minimum deflection. Based upon its initial energy the particles gradually loose energy and go through an intermediate stopping. In this range the charged particles pick up electrons. The capture of higher orbital electrons continues until the ions become neutral.

The beam trajectory goes through some directional change and slows down further. In the final range of stopping, the particles reach low ionization state or almost a neutral state.

One of the important phenomena associated with the interaction of particles is that the energy loss process is statistical in nature. An expansion of the energy curve always happens after charged particles pass through a particular thickness of the absorber. The width of the energy distribution curve is a measurement of **energy straggling** which varies along the distance travelled by the particle. Figure 2.13 shows, how with the penetrating distance the energy profile of a monoenergetic particles gets skewed as an effect of energy straggling.

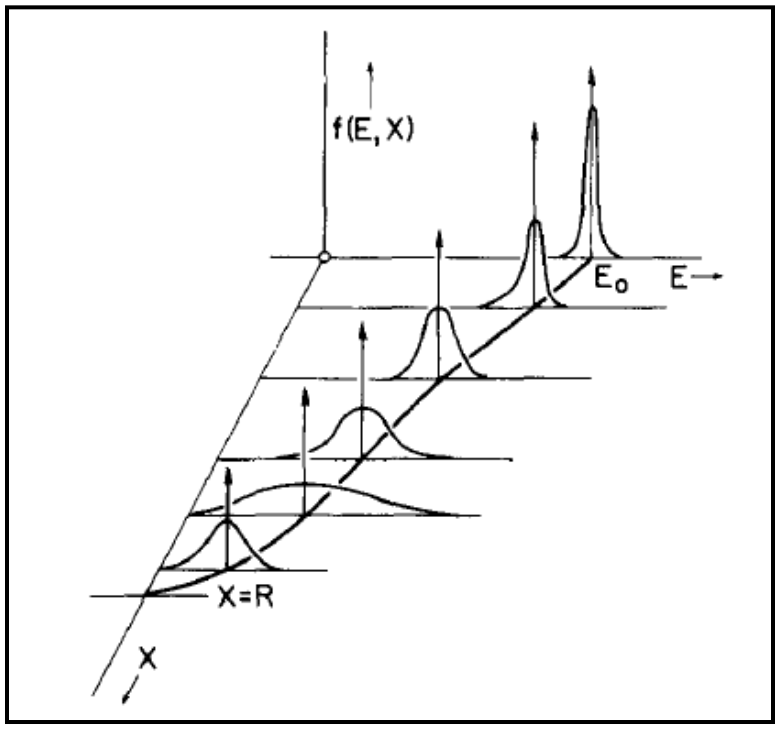

Figure 2.13. Energy distribution of a monoenergetic beam varying over penetration depth [19]

As an effect of energy straggling the Bragg curve (in figure 2.13) will slightly get deformed in the end with a small tail.

Another important parameter related to particle interaction is the range or the average distance a particle beam can travel in an absorber. This could be computed by integrating the average power over the entire energy spectrum of the incident particle,

$$R(T) = \int_o^T \left[-\frac{dE}{dx}\right]^{-1} dE \qquad \text{(f)}$$

The range R(T) shows some statistical fluctuation around a mean value as it goes through multiple coulomb scattering. The fluctuation associated with the range is known as **range straggling.**

The end result of different types of interaction of radiation with matter can be radiation damage. Some radiation damage can be partially healed but for some damages the material is permanently degraded. So, the different scenarios can be described by different types of defects [22]. (i) **Impurities** are caused by radiation when a nuclei transmutes to another radioactive nuclei. Neutron and ion irradiation can generate new radioactive species. Neutron capture by a nucleus can produce an isotope different than the original detector material and the new isotope may decay. This can often distort the chemical composition of the detector material. Ion irradiation causes an impurity to be added to the detector material and it can also cause new radioactive species to be created by interacting with the detector material atomic nucleus. These impurities can slowly and gradually affect the electrical and material properties of the materials. (ii) **Displacement damage** takes place due to transfer of kinetic energy from radiation to atomic displacement in the detector material. An elastic collision can displace an atom from its lattice position which is a primary knock on and triggers multiple secondary atomic displacements. The displaced atoms are referred as interstitials and the void position is known as vacancies. Together, a Frenkel pair is formed. Displacement damage is a clear evidence of nuclear interaction. Vacancies and interstitials can

become mobile at sufficiently high temperature and therefore occasionally a high temperature annealing process can initiate recombination of both and hence help to reduce the number of defects (radiation damage) accordingly.

2.5. Current state of art of diamond-based radiation detectors

Diamonds inherent properties like chemical inertness, stability and operational capability at high temperatures and extreme radiation resilience make it a very useful material at extreme environments. Historically, the high cost of mining and processing of natural diamonds restricted diamond's industrial applications until about 1960 when the first successful production of synthetic diamond was reported. The very first kind of synthetic diamonds were grown by a technique of processing graphite at high pressure and high temperature and eventually converting it to diamond, better known as HPHT diamonds. The next couple of decades had seen some other different approaches to grow synthetic diamond which finally resulted to the invention of chemical vapor deposition (CVD) technique which has gone through further improvement and refinement. Currently microwave plasma assisted chemical vapor deposition (MPACVD) [23] stands as a very efficient process to grow high quality diamond.

Industrial applications of diamond range beyond its traditional use as an abrasive to include the fields of optics, RF and microwave transmission technology, heat sinks, and electronics.[24] An important material property of diamond is the high displacement energy (~ 45 eV/atom), much higher than of other contemporary semiconductors. (e.g. 20 eV for Ge, 25 eV for Si and 9.9 eV for GaAs) [22,25]. This property makes diamond an attractive material for radiation detectors in the fields of nuclear and high energy physics. Initially, diamond-based detectors had to face steep competition with silicon-based particle detectors due to the optimized product quality of Si, but

with steady improvement in the quality of synthetic diamond the current scenario appears to be very promising for diamond.

Recently, clinical radiotherapy applied diamond for base dosimeters [26] because diamond offers fast response with a very low volume of deposited dose and because due to diamond's close to human tissue equivalence (atomic number Z=6 is close to Z_{eff} of biological tissues) it requires less correction to the signal read. Ciancaglioni et al. discussed the performance of a metal-semiconductor-metal structure made of polycrystalline diamond (PCD) [27], which was applied for x-ray dosimeter. The comparison between diamond and silicon PCD based dosimeters show diamond to be more suitable compared to silicon-based devices. Single crystal diamonds are also used for high energy X-ray detection [28] in synchrotron radiation sources. These detectors show good linearity with respect to X-ray photon flux. Single crystal diamond has also been tried for successful application as a photodiode for X-ray radiometry [29]. The response of the photodiode improves by applying a pulsed bias to minimize the effect of trapping and de-trapping of charges. In another field of application, photo current and spectral response of diamond-based photoconductors, built of high quality single crystal diamond, have been studied in the deep UV range [30]. A multilayer diamond detection system was used for monitoring space radiation to study spacecraft's performance. These are known as radiation situation detectors, which measures cosmic flux to decide safe operating conditions of spacecrafts.

In the field of high energy physics, diamond-based radiation detectors are making a breakthrough by upgrading silicon-based detection technology because diamond offers higher radiation hardness. This however took some close collaboration between particle physicist and manufacturers of synthetic diamond to bring the state of art to a very advanced and promising level. It is expected that in the high-energy regime of hundreds of MeV/nucleon to few

GeV/nucleon range diamond will be more radiation tolerant and will survive longer than existing silicon-based detectors. In a comparative study between diamond and silicon irradiated with protons and neutrons the diamond material ranged from slightly more radiation hard at lower energies to significantly more radiation hard at higher energies above 0.1 GeV [31].

The RD42 collaboration program of CERN has conducted a comprehensive study on the performance of diamond detectors in radiation harsh environments. The major motivation was to establish detectors which can survive for many years for ATLAS and CMS experiments at the LHC (Large Hadron Collider) [32]. The current planned upgrades in LHC to High Luminosity (HL-LHC) will increase the fluence to the inner most tracking detector to 2 x 10^{16}/cm^2. A report from this group a few years back, discussed the response of scCVD (single crystal CVD) and pCVD (polycrystalline CVD) based diamond detectors up to 1.8×10^{16} protons/cm^2, which showed great potential for diamond base detectors to survive this type of radiation harshness. Two decades ago, poly-crystalline diamonds (PCD) were used with pion and proton beams in order to study radiation tolerance of diamond while in use as tracking detectors by the RD42 group. Polycrystalline diamond substrates suffer from non-uniform charge collection due to the presence of grain boundaries. As a result, the quest for an improvement in charge collection distance continued and a study on polycrystalline diamond detector performance was reported from the RD42 collaboration group [33]. Proton irradiation on strip trackers made of polycrystalline diamond were shown to retain 25% of their initial signal strength after exposed to a flux of 20×10^{15} p/cm^2 [34,35]. However, with the advent in microwave plasma-assisted chemical vapor deposition (MPACVD), single crystal diamonds became more readily available.

Single crystal diamonds (scd) offer higher charge collection distances, and nearly 100% charge collection efficiency for samples with very low impurities, and superior spectroscopic

properties and time resolution [36]. In one of the pioneering studies, the RD42 group compared the radiation hardness of both PCD and SCD with proton irradiation. The SCD diamond strip detector responded with a higher pulse height as compared to PCD diamond. However, the most interesting observation was the degradation of the charge collection distance (CCD) with particle fluence. With a required shift in the SCD data point it was found that both types of diamond followed the same nature of damage (i.e. assigned same damage constant on the fitting curve). The study of radiation hardness in both types of diamond continued with different proton energy beams [37]. As an interesting outcome, the damage constant was found to marginally drop with proton energy increased from 25 MeV proton to 24 GeV proton beams.

In this project we are studying the radiation tolerance of single crystal diamond in swift heavy ion (SHI) beams. SHI beams are ion beams from elements with heavy nuclei accelerated to relativistic energies. Future rare isotope facilities will provide particle beams of heavy ions with unprecedented intensities with particle rates of up to 10^8 particles per second. Diamond is one of the few materials for tracking and timing detectors that is expected to withstand such beams with reasonably useful lifetimes. A few reports have shown promising outcomes of the interaction of diamond with SHI beams [38,39]. The radiation damage for relativistic Au beams was studied by Pietraszko et al.[35] for fluences of ~10^{14} cm^{-2}. Gracia et al. looked into possible amorphization of diamond samples irradiated up to 40 MeV beam energy [40]. Even at a very high electronic stopping power range, the authors have found that nuclear stopping power created the major effect in the diamond. In their study the authors showed that the surface damage increases proportionally with nuclear stopping power. In another report, a single crystal diamond-based detector (for time of flight study) had been irradiated by ^{197}Au beam. After collecting nearly 10^{14} /cm^2 Au ions the

pulse height measurement by ion beam induced current (IBIC)[41] showed a drop of almost 5.1 times in the area of radiation damage.

In this work SHI beams of Sn and Zr were used to irradiate diamond detectors and study the degradation at a similar fluence range. Both laboratory grown and commercially available single crystal diamond grown by the MPACVD process were used to construct detectors for SHI beams measurements and their performance are compared. Samples were irradiated at the National Superconducting Cyclotron Laboratory (NSCL) at MSU.

Chapter 3. Performance test of radiation detectors

For our experiments, lab grown single crystal diamond substrates produced in MSU MPACVD reactors were cut and polished to fabricate detectors. In addition, electronic grade commercial diamond substrates were also used to build detectors and subsequently irradiate in the same kind of beam. The transient current technique (TCT)[42–44] was measured to quantify the charge transport mechanism, charge collection efficiency and carrier lifetime in the irradiated part of the SCD crystal and compared to a lightly irradiated and non-irradiated SCD diamond substrate. In addition, UV-VIS spectroscopy, FTIR, X-ray diffraction, Raman spectroscopy was also used to understand the post irradiation effect on the diamond substrates.

3.1. Fabrication of radiation detectors

In this study two different types of diamond plates were utilized to fabricate detectors. The first batch of diamond samples were grown and processed at Michigan State University (MSU) by the MPACVD technique. Single crystal diamonds were grown on commercially available high pressure high temperature (HPHT) seeds, at 180 Torr pressure for 48 hours with feed gases of 400 sccm H_2 and 20 sccm CH_4 in a deposition reactor operating at 2.45 GHz microwave power of 2.5 kWatts [45]. After growth, the samples were laser cut from the seed, mechanically polished and cleaned in boiling acid (at 350^{o}C in H_2SO_4/HNO_3 (1:1) for 30 minutes followed by HCl for 20 minutes) to prepare 3.5 mm × 3.5 mm samples with thickness of 0.6 ~ 0.7 mm.

The other batch of samples, 3.0 mm x 3.0 mm with 0.5 mm thickness substrates of electronic grade, were purchased from a commercial vendor and cleaned using the same procedure.

Any further residues were removed by cleaning the samples using acetone and methanol in an ultrasonic bath. The surfaces (both top and back) of the detectors were next exposed to oxygen plasma for 2 minutes to terminate with oxygen in order to reduce any surface conduction.

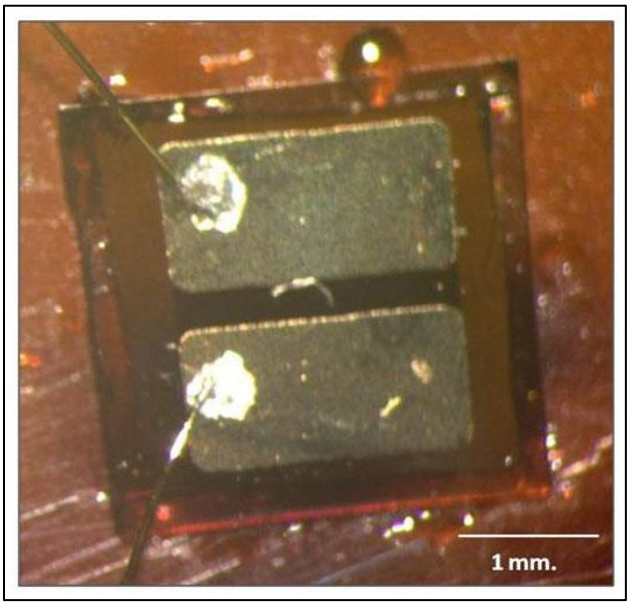

Figure 3.1. Top surface of the single crystal CVD diamond plate with electrodes

After cleaning and oxygen termination, 150 Å of Ti and 1500 Å of Au were deposited on both sides of the diamond plates by thermal evaporation at room temperature. The top surface had two rectangular electrodes (2 mm × 1.1 mm) and the bottom surface had one square (2 mm × 2 mm) electrode. Post evaporation, the samples were annealed in vacuum at 600 ^{o}C for 2 hours. This process helps Ti to form a carbide, which results in good adhesion and formation of ohmic contacts. Finally, gold-plated aluminum wires were attached to the electrodes using silver paint, connecting them through transmission lines on a printed circuit board to a current amplifier with coaxial cables. Figure 3.1 shows the top surface (surface which faces the beam) of the diamond detector, wired to external cables.

The diamond plates with electrodes on both sides, were placed into custom made mounts. The detector mount was placed inside an ultra-high vacuum chamber in the beam`s trajectory. The diamond electrodes were connected to a current-sensitive low-noise amplifier[46] with 2.3 GHz bandwidth and +38 dB gain, through coaxial cables. The output of the amplifier was recorded at a digital oscilloscope. A schematic of the basic operation of the detector was shown earlier in figure 2.3 of chapter 2.

A third diamond sample was used in this experiment for comparison as a reference sample. This electronic grade 3.0 × 3.0 × 0.5 mm^3 diamond sample was purchased from a different vendor. Square electrodes (2 mm × 2 mm) were deposited on both sides of this diamond for transient current measurements. This particular sample was never exposed to the radiation beam; hence it retained its pristine nature.

3.2. Irradiation of diamond detectors by Swift Heavy Ion (SHI) beams

As mentioned earlier, the detectors were made of two different kind of diamond sources, one batch from diamond grown at MSU (samples are named as GYJ 148A, GYJ 148C) with nitrogen impurity level above few 100 ppb, and the other batch was from commercially available electronic grade diamond (commercial diamond-2) with low nitrogen impurity. To understand the detection process and gradual degradation, the detectors were exposed to beams of ^{124}Sn and

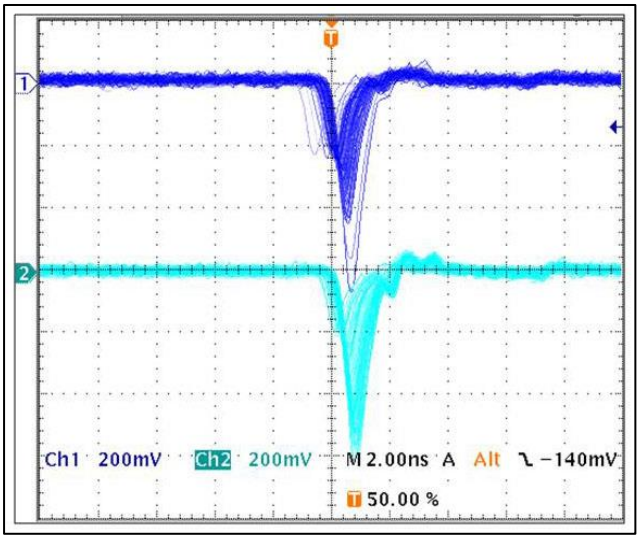

Figure 3.2. Signal captured from lab grown SCD detector (GYJ-148C) irradiated with ^{96}Zr beam. (The upper signal represents the response of heavily irradiated segment and the lower signal shows response of lightly irradiated segment)

^{96}Zr ions with an energy of 120 MeV/u accelerated at the Coupled Cyclotron Facility at NSCL, MSU. The intensity of the beam was varied from 10^2 particles/s/mm^2 to 10^6 particles/s/mm^2 by suitably changing attenuator foils in the injection line of the cyclotron. The range of ^{124}Sn ion beam is 1.95 mm for diamond and for ^{96}Zr ions, it is 2.25 mm. The approximate thickness of the lab grown samples are 0.7 mm. The energy loss is 3802 MeV for ^{124}Sn beam with 89.31 MeV/u remaining energy and 2395 MeV for ^{96}Zr beam with energy left as 95.02 MeV/u.

The signal from a detector made of MSU-grown diamond (GYJ-148C) irradiated by the ^{96}Zr beam, captured at the oscilloscope, is shown in figure 3.2. The maximum applied bias field for lab grown diamonds (GYJ 148A & GYJ 148C) were set between ±0.65 V/μm to ±0.85 V/μm. However, for the commercial diamond, to avoid any saturation by the preamplifier, the maximum applied field was limited by ±0.10 V/μm. In figure 3.2, the signal from the heavily irradiated segment is shown in channel-1 and the lightly irradiated part at channel-2. This shows an ensemble of multiple traces (where each trace is generated from a single particle) with a pulse width of ~ 2

ns. The amplitude in the channel-1 (with most probable charge generation, in the dark band) dropped partially as compared to channel-2 due to the onset of degradation from the damage created by the beam in the heavily irradiated segment.

The collection of screenshots of the oscilloscope at a different time (i.e. after a certain fluence) is shown in figure 3.3. The graph measures the signal amplitude at different applied bias voltages to estimate whether any change in the amplitude has happened.

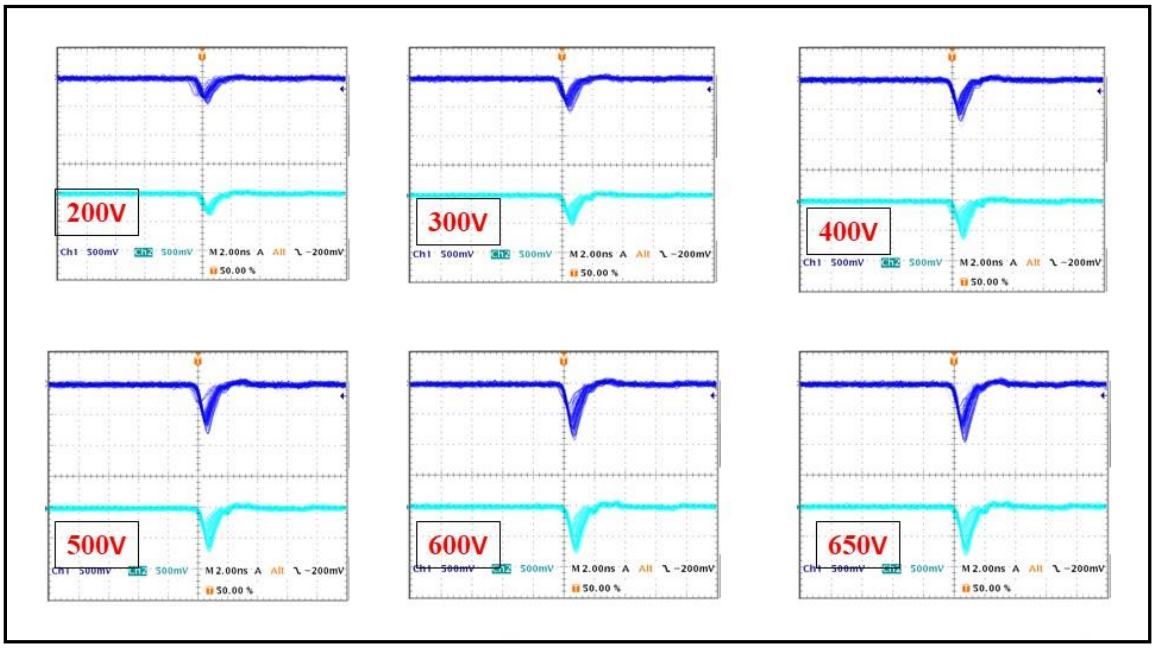

Figure 3.3. The output voltage from lightly irradiated (dark blue) and heavily irradiated (cyan) after a certain particle fluence (2.77×10^{12} particles/cm^2) for different bias voltages

The maximum signal amplitude for both lightly irradiated (dark blue) and heavily irradiated (cyan) and their ratio are used as a corresponding figure of merit to estimate degradation, which will be discussed in the next section.

3.3. Results of beam irradiation on diamond detectors

Figure 3.4 shows signal variation versus applied detector bias at four different fluence levels for lightly irradiated and heavily irradiated segments. As seen in the bias scan-4, the red curve representing the signal from heavily irradiated segment, falls off by a large margin from the signal of the lightly irradiated curve.

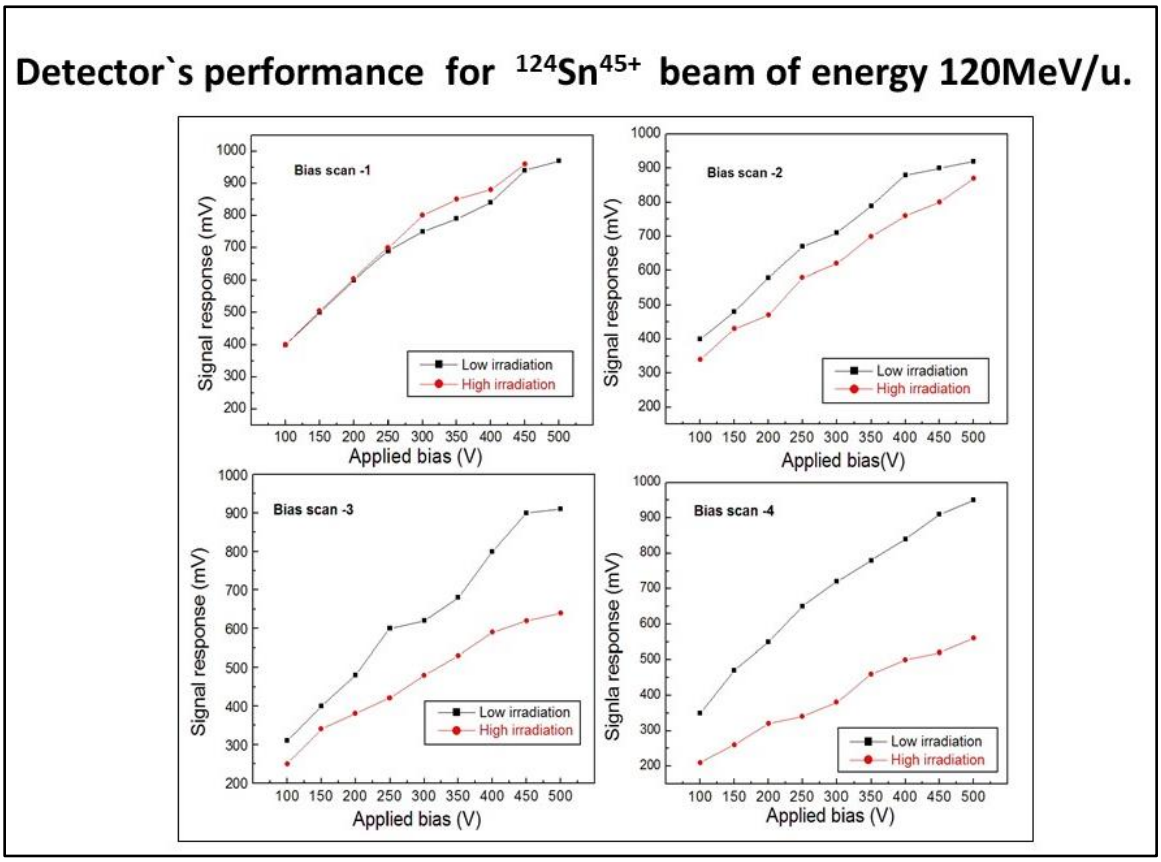

Figure 3.4. The output voltage measured at different time (with a range of bias voltages) during irradiation from heavily irradiated segment (red curve) vs lightly irradiated segment (black curve)

A ratio of the signal strengths (i.e. output voltage), as calculated at the highest bias voltage to define the relative signal, is used to create the degradation curve shown in figure 3.5.

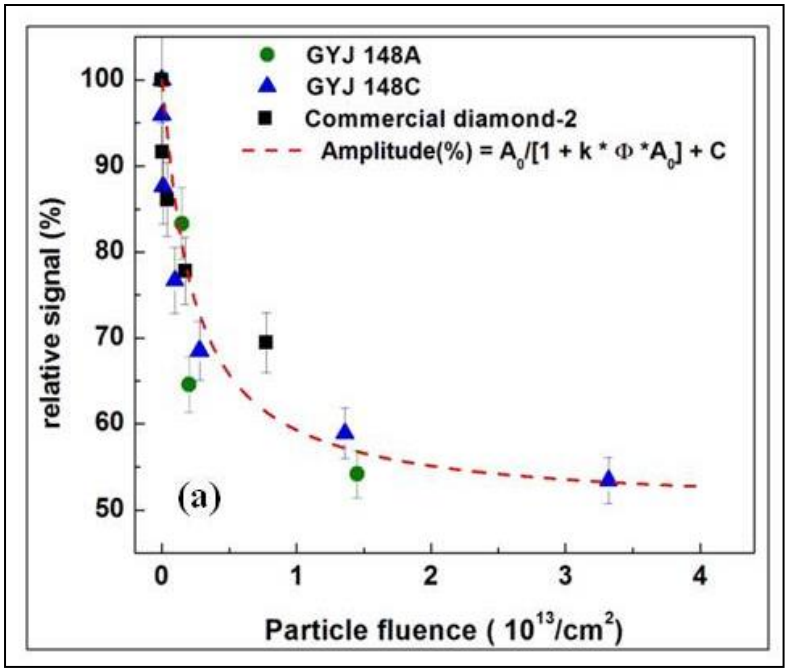

Figure 3.5. Relative signal drop of detectors over particle fluence

The relative drop of signal (at a maximum applied field ~0.65 V/μm) in the heavily irradiated segment as compared to the lightly irradiated segment is plotted as a function of particle fluence in order to understand the degradation of the detectors. This plot is built on the assumption that the amplitude of the output signal from the detectors (made from diamond plates of nearly same thickness but different quality) reflects the charge generated in the material, and therefore the drop of signal is directly caused by the rise of defects/trapping inside the volume exposed to the energetic beam. Figure 3.5 shows the relative signal (%) drop in the heavily irradiated segment for the two MSU-grown diamond samples (GYJ-148A & GYJ-148C) and the commercial diamond-2. The detector made of the MSU-grown diamond (GYJ-148A) was irradiated by a ^{124}Sn beam, whereas the other two detectors made from MSU-grown diamond (GYJ-148C) and commercial diamond-2 were irradiated by ^{96}Zr.

For the detectors fabricated from MSU-grown diamonds the signal dropped to near 55% after the same amount of fluence. A parametric equation [47] has been used to describe the scenario

(f)

as;

$$\text{Amplitude}(\%) = \frac{A_0}{1 + k \cdot \varphi \cdot A_0} + c$$

where A_0 represents the initial signal amplitude percent at the beginning of irradiation, φ represents the particle fluence the detectors are impinged with, parameter k is the damage constant and c is the offset. The hyperbolic fit (shown as dotted line in figure 3.5) appears as a good fit on the experimental points with the damage constant k as 0.88×10^{-14} $V^{-1}cm^2$.

In the study of radiation hardness of diamond detectors by RD42 collaboration group, the distribution of charge collection distance (CCD) was measured with particle fluence for different proton beam energy. With a parametric equation of the same kind, the damage constant was reported as k (by RD42 for protons) $\sim 10^{-18}$ μm^{-1} cm^2 for both polycrystalline and scCVD.

Chapter 4. Post irradiation characterization of diamond detectors

As discussed earlier, the swift heavy ion beams initially loose energy due to ionization loss. However, beyond a certain point the beams gradually reach an energy regime where most of the energy goes into non-ionizing energy loss and eventually end up of within a narrow range of depth causing atomic displacement. A single incident particle can initiate a chain of primary and secondary interactions and end up creating defects (vacancies, interstitials, Frenkel pairs) or otherwise adding strain to the material. In many cases the diamond sample itself has some traps already present at its pristine stage and the heavy ion beam irradiation triggers formation of further cascade of damages inside. Inside the atomic structure, some of the sp^3 bonds may reshape to a stable form of sp^2 bonds. Therefore, this change in the structure (both physically and chemically) disturbs the electronic properties of the diamond. Impurities can also form inside a material when the incident ion picks up the necessary number of electrons to become neutralized and therefore settling as a foreign species inside the host structure.

The effect of radiation induced damage can be investigated by using the transient current technique (TCT), which measures the charge transport properties of semiconducting material. It is also worth looking at the extent of damage in the material and at the interface of the electrodes by measuring the leakage current. In general diamond shows extraordinarily low leakage current compared to silicon based devices. One of the major indications of radiation damage in silicon based detectors is the increase in leakage current. Diamond can maintain very low leakage current even after significant radiation induced damage.

4.1. Electrical characterization

This section presents the electrical characterization techniques to determine the effect of the beam irradiation on charge transport properties of the single crystal diamond.

4.1.1. Transient current technique

The transient current technique (TCT) is used to measure the charge transport properties of pristine and radiation beam irradiated semiconducting samples. A metal-semiconductor-metal capacitive structure is configured (the same used for the detector) to carry out this experiment. The TCT technique is a measurement of the current generated due to drift of free carriers under the influence of an external electric field. In this experiment, ionized particle generated free charges travel from one side of the sample to the other side under the influence of an external electric field. The shape of the current pulse depends solely on the properties of the material under test. Important parameters for particle detectors, like drift velocity, carrier mobility, carrier lifetime and field distribution can be analyzed from this measurement. Once hole and electron charges are created near one side (electrode) of the sample either an electron or hole charge cloud, based upon the polarity of the applied field, will drift due to the electric field to the other electrode. A rectangular signal versus time is generated during the time it takes for the charge cloud to reach the farthest away electrode when minimal trapping occurs. The nature of the current signal can be expressed as [43]

$$i_{e,h}(t) \propto e^{\left(\frac{t}{\tau_{eff(e,h)}} - \frac{t}{\tau_{(e,h)}}\right)} \quad \text{(g)}$$

The first term in the exponent relates to the contribution from the effective space charge and the

second term represents the exponential decrease of current due to charge trapping. In a diamond sample, with significant charge trapping, the current signal is described as

$$i_{e,h}(E,t) = \frac{Q_0}{d} \cdot v(E) \cdot e^{-t/\tau_{(e,h)}} \qquad (g)$$

where Q_0 is the initial generated charge, d is the sample thickness, v€ is the drift velocity and $\tau_{(e,h)}$ is the effective trapping time of respective carriers. The trapping centers inside causes the amplitude to drop exponentially. Any non-uniform space charge distribution will lead to a non-uniform field distribution within the sample. Figure 4.1 shows the expected form of transient current shapes of different qualities of diamond [36].

As seen in figure 4.1 the generated charge reduces exponentially for a pcd sample or samples where there is already substantial traps present. The flat top signal represents drift of charges in very high-quality diamond with uniform electric field.

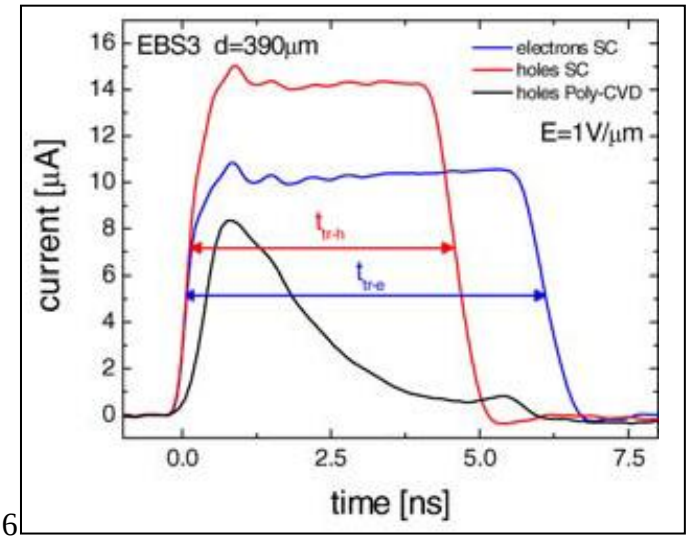

Figure 4.1. Transient current signal shape for different quality of diamond [36]

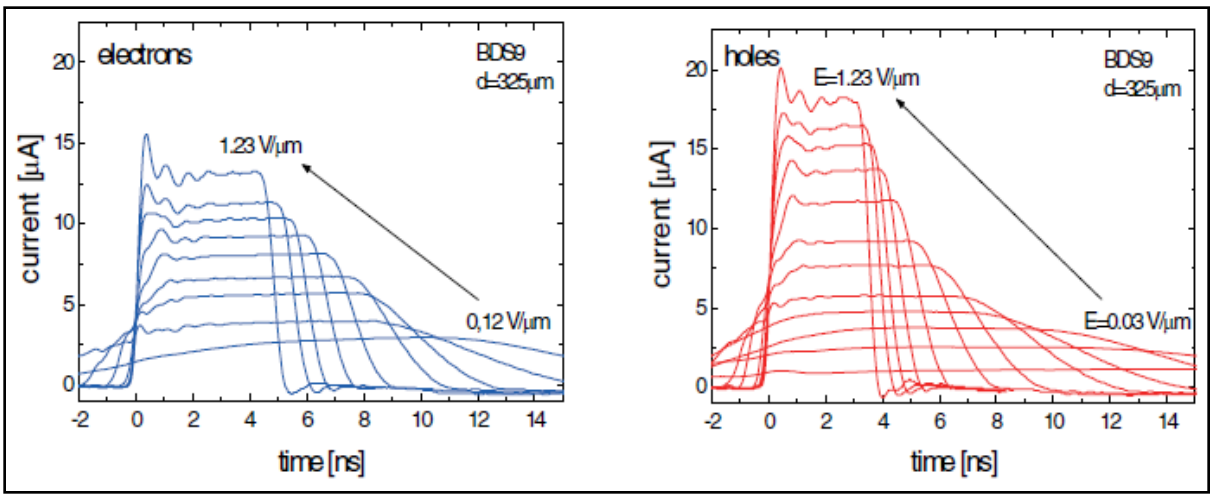

Figure 4.2. Transient current signal for electron and holes from a single crystal diamond [36]

The shape of the signal versus time partly depends on the type hole-electron pair excitation source used to ionized charges at one side of the sample, e.g. for laser induced charges the field will get modified by the high density of charges leading to a space-charge-limited current flow regime. For a weak source like α-particle, the low density of charges ensures that TCT signals are generated in space-charge-free regime. However, the quality of the diamond (defects, impurities) is more crucial in guiding the shapes of TCT signals. Figure 4.2 shows the transient current signal at different electric field for both carrier types in a high-quality single crystal diamond [36].

In the current work, a ^{232}U α-particle source of 5.4 MeV energy was collimated through a 1 mm diameter hole on top of selected sections of the irradiated and pristine detectors. There was a 13 mm air gap between the source and the sample, which amounted to an energy loss of 1.28 MeV in the air. The α-particles penetrate 8–10 µm into the diamond samples, a much smaller distance compared to the sample thicknesses (530–550 µm). The particles impinged at a low rate of 6.3×10^2/s/cm^2 and the responses from the detector were collected in a short duration of 5~7 minutes time to minimize polarization effect. The electrodes of the detector were connected to a

broadband current amplifier (Cividec Instrumentation: C2HV0081, 2GHz/40dB) and single traces were stored with a Tektronix (TDS 3054B) oscilloscope.

To understand the transient current signal in the current set up, a commercially available electronic grade single crystal diamond was tested at first. This particular diamond was designated as commercial SCD-1 and held at its pristine stage in the entire study, i.e. this sample was never irradiated with any ion beam. This sample was used as a reference sample for the entire study. The measured voltage $V_m(t)$ was converted to a transient current output $i_m(t)$ by the following equation (i)

$$i_m(t) = \frac{1}{A_{amp}\, R_{in}} \left[R_{in} C_d \frac{dV_m(t)}{dt} + V_m(t) \right] \qquad \text{(i)}$$

The major uncertainty in the measurement appears from the two parameters A_{amp} and R_{in}, which were calibrated with the output of a charge-sensitive amplifier (Cividec Cx-L, with sensitivity 12 mV/fc). The calibration values have been used to convert for all the samples currently under study.

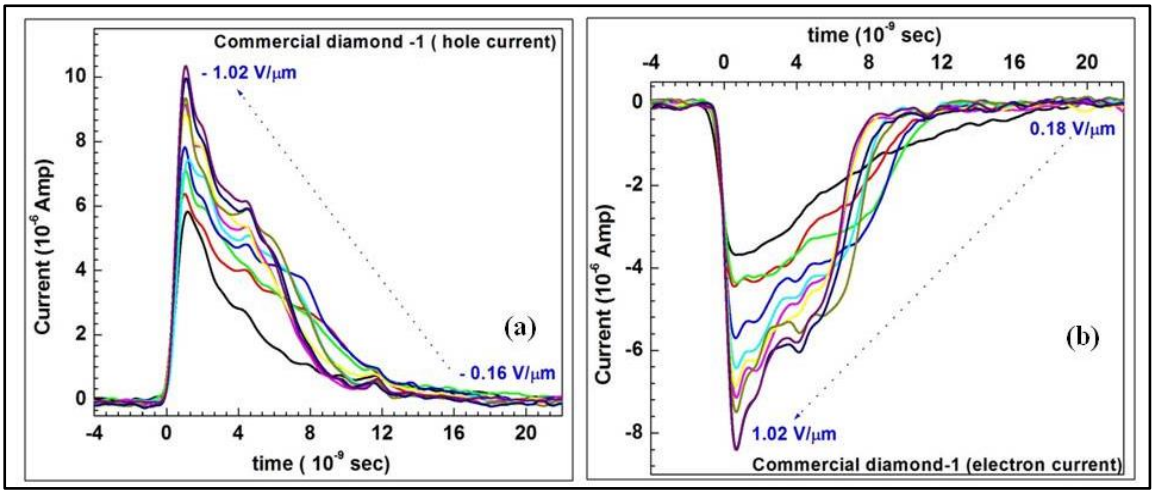

Figure 4.3. Transient current signals from commercial diamond -1

As observed in figure 4.3, for both type of charges the amplitude drops gradually during the drift motion. This could either happen as the diamond sample may have impurities causing charge trapping or there could be strain present in the sample causing polarization of the field. A birefringence study of this pristine sample has shown reasonable strain present in the sample. Holes get trapped more in the sample than electrons as shown by the amplitude of the hole current decreasing faster versus time. The initial current amplitude (at t=0+) depends on the amount of energy that was deposited, and the equivalent charge generated in the sample, the applied external field and the mobility of the charge carriers.

TCT studies were also done on an irradiated commercial substrate (^{96}Zr beam of energy 120MeV/u) of slightly different type (higher nitrogen impurity than commercial diamond -1 but lower nitrogen than MSU grown samples). As mentioned in the substrate preparation section above, the substrate was prepared by depositing two rectangular electrodes on top of the substrate, one electrode section was where the swift heavy ion beam was directly focused on and named as heavily irradiated segment, and the other section is only irradiated by the less intense halo of the approximately Gaussian shaped beam profile and been termed as lightly irradiated segment. The direct beam is expected to induce more defects in the area of the heavily irradiated segment and therefore disturbing the charge transport more in that segment. The next two figures give examples of the transient current signal of the two segments of commercial SCD-2.

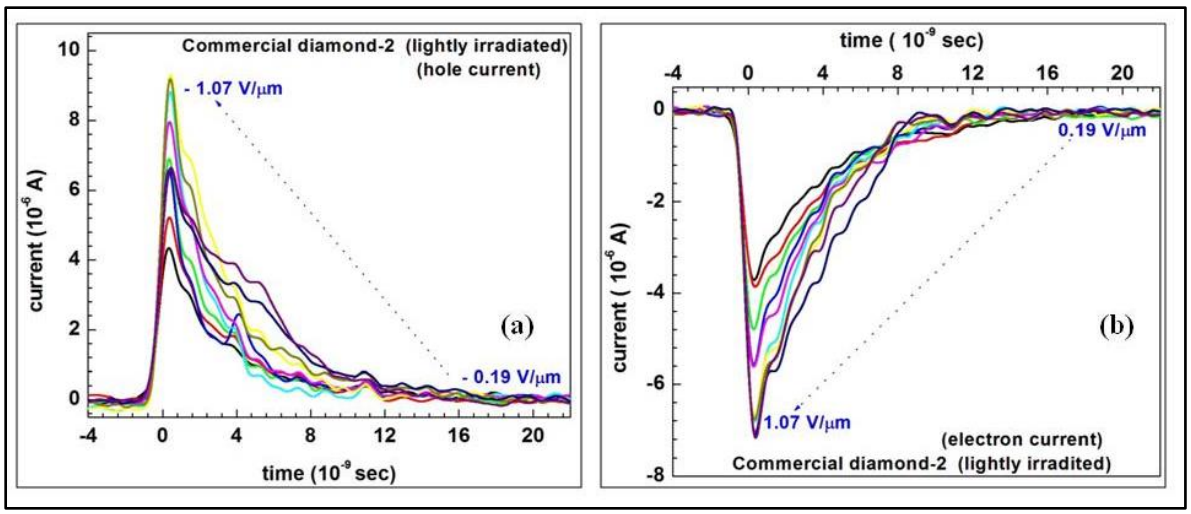

Figure 4.4. Transient current signal from lightly irradiated segment of commercial diamond-2

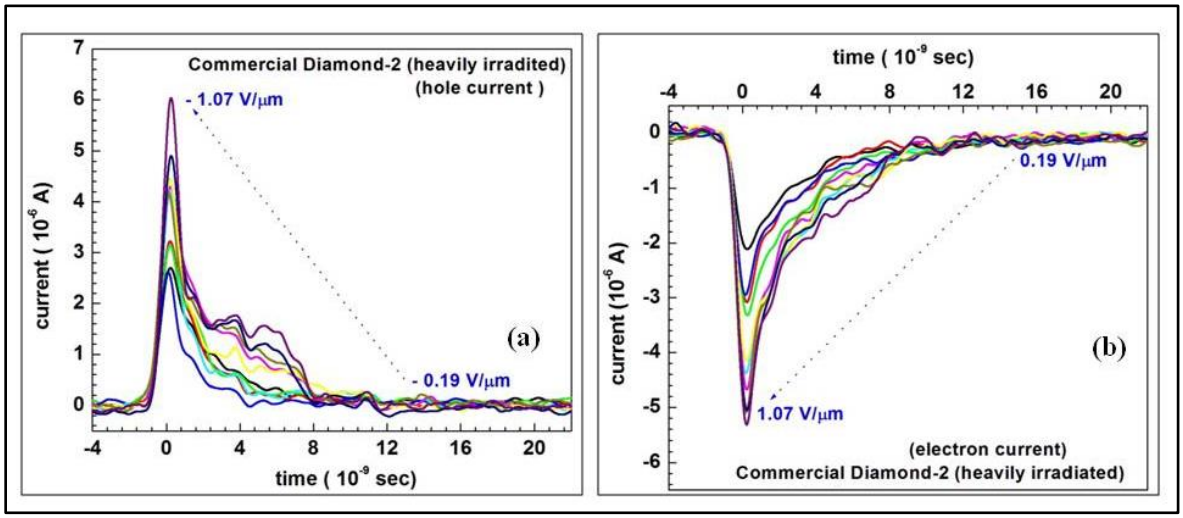

Figure 4.5. Transient current signal from heavily irradiated segment of commercial diamond-2

As observed, comparing figures 4.4 and 4.5 the transient current signals of the more heavily irradiated diamond region are narrower in nature and have a sharper exponential decrease in amplitude versus time. Specifically, in figure 4.5, which shows the effect of direct beam damage (heavily irradiated), the irradiation causes more trapping centers or defects to be produced yielding a narrower pulse signal, i.e. the drop of approximately 50% of the amplitude happens more rapidly

in the heavily irradiated segment as compared to the lightly irradiated one. This indicates that in the heavily irradiated segment the damage is due to the beam irradiation. The beam induced damage also shows slightly smaller amplitude for both electron and hole generated currents at time t=0 as compared to the lightly irradiated segment. The effect of the beam induced damage can be further quantified by calculating the collected charges (Q_{col}) of the different segments of the commercial diamond-2. The collected charge is found by defining a suitable time (by using figure 4.3, 4.4 and 4.5) and integrating the current pulses over time as given in equation (j)

$$Q_{col} = \int_{t_{start}}^{t_{end}} i_m(t)\, dt \qquad \text{(j)}$$

where t_{start} and t_{end} are defined as the time the current signal rises above and drops below a threshold level respectively. The calculated charge by the above integral is plotted with respect to the applied field as shown in figure 4.6.

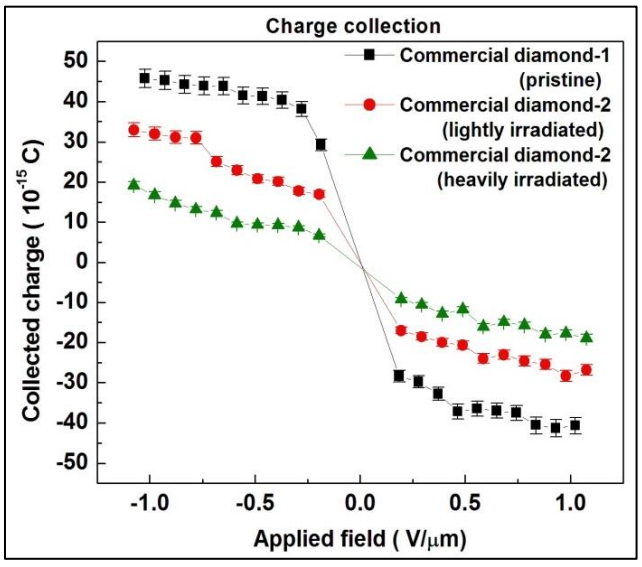

Figure 4.6. Charge collection versus applied field

The overall charge collection was calibrated by using a charge sensitive amplifier (Cividec Cx-L, CxL0051). For the commercial diamond-1, charges saturated beyond an applied field ± 0.5 V/μm, however for the other diamond sample charge collection was at lower values due to the presence of traps. For calibration, the charge sensitive amplifier was used at higher fields for commercial diamond-1. The collected charge was recorded at 0.60–0.65 V/μm and averaged over a number of measurements. The gain of the amplifier was separately measured to estimate the $A_{amp.}$ Further with the collected charge value, the product ($A_{amp.}R_{in}$) was adjusted and applied to convert the measured voltage to current $i_{m.}$ for the generated signal from all samples. The degradation created by the swift heavy ion beam is quite evident as the charge collection in the heavily irradiated segment was less than 20 fC (within the applied field range) as compared to lightly irradiated segment where the collected charge is close to 30 ~ 35 fC.

The ion beam deposits its energy in the material, which will primarily ionize and create electron-hole pairs. However, some the SHI deposited energy will initiate dislocation of atoms from the lattice. The dislocated atoms (both carbon and especially any impurities) can result in traps being created.

Finally, a comparison of transient signal generated from non-irradiated segments of MSU and commercially available electronic grade is shown in figures 4.7 and 4.8.

As it is evident that the charge drift times are extremely short for MSU lab grown diamonds (less than 2 nano second).in comparison to the commercially available electronic grade diamonds. This clearly establishes the facts that the lab grown diamonds have more charge traps arising from excess nitrogen-related traps or other defects.

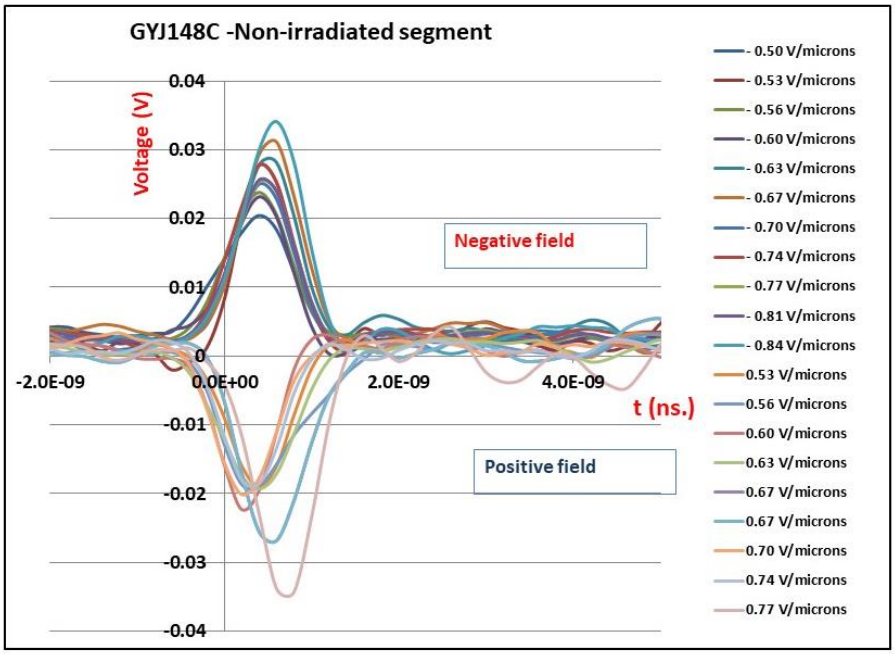

Figure 4.7. Transient signal generated from a MSU lab grown diamond

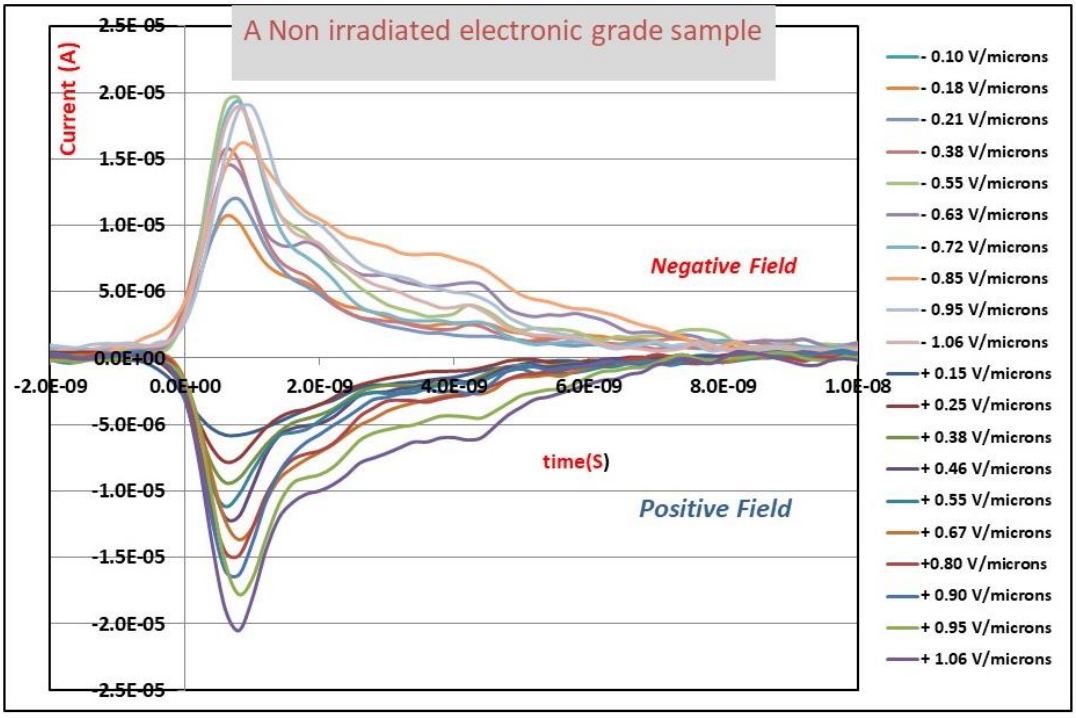

Figure 4.8. Transient current signal generated from a non-irradiated commercial electronic grade diamond

4.1.2. Leakage current test

As a wide bandgap material, intrinsic diamond also shows very high room temperature resistivity. In addition, the energy required to create free carrier is also very high, hence altogether diamond acts nearly like an insulator in its undoped condition. Hence in general the leakage current associated with a good quality of single crystal diamond material is very low ($<10^{-12}$ A). The leakage current characterization of a particular diamond sample becomes useful in finding a safe biasing range where noise level stays within a certain lower limit. The leakage current can be generated both due to the bulk properties as well as the surface` condition. The leakage current from the bulk arises due to thermally activated carriers. These carriers can generate from trap levels inside or occasionally from defects that penetrates deep into the substrate. Hence a low leakage current, which is signature of a good quality of diamond is desirable for its usage for any electronic applications. Figure 4.9 shows an I-V characteristic of a pixel polycrystalline detector [48]. Polycrystalline diamonds are used as beam loss monitors in accelerators, hence a relatively high leakage current still makes it quite applicable. However, in some cases polycrystalline diamonds show erratic distribution or rise in leakage current, eventually settling to a very high leakage current. Occasionally an applied magnetic field can alter this behavior as studied by Muller et al [49].

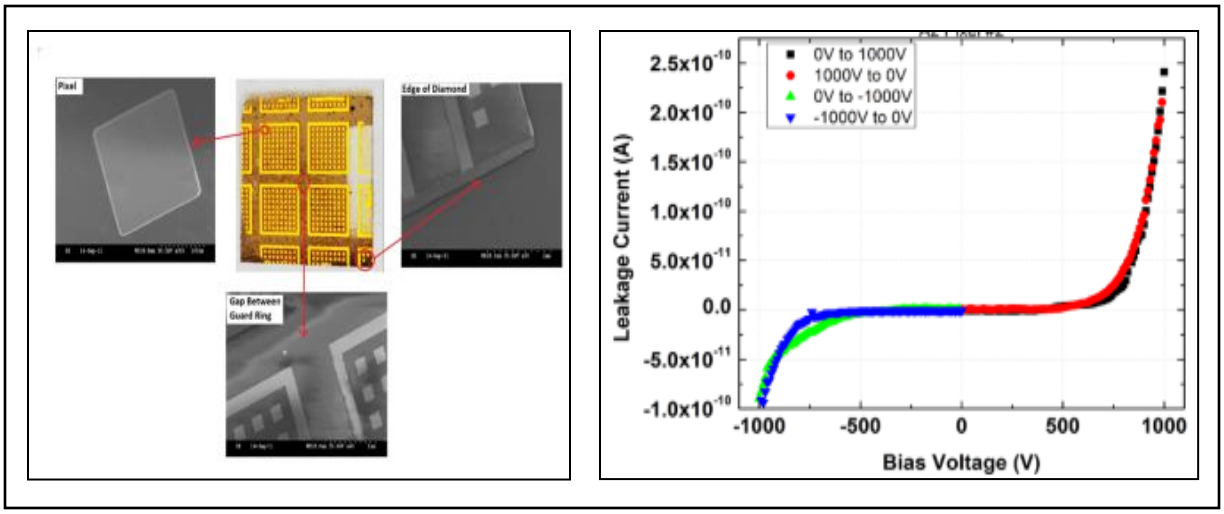

Figure 4.9. Leakage current in a polycrystalline pixel detector [44]

In this experiment a Keithley 6485 picoammeter is used to measure the leakage current for both the lightly and heavily irradiated segments of the commercial diamond-2. The externally applied voltage was varied, and the maximum was limited to 550 V.

The leakage current test was conducted in the commercial diamond-2, in both the lightly irradiated and heavily irradiated segment. In both cases the same contacts (Au and Ti ohmic) used during beam radiation test, were used to carry out the test. The following figures show the nature of leakage current`s distribution collected at different stages from the two segments.

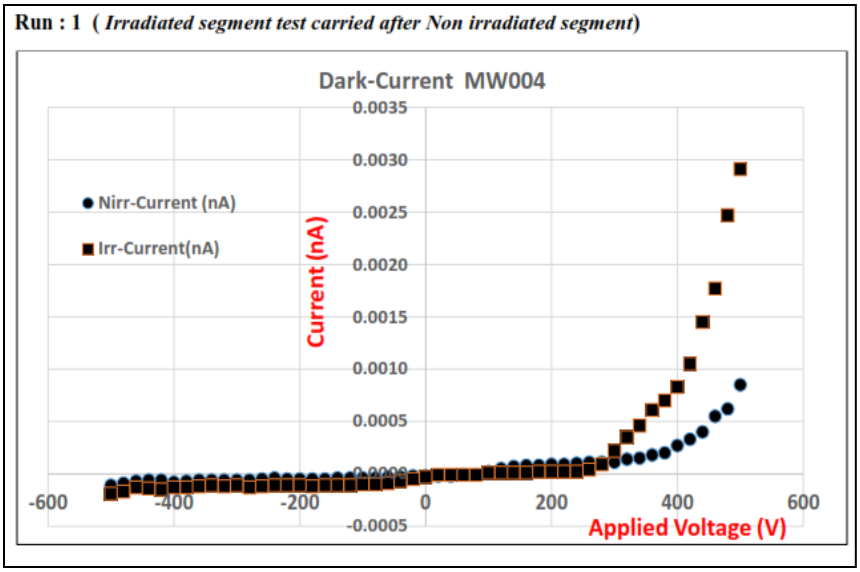

Figure 4.10. Leakage current measurement on commercial diamond-2

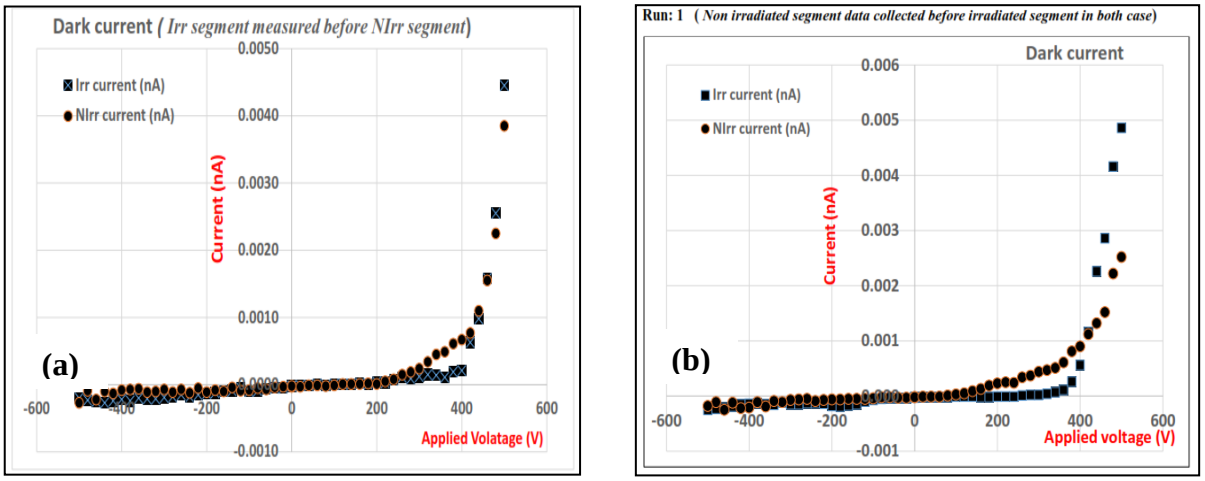

Figure 4.11. Repeat run of leakage current measurement (a & b) with segments measured in different orders

In the first set (figures 4.10 & 4.11(a)) the leakage current of heavily irradiated segment (noted in figure as Irr) was measured, followed by measurement of the lightly irradiated segment (or non-irradiated segment, noted as NIrr) where as in the other set (figure 4.11 (b), the order was reversed, i.e. the lightly irradiated segment was looked into before the other segment. In all cases

the heavily irradiated segment showed marginally higher leakage current after the increase in current for the positive polarity, which only appeared in one polarity of the field. Also, in the second set of data the current rises to an order less than it happened in the first set, which might have happened due to light in the background. A next set of experiment (fig 4.12), where the leakage current test in the heavily irradiated segment was carried out first shows almost no difference (other than the current in lightly irradiated segment between 300v-350 v is higher compared to its other part) between the distribution of the two segments. In all cases the I-V curve shows very similar nature to leakage current distribution of a polycrystalline diamond (as shown in figure 4.9). The commercial diamond-2 has high impurities and trapping centers, which could release free charges over a certain high field, which eventually shows a sharp rise of current. A separate measurement has been done to verify whether the rise in the current is due to any transient effect. In multiple trials of test the leakage current show similar distribution i.e. a polarity dependent signature of a rise. Also, the leakage current in all the tests stayed within the range of 10^{-12} A, showing the quality of the commercial diamond-2 sample after irradiation. There was no degradation of the contacts observed under optical microscope.

To have a better understanding in the rise of the current, the leakage currents were measured in the presence of strong light on the sample. The background was turned dark and a red LED was used to illuminate the samples for a short time. Figure 4.12 shows the leakage current measured while the sample is illuminated.

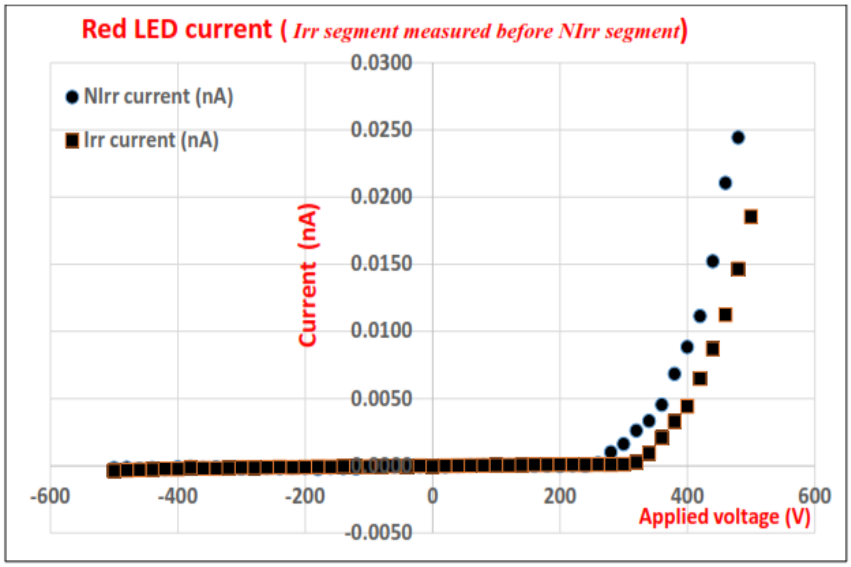

Figure 4.12. Leakage current measurement with sample illuminated with red LED

A comparison of the current axis among the two figures (4.11 & 4.12) clearly shows that some traps get activated by the red LED. These are shallow level traps which are located within 1.5 eV of the conduction band and get activated with the applied field in presence of the illumination. As it is found that the field required for the activation and the total rise is nearly the same for both lightly irradiated and heavily irradiated segments of the diamond.

In an extension of this study on the transient current response, the rise of current at three different high fields was studied to understand whether the spike of the current drops back after some time or not. To realize this the applied voltage was increased to three different high values above 300 V (as it is seen that the current rapidly increases after 300 V). The following figures (figures 4.13 & 4.14) show the rise and effective time taken by the leakage current component to drop at three different voltages at 365 V, 425 V and 465 V respectively, after the light (LED) was turned off.

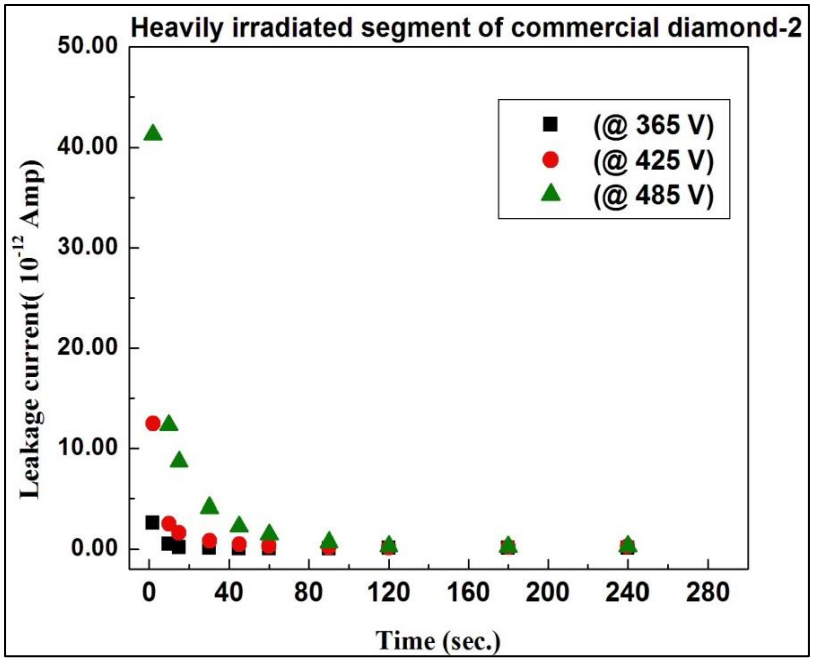

Figure 4.13. Transient response of heavily irradiated segments of commercial diamond 2

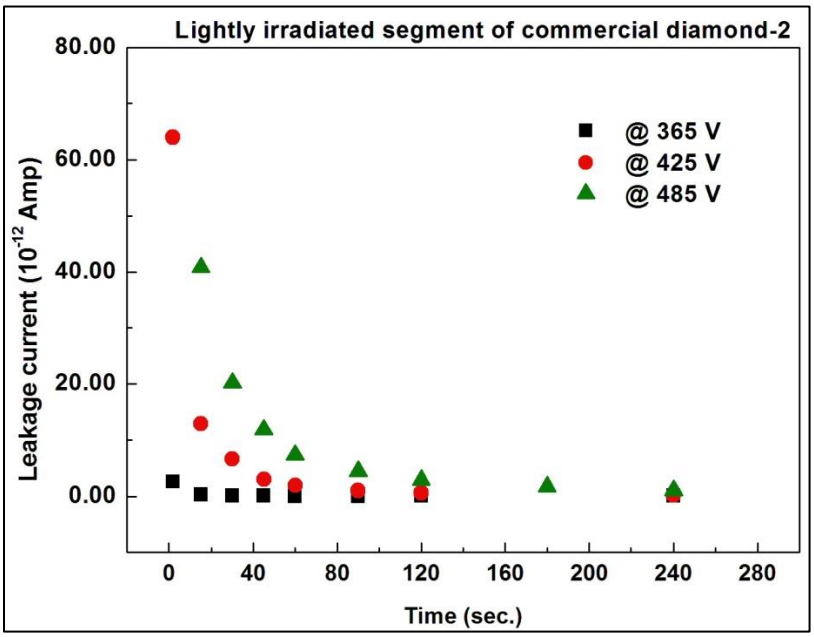

Figure 4.14. Transient response of lightly irradiated segments of commercial diamond -2

Figures 4.13 and 4.14 reveal that the transient component of the leakage current slowly fades to almost zero after some time. However, for heavily irradiated segment it takes slightly shorter time for the transient component to decay as compared to the lightly irradiated segment, which might be due to presence of additional defects in the heavily irradiated segment caused by the beam. Therefore, this experiment shows how heavily irradiated segment responses to visible light activated traps and the typical time required to normalize.

4.2. Optical characterization

A pristine quality single crystal diamond is an optically transparent material throughout the visible range and throughout large portions of the infrared region. However, any impurities both deliberately or unintentionally added affect the optical properties, which therefore makes it a very interesting technique to study the quality of diamond samples. Nitrogen is the most familiar impurity present in diamond and based upon the quantity of nitrogen the diamond can appear as pale yellow or brown in color. Hence different forms of nitrogen impurities could be studied by looking at absorption peaks in the visible and infrared range.

4.2.1. UV-Vis spectroscopy

In UV-VIS spectroscopy optical properties of materials (e.g. absorbance, transmittance) are measured within the range of 200-400 nm (uv) and 400-800 nm (visible) light. This method helps both in qualitative and quantitative analysis of solids and liquids (or compounds present in liquid). The basis of this method relies on Beer Lambert`s law [50] for analyzing the absorbance of a material, which is a unique characteristic for any material under test. One can derive the

concentration of a molecule in a solution from the absorbance, however this has limitation for higher concentrations. Diamond is transparent in the near UV to visible region at wavelengths longer than its strong absorption peak at 225 nm (due to its indirect band gap). Diamond also has absorption peaks in infrared region 2500 -6000 nm.[2,51].

For any solid material a rough surface adds up as a source of scattering and therefore needs to be accommodated for as a correction to figure out the transmittance or absorbance. Therefore, an improper surface finishing can cause a significant signal loss and therefore end up showing a lower transmittance. This is also an issue related to transmittance of polycrystalline diamond, where light scatters at grain boundaries. Internal strain can also cause higher absorbance, which could be partially reduced by high temperature annealing. Otherwise a high-quality type-IIa diamond with a smooth polished surface shows high transmittance beyond the characteristic cut-off wavelength of 225 nm.

In this study a Perkin-Elmer UV-VIS spectrometer (LAMBDA-900) is used for measuring the optical properties of different diamond samples. A slit width of 3-5 mm has been used (based upon the noise present) with variable integration time at different segments of the wavelength. Figure 4.15 shows the absorbance and transmission spectra of a high-quality commercial diamonds along with the two lab grown diamond (GYJ 148 A and GYJ 148 C).

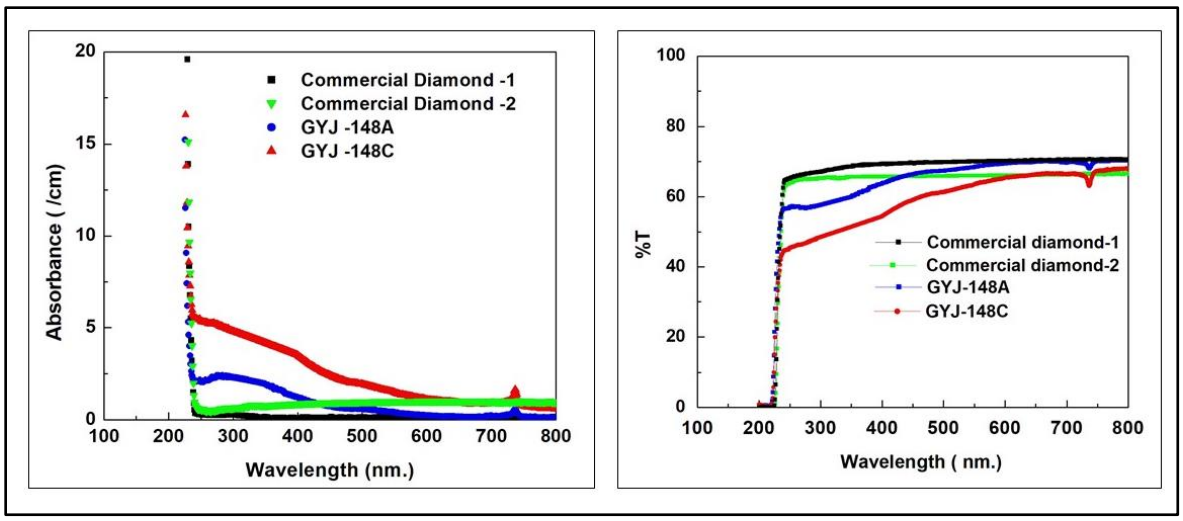

Figure 4.15. % Transmission and absorbance of different quality diamond

The commercial diamonds show almost ideal diamond characteristics, i.e. a high transmission (68-71%) throughout the uv-visible range and a sharp absorption near the band edge around 220 nm. The %T value partly varies between the two commercial diamonds (from two different vendors) due to mainly marginal difference in thickness and also the background spectra (as these data were collected on two different days), otherwise their response in general are very similar. The other two diamond samples (GYJ-148A and 148C) were grown in MSU in diamond system -IV (Reactor C configuration). These two samples have higher nitrogen content which shows up as high in the absorbance as compared to the other samples. These two samples also had a signal from silicon that may be present due to erosion of the quartz dome during growth. The signature of Si absorption appears around 732 nm in the transmission spectra. The marginal rise in absorbance for commercial diamond -2 is mostly from the instrumental error (slight noisy background collection). Next, we look into the effect of irradiation through optical characterization. Figure 4.16 shows the effect of the SHI beam irradiation after removal and cleaning of the electrodes.

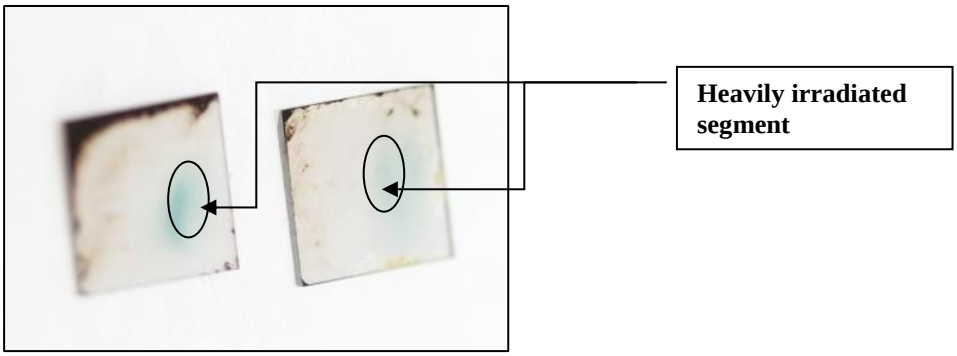

Figure 4.16. Effect of SHI beam irradiation on samples GYJ 148A and 148C

As seen in the figure 4.16 both beams (Zr and Sn) leave a similar kind of signature after a similar dose of particles. The next set of diagrams in figure 4.17 show the transmission spectra of the lightly irradiated and heavily irradiated segments separately through a small aperture (2mm in diameter). In the same scanned range there are some distinct differences seen between the two regions. For both diamonds strong absorption takes place around 350 nm, which happens due to irradiation produced defects, and the signature of the damage, i.e. a substantial drop in transmission around 650 nm and 325 nm. However, the lightly irradiated segment appears very different for

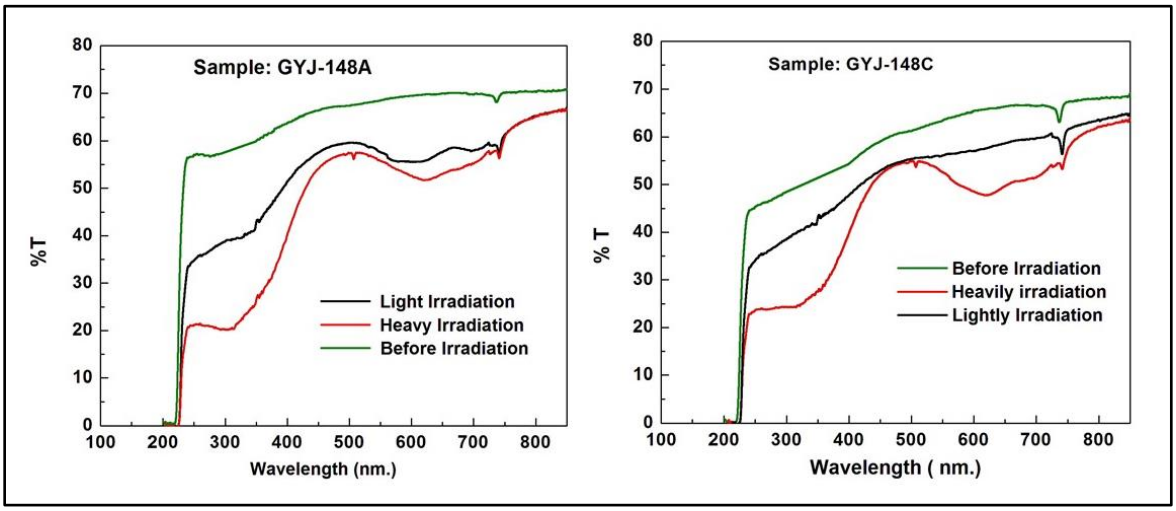

Figure 4.17. % Transmission on SHI beam irradiated samples

both diamonds. This could be due to GYJ 148C has slightly higher nitrogen impurity content than GYJ 148A as seen in figure 4.16. Hence the effect of beam halo is more prominent in GYJ-148A.

4.2.2. Fourier Transform Infrared spectroscopy (FTIR)

Fourier Transform Infrared spectroscopy is a technique where infrared (IR) radiation is passed through a sample to study the molecular absorption or transmission characteristics [52] over a selected range of photon energies (wavelengths). This method is helpful in identifying different kinds of bonds present in an organic compound. When a material absorbs IR radiation, the molecules get excited and goes to a higher vibrational state. The particular wavelength or range absorbed by the molecule is a function of the energy difference between the ground sate and the excited vibrational state, the wavelength is tagged as the characteristics wavelength of the molecule. Mostly it is the mid infrared range span in the wave number range 400 cm^{-1} to 4000 cm^{-1} that is used for this application. The advantage of the mathematical technique "Fourier Transform" is that it allows to analyze the whole range of spectrum at one shot, an interferometer is used to achieve this very fast operation.

In this experiment a sample is scanned by in Perkin Elmer spectrum one FTIR spectrometer, which can scan between wave number 400 cm^{-1} to 4500 cm^{-1}. Figure 4.18 in this section shows the primary features of diamond’s infrared spectrum.

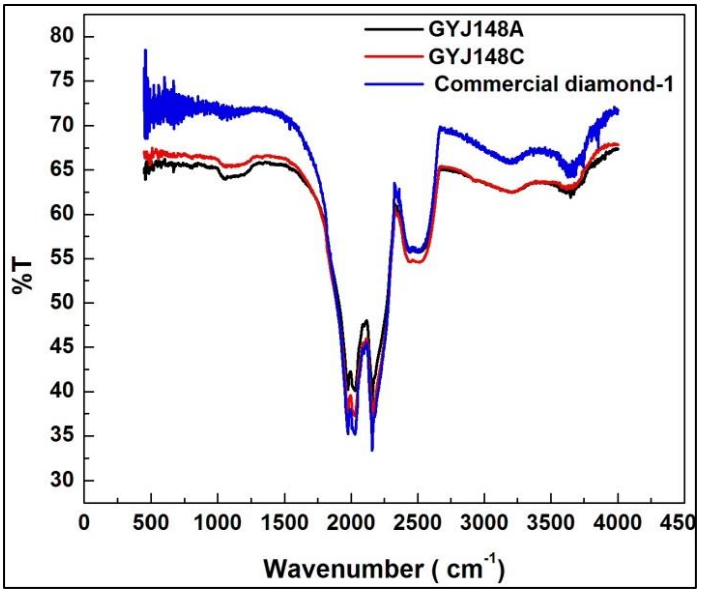

Figure 4.18. Infrared spectrum of commercial and lab grown diamonds

In figure 4.18, the infrared responses of commercial diamond-1 and the two lab grown diamonds are depicted. The strong absorption peaks present between 1900 to 2300 cm^{-1} are associated with C-C bonds in diamond [53]. The lab-grown diamonds show additional absorption around 1100 cm^{-1} which is a signature of the presence of nitrogen impurities. There are minor absorption signals at around 2900 cm^{-1} (for the lab grown diamonds) and at 3100 cm^{-1} for all the diamonds. These absorptions come from C-H_x groups. A careful selection of low methane flow concentration ensures minimal absorption in this region. Figure 4.19 shows the infrared spectrum of the lab grown samples after irradiation.

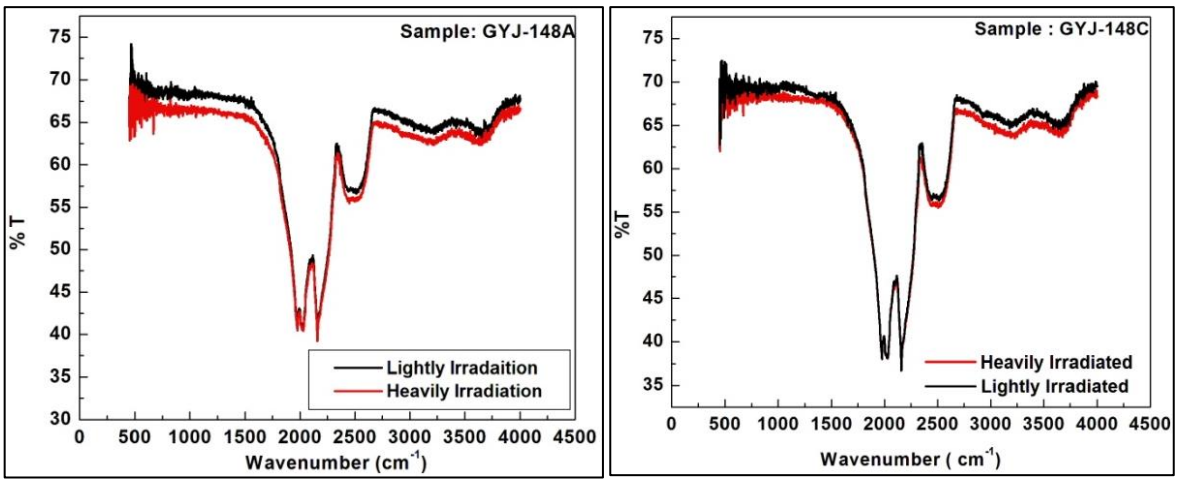

Figure 4.19. Post irradiation infrared spectrum of lab grown diamonds

It is quite evident from figure 4.19, that the beam induced damages, or any added impurities remain non-responsive in the mid infrared range, hence there is no additional absorption that appears in the spectrum.

As a conclusion from the optical studies, it is found that SHI beam over the fluence of 10^{13} particles-cm^{-2} creates some color centers in the single crystal diamond plates. Therefore, the absorption in the visible range gets affected the most, and in addition a part of the UV absorption also suffers. However, in the infra-red region the diamond retains all its characteristics.

4.3. Structural characterization

Swift heavy ions that either pass through material or stop within material often produce displacement of atoms. This displacement of atoms, if large enough, can be seen by using structural analysis of the material. In this section the analysis of beam irradiated samples by X-ray diffraction and Raman spectroscopy is performed to look for any damage that results in crystal structure deformation. In general, for any ion beam reacting with material, the effect is determined by the

ion energy, the fluence and the stopping range of the beam inside the material (or whether the beam completely passes through the material). Even though the low energy regime is more prone to cause structural damages, there is evidence that in the high energy regime where electronic stopping power is a dominating process, structural damages can happen for dielectric and semiconductor materials. At high energies the damage occurs along the path of the high energy ion, where the charged ions produce cylindrical shape of damage along the trajectory. At any time, the electrostatic energy transfers outwards to the neighboring atoms and columnar defects are formed due to the shock waves. This phenomenon is known as track formation. However, up until now there has not been any reports showing any track formation happening in diamonds. Damage that is observed is mostly at low energy ranges due to dominance of nuclear stopping power. In a recent report Garcia et al. showed detailed experimental evidence of amorphization in optical grade diamond material by irradiating with beam energies of a few MeV to a maximum of 40 MeV, which includes electronic stopping power to a maximum range of 14KeV/nm [40]. Therefore, to look for any major structural changes in the irradiated samples in this work, a high-resolution X-ray diffraction method is applied. In high resolution X-ray diffraction (HRXRD) any feature related to crystallographic planes can be measured with more precision than normal x-ray diffraction.

4.3.1. High resolution X-ray diffraction (HRXRD)

The XRD characterization for this study has been conducted with a Bruker AXS D8 system. Some detailed information about the system could be found in the attached reference [54]. The two major methods which are commonly used in HRXRD system are Ω-2θ scan and rocking curve scan. In Ω-2θ scan, one can find different set of parallel planes that are present in the sample

and the corresponding interplanar spacing. At each step the angle between the incident beam and the sample surface (Ω) is varied. The detector adjusts it`s movement to 2θ position where Ω (Theoretical value) = θ. Sharp diffraction peak appears at positions where Bragg`s law gets satisfied. This method is also helpful in studying for any stress/strain present in the material. On the other hand, rocking curve scan is more related to single crystal material analysis. It is mainly carried out to analyze the deviation of the orientation of a set of planes from its expected position.

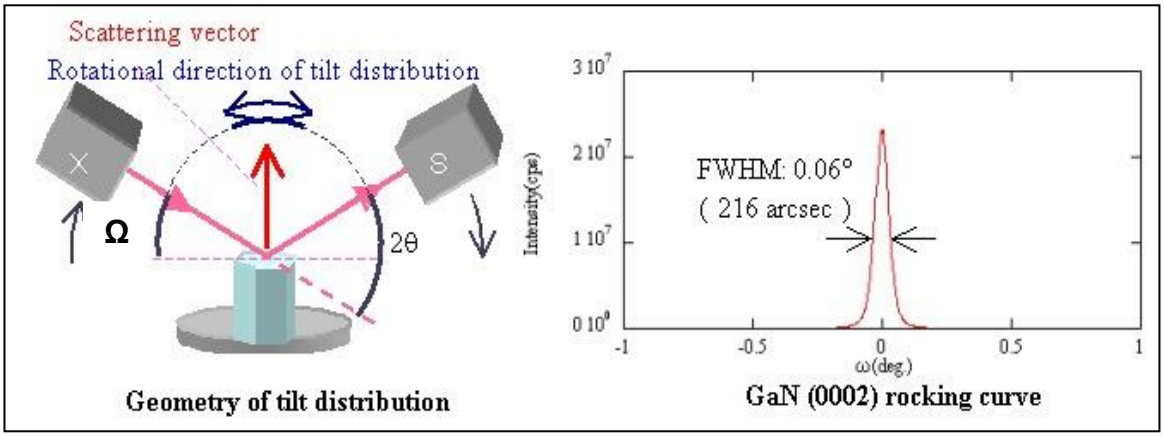

Figure 4.20. Rocking curve scan of GaN sample [54]

As shown in figure 4.20, for a rocking curve scan the sample is positioned with the beam at an incident angle Ω and the detector at the corresponding Bragg angle, 2θ.[55]. Next the sample is moved in a range of ± ω around its equilibrium position Ω, while the detector position remains fixed. For a close to perfect scenario (Ω ± ω) will be close to zero, however there could be substantial deviation if the planes are partially distorted due to strain.

In this work one of the SHI beam irradiated diamond samples, GYJ 148C was selected for a rocking curve scan at the (004) orientation. A 50 micron slit width is used towards the source and a normal nickel filter is attached at the detector end. The rocking curve scan is carried at several spots on the sample travelling from the heavily irradiated segment to the lightly irradiated segment

as shown in figure 4.21. The sample is initially aligned at Ω = 59.7550° and the detector at 2θ = 119.5101°, and in the next step it is rotated within ω= ± 5.0°. Figure 4.21 shows a schematic of the strategy followed for rocking curve scans at different (approximate) spots on the sample GYJ-148C. Commercial diamond sample- 2 is also tested as a reference for this set up. Before any rocking curve scan a y-scan of the sample is done to get an approximate range to cover by the beam spot.

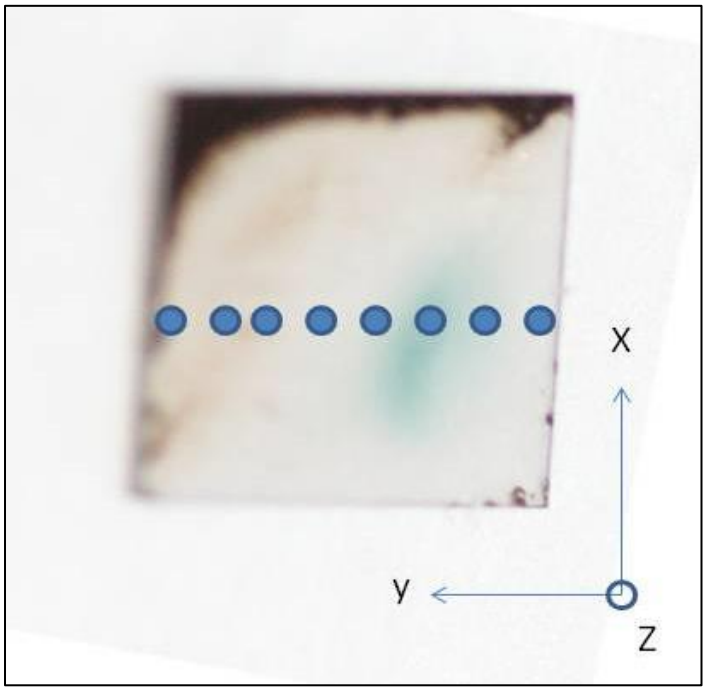

Figure 4.21. A schematic of different positions for rocking curve scan

The next set of plots in figure 4.22 shows the rocking curve scans at the different spots of the sample, as well as the full width at half maximum (fwhm) distribution. A Gaussian curve fitting tool is applied here to get the fwhm value. The figure begins with a scan at heavily irradiated segment (scan 1) and goes all the way to lightly irradiated segment (scan 12 & 13). As observed

in each of the scan there exists a small peak along a tail with the (004) peak. The appearance of the small peak could happen due to $k\alpha_2$ line from the source being present with $k\alpha_1$ line.

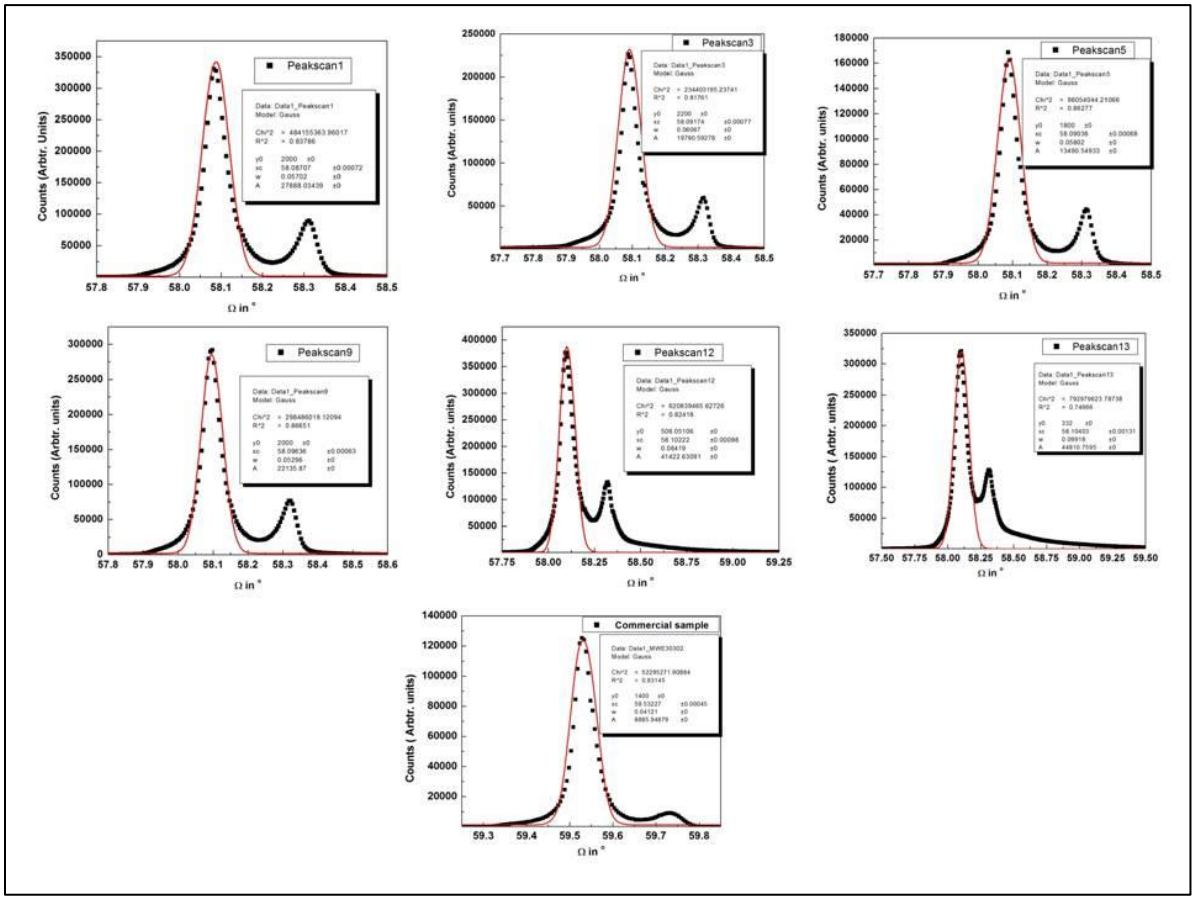

Figure 4.22. The distribution of rocking curve scan at different spots of sample GYJ-148C

The following table lists the distribution of fwhm as measured from the lightly irradiated to heavily irradiated region. The fwhm is calculated by using a best fit method of a Gaussian curve over the points by the Origin software (https://www.originlab.com/).

Table 4.1. Full width half maximum (fwhm) measured for peak (004) across the sample GYJ 148C.

Sample name	fwhm (Arc sec)
GYJ-148C scan1	205.27
GYJ-148C scan 2	216.50
GYJ-148C scan 3	218.41
GYJ-148C scan 4	216.75
GYJ-148C scan 5	208.87
GYJ-148C scan 6	193.17
GYJ-148C scan 7	199.69
GYJ-148C scan 8	222.62
GYJ-148C scan 9	194.25
GYJ-148C scan 10	236.95
GYJ-148C scan 11	240.56
GYJ-148C scan 12	298.40
GYJ-148C scan 13	357.05
Commercial diamond-2	148.35

It is evident from the table 4.1 that within the resolution limit of the rocking curve measurement set up, the fwhm show slightly higher fwhm around heavily irradiated segment (scan 2,3,4) compared to lightly irradiated segment (scan 5,6,7). This needed to be verified with further repetition of experiments and conducting the same study on the other sample. (GYJ-148A).

However higher fwhm values are observed towards scan -12 and 13 which is almost towards the edge of lightly irradiated segment. These increases could happen as the sample GYJ-148C has some visible non-diamond phases appearing in the figure 4.22.

4.3.2. Raman spectroscopy

Raman spectroscopy relies on a change in energy of a monochromatic light due to molecular vibration of atoms it is incident upon. The energy shift is realized as the characteristic of a particular molecule or a specific molecular bond existing in a test material. The Raman effect is a very weak interaction. In general incident photons get scattered elastically while interacting with a molecule. However, a small fraction of the total photons goes through inelastic scattering and hence emerge with a lower frequency (energy), this effect is known as Stokes scattering. In the other scenario where the molecule loses energy and therefore the photons end up shifting to higher energy side is called anti-stokes scattering. The chance of anti-stoke scattering is lower.

An experimental set up a Raman spectrometer is comprised of (a) a laser source (UV or visible laser), (b) a combination of different lenses to illuminate the sample, and (c) a notch filter and spectrometer to collect and analyze the scattered light and finally a charge coupled device to store the spectrum. Figure 4.23 shows a schematic of a Raman spectrometer set up.

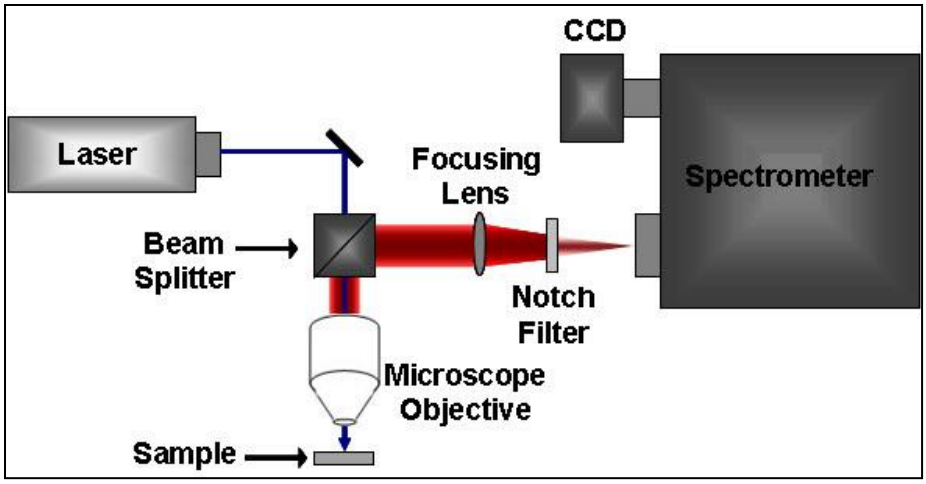

Figure 4.23. A schematic of Raman spectrometer [54]

Raman spectroscopy [56] is a useful technique to characterize radiation damage in a material. Based on the shift of the Raman peak position or its widening one can characterize the strain and crystalline quality of the material. There have been numerous reports on qualitative

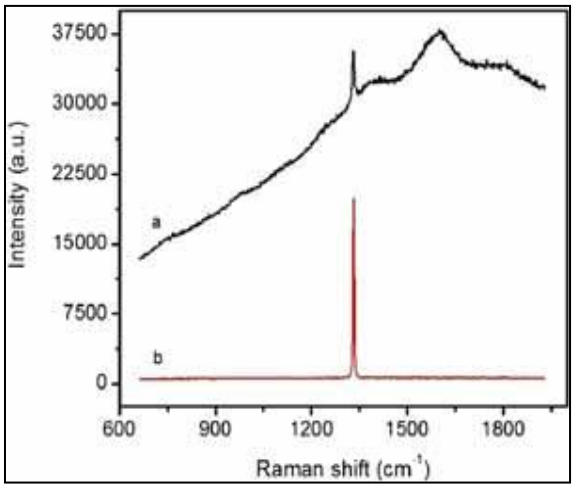

Figure 4.24. Raman shift of an irradiated diamond, (a) damaged region, (b) undamaged region

analysis of single crystal diamonds by Raman spectroscopy [57,58]. However there have been few reports on Raman spectra on radiation damage of single crystal diamond. Kalish et al. showed that for an ion implanted diamond there exist a critical damage threshold for the concentration of

damage produced vacancies above which diamonds get graphitized and below that level it can be restored through proper annealing [59]. This has been supported by Raman spectra analysis on regions selectively implanted. A carefully selected annealing range for samples implanted below the critical damage limit results to a gradual decay of the Raman peak at 1630 cm^{-1} , which is a Raman signal representing a specific vacancy.

In another report, Yang et al. looked at Raman spectra of a single crystal diamond irradiated with an 855 MeV electron beam over a $1mm^2$ area done over several years to reach a total fluence on the order of 10^{19}. The Raman spectra in the damaged diamond showed significant change with additional peaks appearing due to amorphous carbon, as shown in the figure 4.24. The Raman spectra indicates the such a dose produced substantial defects [60].

In this work, the Raman spectra at both heavily and lightly irradiated segments of the samples GYJ-148A and 148C were measured. A Renishaw inVia Raman microscope was used to conduct the study. The instrument has a visible (532 nm green laser) and a UV laser. For this study the samples were illuminated by the green laser. The power of the laser was adjusted to 1% to avoid any saturation in the ccd camera. The spot sized measured of the sample could be adjusted by using different objective lenses to get suitable laser illumination spot size. In our experiment the laser spot size was restricted to ~ 20 microns. In addition, a slit opening of 10 μm on the spectrometer was used, which can vary between 10-65 μm. For all the acquisitions a 10 sec. time frame were used. Additional application of the confocal lens in the optical path helps to reduce the beam divergence. As a first test of the measurement technique the electronic grade commercial sample-2and a HPHT sample is checked in the spectrometer. Both of the samples show the strong diamond characteristics peak at 1332 cm^{-1} as the only signal and hence ensures good quality as seen in figure 4.25.

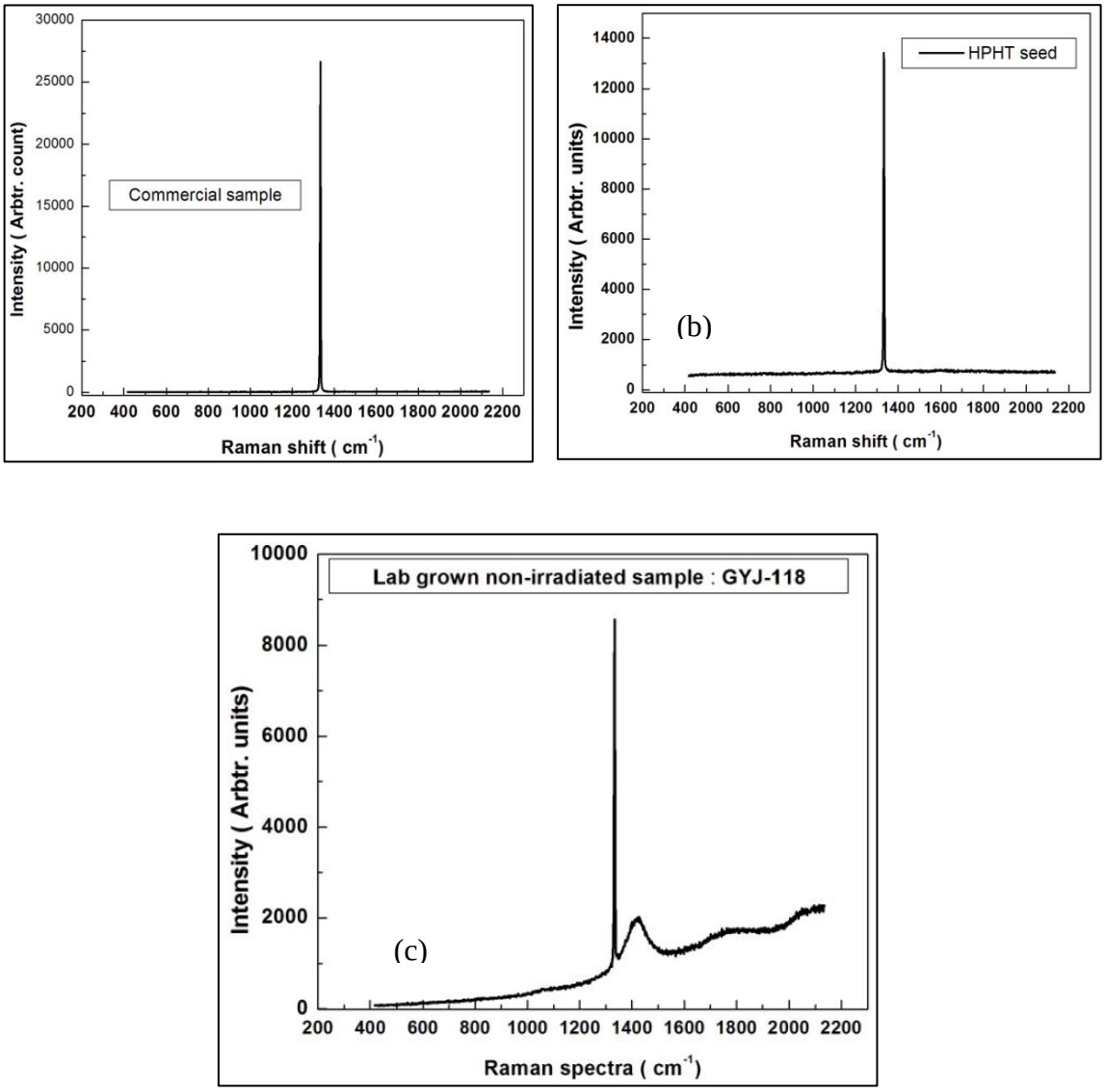

Figure 4.25. Raman spectrum collected from the instrument used for this work (a) electronic grade commercial diamond, (b) HPHT diamond and (c) a lab-grown non-irradiated diamond

However, the lab grown diamond shows some additional feature peak around 1430 cm^{-1}, which arises due to photoluminescence from nitrogen vacancies. There is also visible signal for the sample from 1500 cm^{-1} to 2150 cm^{-1} which is due to the presence of trace amounts of amorphous carbon in the substrate. Figures 4.26 show the Raman spectra of the irradiated samples.

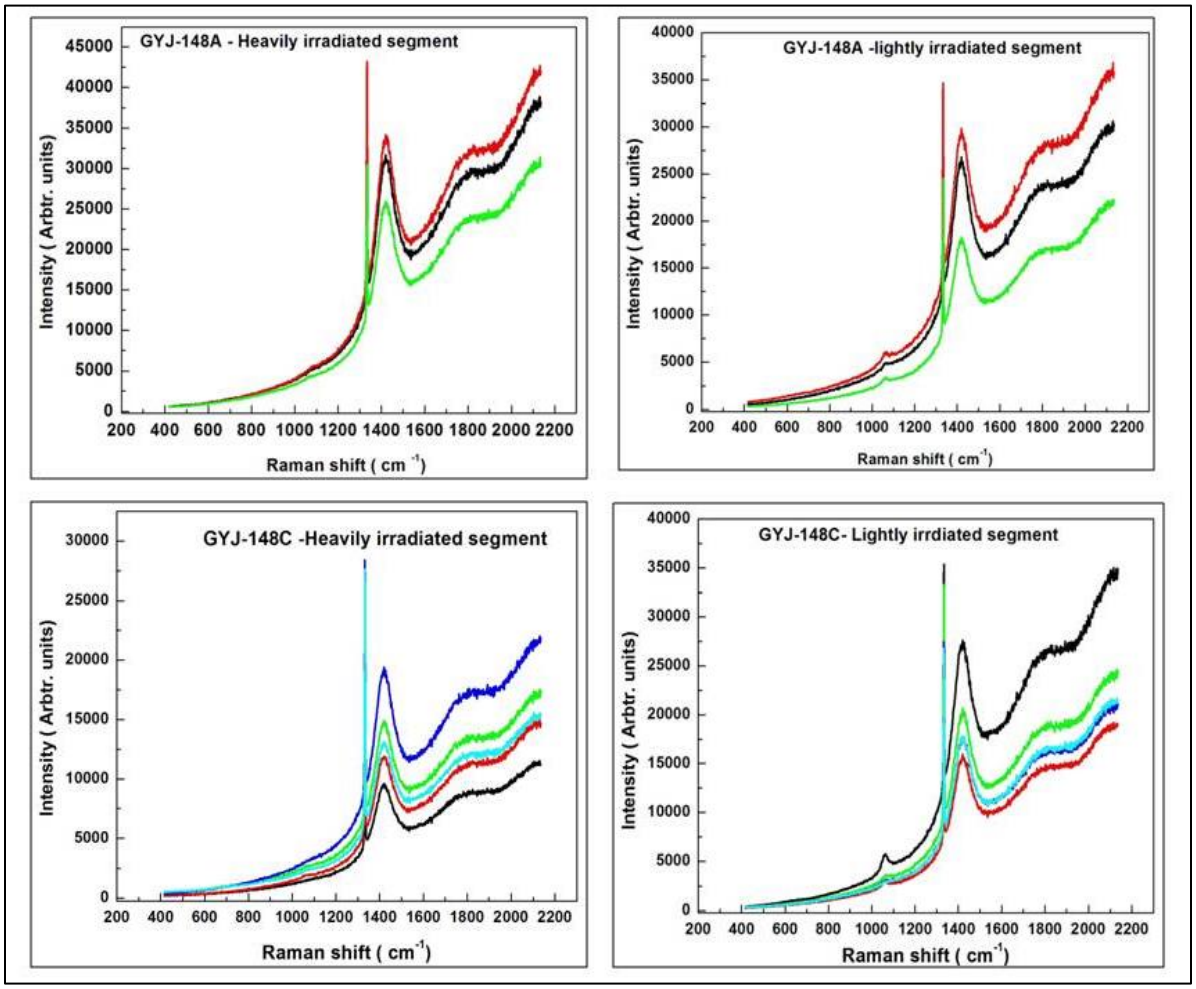

Figure 4.26. Raman spectrum collected from SHI irradiated diamonds

As figure 4.26 reveals with comparison to 4.25 (c) that all these labs grown diamonds have nitrogen produced photoluminescence signals. The different curves (represented in different colors) appear from different spots of the measurement conducted. This confirms that these samples have higher fluorescence as the background due to presence of higher concentration of nitrogen (compared to commercial samples). Also, since no additional peaks were observed in the heavily irradiated segment, it is indicated that the type and fluence of SHI beams used for irradiation did not produce enough damage to change the Raman spectra.

Chapter 5. Single crystal diamond deposition by chemical vapor deposition (CVD)

5.1. Brief overview of historical events

The basic idea of growing diamond in the laboratory lies fundamentally on the understanding that first diamond is solely comprised of carbon atoms and secondly that it requires intense pressure and temperature in the upper mantle of earth to form natural diamond. In the early sixteenth century Averani and Targioni [61] studied the combustion of diamond, but it was the significant work conducted by British Chemist Smithson Tennant in 1797 that proved for the first time the combustion of diamond produces CO_2 i.e. diamond is made of pure carbon. This idea opened a new series of attempts to convert diamond from the easily available carbon allotrope graphite. However, graphite is more stable at room temperature and pressure, which therefore made the idea very difficult to achieve. In the late eighteenth century out of many attempts some premature success stories were reported by J.B.Hannay in 1880, Henry Moissan in 1890 and later by Charles Parsons in the early nineteenth century, but some of the results could not be repeated and therefore left some doubts about the outcomes [62]. In 1939 O. I. Leipunsky from Soviet Academy of Sciences, Moscow was able to create a phase diagram to identify the right kind of temperature and pressure to convert graphite into diamond [63].

In 1941, P.W. Bridgman jointly with General Electric, Carbondum and Norton initiated a new venture to investigate diamond synthesis. Further in 1951, a new group was formed at General Electric with a focus on the role of high pressure in the diamond synthesis process. The group worked on modifying the design of Bridgman`s anvil to elevate the pressure to 10^6 psi. This was followed by some novel modifications by H. T. Hall to create a belt apparatus. Finally, in 1955 the

first success in the history of lab grown diamond was reported by H.P. Bundy, H. T. Hall and their group. This work initiated a new generation of diamond synthesis at high pressure and high temperature (HPHT). However due to government secrecy the details about the ultra-high pressure high temperature belt apparatus and the corresponding diamonds grown were not published until 1959 by H. P. Bovenkerk [64].

On the other hand, there was two competing projects between Union Carbide and General Electric going on around the same time to take a different diamond synthesis route, i.e. growing diamond at low pressure. After several years of attempts it was Union Carbide Scientist William G. Eversole who had the first success in the United States to produce diamond at low pressure on a hot diamond surface. Eversole`s study for this alternative approach started in 1949 by using CO as the source gas and subsequently moved to methane and other gases. The only documentation of his work can be found in a patent [65], [66]. However, at almost the same time Soviet scientist Boris Derjyagin and Borys Spitsyn applied for a patent in 1956 to claim the success of growing diamond in carbon using a gaseous environment [67], although the patent was not published until later in 1980. The work of Eversole was revisited and picked up with great interest by J. C. Angus of Case Western Reserve University, USA. He grew diamond on diamond seed crystals at sub-atmospheric pressure, which validated Eversole`s work [68]. Further around 1976 Deryagin`s group revealed the idea of growing diamond on non-diamond substrates. Nonetheless, all these early attempts suffered from very low growth rate, but their continued efforts led to the discovery of the critical role played by atomic hydrogen towards etching of graphite while promoting diamond growth.

In the early 1980s, a breakthrough was made in Japan. Matsumoto et al. at the National Institute for Research in Inorganic Materials (NIRIM) developed a hot filament reactor [69], which

unleashed an outpouring of worldwide interest in low pressure diamond growth. The major outcome of this process was its capability to grow diamond on non-diamond surfaces at almost 1μm/hr growth rate. This was followed by another landmark innovation in the deposition of diamond on non-diamond substrates but using a microwave plasma discharge. This work opened a new direction of diamond deposition which is still considered as one of the most efficient techniques. The Hot filament chemical vapor deposition (HFCVD) systems are quite regularly used in industry for large area deposition. Some details of these methods will be discussed in the next section.

5.2. Hot filament CVD

The hot filament chemical vapor deposition (HFCVD) technique was the first of its kind, i.e. a technique to grow diamond at low pressure [70]. Also this technique gained immense popularity for offering nucleation and growth of diamond on non-diamond substrates [71]. In this method, a gas mixture of hydrogen and small percentage (0.1~2%) of methane gas is flowed into a vacuum chamber to raise the pressure in a range of 1-100 Torr. The gas passes through a wire mesh or array made of W (most widely used), Ta, or Mo. The wire array/mesh is electrically heated to a temperature close to 2000 °C so the hydrogen gas molecules go through thermal dissociation and create atomic hydrogen. This atomic hydrogen further converts methane (CH_4) to methyl radicals (CH_3) and other hydrocarbon species. During the diamond deposition a Si or Mo substrate is placed a few mm to a cm below the mesh at some elevated temperature (700 °C ~ 1000 °C) to deposit the diamond. The typical growth rate in HFCVD systems can vary within 0.1-20 μm/hr. Lower growth rates typically produce higher quality films. Figure 5.1 shows a basic schematic of the HFCVD principle.

Although HFCVD is widely used to deposit polycrystalline diamond of reasonable quality, a limitation is the wire mesh acts as a source of contamination as well.

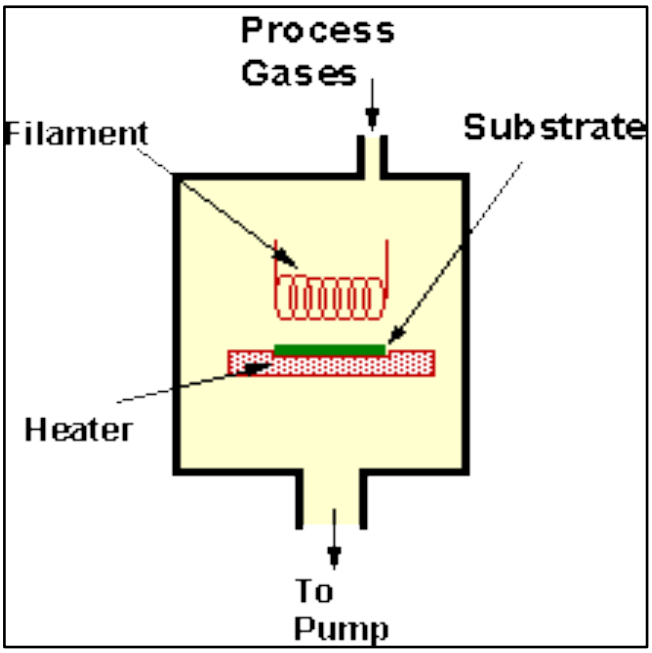

Figure 5.1. A schematic of HFCVD operation [72]

During the deposition process the wire mesh/filament, especially for tungsten wires, is carburized. This results to an additional incubation time at the start of the deposition. This causes slow and non-uniform growth rates during initial stages of growth. Also, at higher temperature the filaments can oxidize, and they occasionally break as well. Since the gas activation process is a thermal process there is a low density of ions in the gas phase, hence biasing the substrate doesn`t work very effectively.

5.3. Plasma Enhanced CVD (PECVD)

Another method of diamond deposition is energizing the gaseous environment with a plasma to create the deposition process species. This process is called plasma enhanced chemical vapor deposition (PECVD). This technique can overcome some of the drawbacks of HFCVD, especially in terms of contaminants. PECVD is a family of techniques of using a plasma created with different types of discharges such as DC-plasma, RF-plasma, microwave plasma, or electron cyclotron resonance microwave plasma. Other than DC plasma, in all other cases a plasma discharge is generated by applying a high frequency electric field. The gas is partially ionized and within a certain volume converts into a collection of electron, ions and neutral gas molecules, which is overall electrically neutral. The highly energized electrons further impact the hydrogen molecules to dissociate them into atomic hydrogens. The electrons temperature reaches over 10,000 K. However due to the neutral molecules the overall gas temperature stays lower. In low pressure plasmas, the electrons have a longer mean free path, fewer collisions with neutral molecules and therefore less energy transfer, so the overall neutral species temperature in the plasma is low. The exact opposite scenario happens at higher pressures and therefore the concentration of reactive species and overall temperature of the plasma is higher. The two important factors guiding the PECVD process are the initial chemical reactions in the non-equilibrium temperature plasma volume and the flux of species to the surface where diamond deposition occurs. A general schematic description of the PECVD process is shown in figure 5.2.

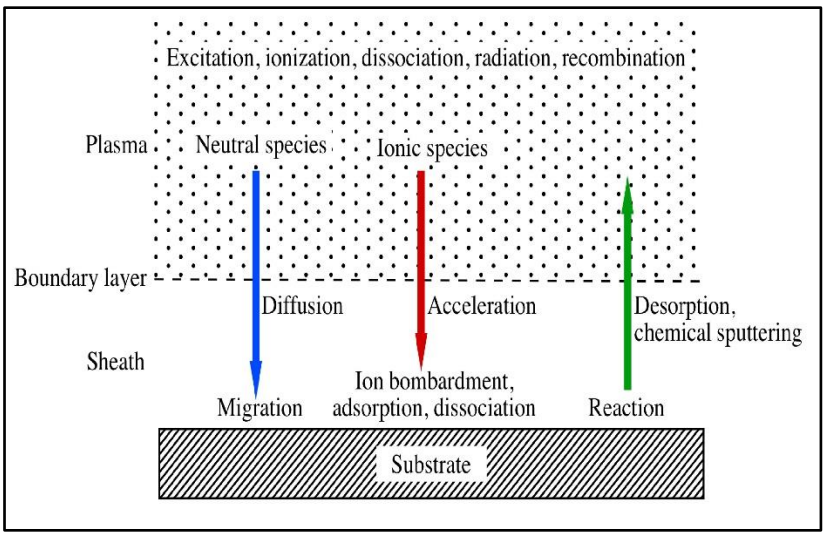

Figure 5.2. Reaction steps in PECVD process [73]

Within all the different types of CVD techniques, the microwave plasma assisted chemical vapor deposition (MPACVD) technique is an extensively adopted technique for high quality diamond deposition. Therefore, the MPACVD technique will be discussed in more detail in the following section.

5.4. Microwave Plasma-Assisted CVD (MPACVD).

The microwave plasma assisted CVD technique is currently the most applied method worldwide to grow high quality diamond. In the MPACVD technique, microwave power is coupled to the process gas volume through a dielectric window to excite the discharge. The process chamber is the fundamental part of the electromagnetic cavity, where only a particular mode of electromagnetic wave can oscillate. The mode is selected based upon the cavities' shape and dimensions. The microwave electric field heats up the electrons and the oscillating electrons transfer their energy to neutral gas molecules through subsequent collisions. The MPACVD process is very efficient from low pressure (10 mtorr) to very high pressure (~400 Torr). The

behavior of the discharge changes quite significantly with the variation of the pressure. As the pressure is increased in the process chamber, the plasma discharge shrinks in volume and creates a higher-power density regime of operation. At higher pressures, the discharge also becomes more spatially inhomogeneous (i.e. the core is at a higher temperature surrounded by a sharp transition to lower temperatures at the boundary of the plasma). The chemical reactions among the gas species start once the discharge has reached the required temperature, and the growth of diamond initiates when the right conditions are present on the substrate. Generally, the substrate is either penetrating the discharge or kept in very close proximity at the edge of the plasma. Some of the major advantages of MPACVD process is the stability and easy reproducibility of the microwave discharge, the high plasma density and low sheath potential, and the possibility of mixing different feed gases with less chance of contamination [10].

In the MPACVD process, the microwave power is generated from a magnetron operating at 2450 MHz (as it is more available) which is passed through a load matched waveguide. Another commonly used frequency is 915 MHz, which is used to deposit on larger substrates. A general configuration of a MPACVD is shown in the figure 5.3.

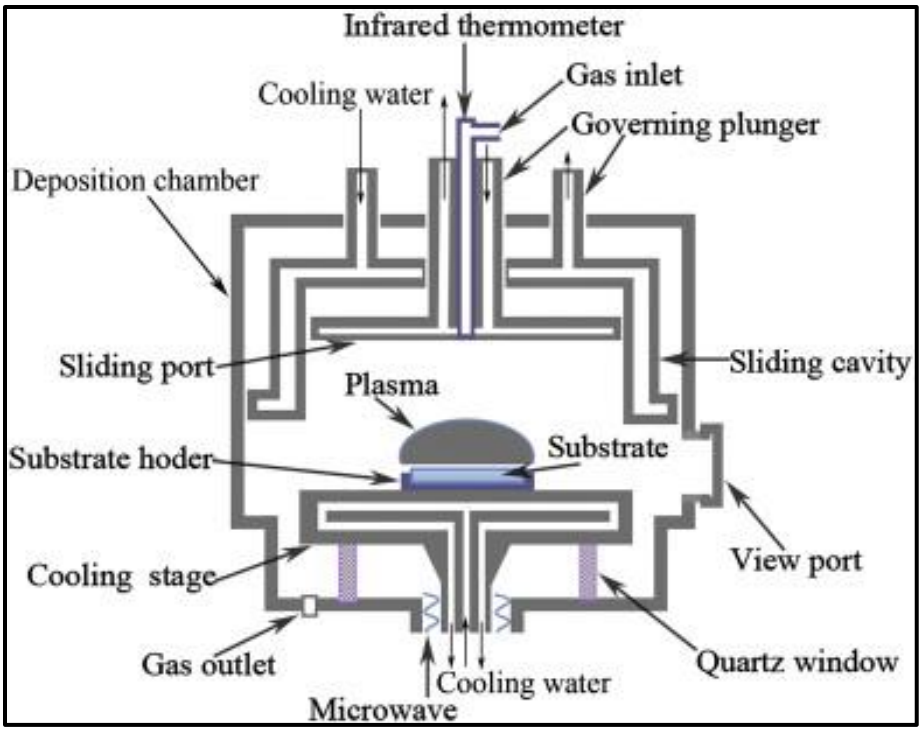

Figure 5.3. A cross sectional configuration of a MPACVD reactor [74]

Although a heater beneath the substrate is optional, at higher pressures a cooled stage is used to efficiently control the top surface temperature of the substrate on which the diamond is deposited. Controlling the deposition temperature is important for getting high quality diamond deposition. The power to ignite and maintain the plasma depends on absorbed power P_{abs} (where $P_{abs} = P_{source} - P_{reflected}$) where P_{source} is the microwave power from the power supply and $P_{reflected}$ is the microwave power reflected from the reactor.

The MPACVD process still draws lot of attention from both industry and academia in terms of different reactor designs [75], [76],[77],[78],[45] as well as optimization of the process to make efficient and faster growth of diamond.

5.5. Deposition of single crystal diamond

The nature of diamond growth in the CVD process is an ensemble of multiple complex chemical and physical process that deposit hydrocarbon species on the substrate [79],[80],[81]. Some of these complex reactions get altered based upon plasma growth conditions and substrate surface conditions. Before going into the actual details of the chemical process, a simplified view of diamond growth process is shown in figure 5.4. The process gases are fed to the deposition chamber of the reactor. The activation of the reactant gases takes place next by energy supplied from a microwave, RF or hot-filament source. This proceeds by the active radicals and molecules moving closer to the growth surface and finally chemical reactions on the surface that grow diamond [82],[8],[83].

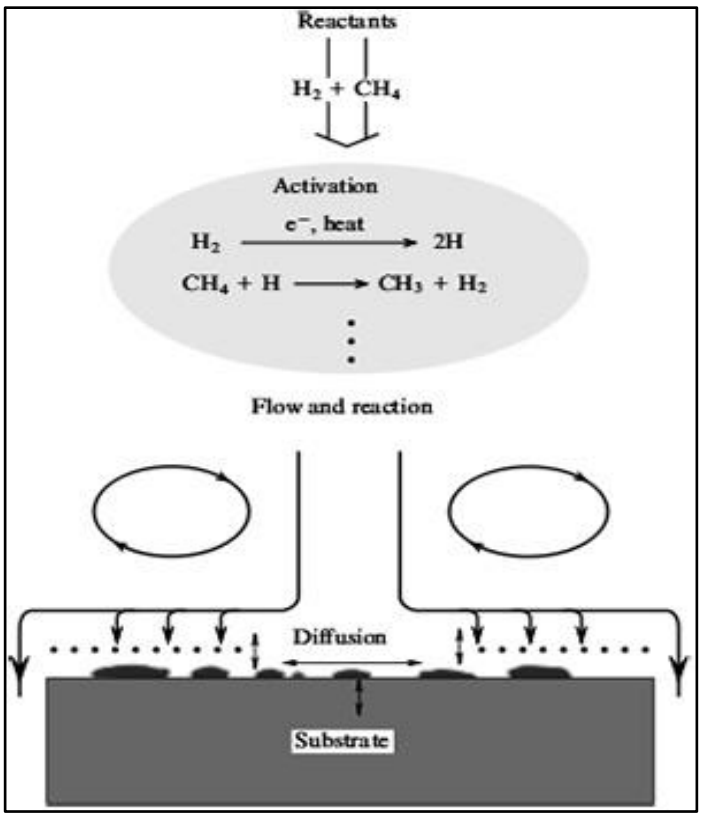

Figure 5.4. A schematic showing the process of diamond deposition during CVD process [20], [84]

The diamond deposition process by CVD technique is an example of turning gaseous reactants into a solid-state material. Therefore, the fundamental aspect of this process relies on the chemical reactions of the species at the surface, the orientation and morphology of the surface and the temperature of the surface. As already stated, atomic hydrogen plays the most crucial role for the diamond CVD process. The diamond growth conditions are preceded by the substrate surface being almost entirely saturated by hydrogen atoms. Otherwise dangling bonds created by surface abstraction or thermal desorption may lead to graphitization. Also, atomic hydrogen etches graphite faster, leaving sp^3 bonded carbon at the surface. Then a small percentage of carbon containing precursor gas is introduced in the chamber. Out of variety of choices, methane has become the most used carbon precursor gas over the years. Occasionally hydrogen atoms de-

absorb from the surface to recreate a dangling bond and forming H_2. Then, due to the presence of a hydrocarbon species (CH_4) in the plasma, at a small percentage the hydrogen abstraction sites methyl radicals (CH_3) can react with the open surface sites and carbon atoms get attached to the bonds. The combination of this process (hydrogen abstraction and methyl addition) continues to the next adjacent sites and diamond grows.

The chemical reactions for diamond growth rely on the relationship of external control parameters to the deposition CVD chemistry within the reactor operating region of diamond growth. A detailed framework of diamond growth based on the input gas compositions was proposed and further defined by Bachmann et al. [85] in 1994. Their initial work was built on the experimental condition of nearly seventy research works that used a variety of different CVD techniques. The processing input gas mixtures for diamond growth is plotted on a triangular plot with the carbon, hydrogen and oxygen (C-H-O) composition indicated on the diagram as shown in figure 5.5. One this diagram the region of diamond growth is indicated.

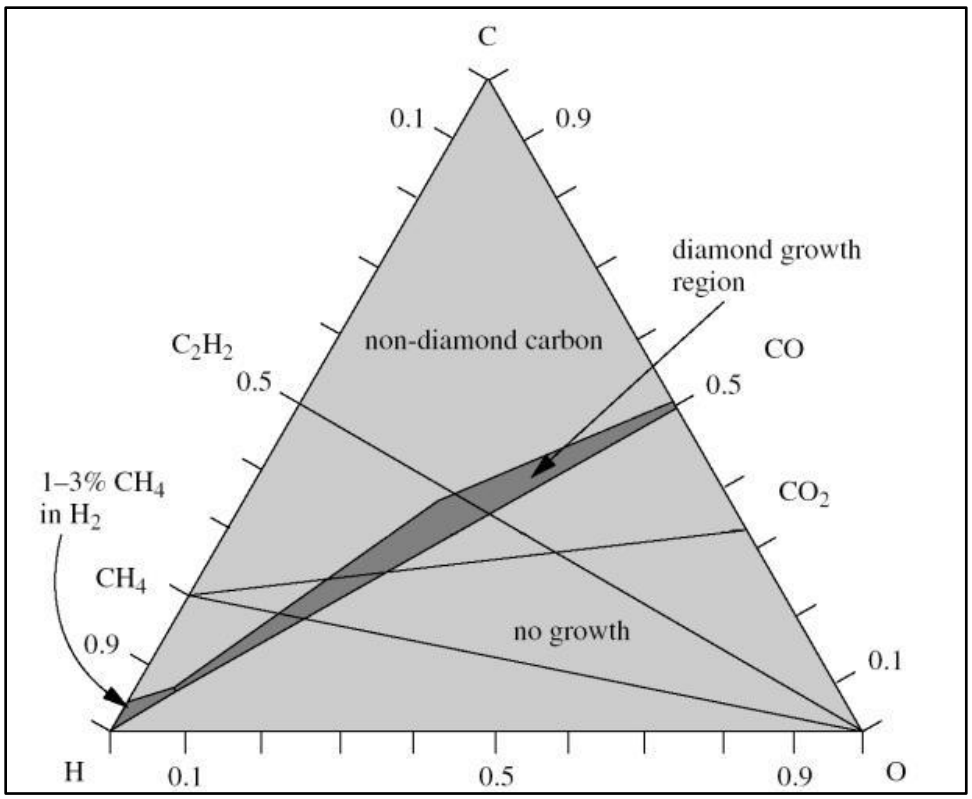

Figure 5.5. Bachman C-H-O triangle describing the gas composition required for diamond growth [11]

The important prediction from Bachmann was that, irrespective of the nature of growth, diamond will only get deposited when the gas composition is above the CO to hydrogen tie-line [11]. Outside this narrow triangle of diamond growth, the result either ends up into no growth (i.e. if gas composition moves towards the O vertex) or nondiamond carbon phase deposition if the carbon concentration is too large.

5.5.1. Chemical reactions for CVD diamond growth

The basic process of diamond deposition is primarily built upon two important sequences, i.e. (a) the creation of atomic hydrogen in the discharge and (b) the breaking the carbon containing gas species into carbon containing radicals. The chemistry of diamond deposition is a complex

process as it involves (i) competitive deposition processes between sp^2 and sp^3 structure growth and (ii) the possibility of other chemical reactions taking place due to presence of other carbon containing compounds. An early study of Frenklach and Wang [86], [87] covered some of these processes like the growth rates of sp^2 and sp^3 carbons, and their respective etching processes to have a better understanding of the diamond deposition process.

In a plasma assisted CVD system a simplified set of chemical reactions (a-k) can be formulated to describe the diamond deposition process. The electrons are energized in the plasma by the power coupled to system and the energetic electrons dissociate the molecular hydrogen into atomic hydrogen. At lower energy density, atomic hydrogen is produced through electron impact dissociation [88], [89]

$$H_2 + e^- \rightarrow H + H + e^- \quad \text{(a)}$$

This above process is balanced by diffusion of some hydrogen atoms to the wall or recombination of the atomic hydrogen in the gas phase. Although the recombination of hydrogen atoms in the gas phase is a slower process, especially at lower pressures. The recombination process can be written as;

$$H + H + M \rightarrow H_2 + M \quad \text{(b)}$$

which is a pressure dependent process, where a third body (M) is involved to carry away the excess heat.

In presence of any hydrocarbon species, a combination of reactions can also take place in the plasma discharge that use the atomic hydrogen. Some example reactions include reactions that convert stable molecules (such as CH_4) to reactive radicals (such as CH_3) and vice versa.

$$H + CH_4 \leftrightarrow CH_3 + H_2 \quad \text{(c)}$$

and

$$H + CH_3 + M \rightarrow CH_4 + M \quad \text{(d)}$$

This homogeneous recombination process (c) can be neglected at low pressures, but for higher pressures with a considerable amount of hydrocarbon the hydrogen atom distribution in the gas phase is affected. However, hydrogen atom loss primarily happens at reactor walls and at the diamond growth surface.

Diamond deposition requires the formation of active diamond growth sites on the growth surface where a sp^3 radical or other carbon containing radical addition to the surface can happen [23]. Under typical growth conditions, the number of carbon surface radicals per unit area ($\chi_{C_{d*}}$) depends upon the rate of abstraction of hydrogen from the surface

$$C_dH + H \overset{k_1}{\rightarrow} C_{d*} + H_2 \quad \text{(e)}$$

and the loss of surface carbon radical sites caused by atomic hydrogen adsorption on the surface,

$$C_{d*} + H \overset{k_2}{\rightarrow} C_dH \quad \text{(f)}$$

where C_dH and C_{d*} represent the diamond surface site bonded to hydrogen and carbon surface radical sites, respectively. The corresponding reactions that fill a carbon surface radical via the dissociation of hydrogen,

$$C_{d*} + H_2 \overset{k_{-1}}{\rightarrow} C_dH + H \quad \text{(g)}$$

is much slower in comparison with reaction (f). $\chi_{C_{d*}}$ also depends on other growth species;

$$C_{d*} + C_nH_m \overset{k_3}{\rightarrow} \text{products} \quad \text{(h)}$$

and decomposition of diamond structure on the surface to graphite (and it`s reverse reaction),

$$HC_d - C_{d*} \overset{k_4}{\rightarrow} C_{gr} = C_{gr} + H \quad \text{(i)}$$

and

$$C_{gr} = C_{gr} + H \overset{k_{-4}}{\rightarrow} HC_d - C_{d*} \quad \text{(j)}$$

where, C_{gr} denotes a sp^2 structure site.

At steady state conditions for the surface radicals,

$$\chi_{C_{d*}} = \frac{k_1[H]\chi_{C_dH} + k_{-4}[H]\chi_{C_{gr}}}{k_{-1}[H_2] + k_2[H] + K_3[C_nH_m] + k_4} \quad \text{(k)}$$

and at high atomic H concentrations, the terms $k_2[H]$ and $k_1[H]\chi_{C_dH}$ become the controlling factor of the surface density, hence,

$$\chi_{C_{d*}} = \frac{k_1}{k_2}\chi_{C_dH} \quad \text{(l)}$$

The overall surface site density is

$$\chi_{c(total)} = \chi_{C_dH} + \chi_{C_{d*}} + \chi_{C_{gr}} \quad \text{(m)}$$

which is observed in any standard CVD growth processes.

At low hydrogen atom concentrations, $k_{-1}[H_2]$ dominates the denominator however k_1 [H] has some effect which makes,

$$\chi_{\mathrm{c_{d*}}} = \frac{k_1[H]}{k_{-1}[H_2]}\chi_{C_dH} = K_1\chi_{C_dH} \quad \text{(n)}$$

where K_1 is the equilibrium constant. From the equation above (n), it is evident that diamond growth depends on the equilibrium condition of H atoms concentration over H_2 gas molecules concentration. Low concentration of H atoms slows down etching of non-diamond surface carbon sites and total number of diamond growth sites.

This is one of the key points of defect generation of diamond (although this is not the most comprehensive explanation for all kinds of defects that can occur during diamond growth). A generic idea of defect growth relies on the interaction of H atoms and sp^2 incorporation. The basic assumption in the generic model of defect growth is that an adsorbate reacts with another nearby adsorbate prior to forming the lattice [90], for example two methyl groups react and overgrow to a sp^2 defect. Therefore, at a fixed substrate temperature, the defect fraction in the film X_{def} follows an empirical model as,

$$X_{def}\ \alpha\ \frac{G}{[H]^n} \quad \text{(o)}$$

where G is the growth rate. The order n is determined experimentally. The growth rate G is proportional to $[CH_3]$ [H] and in partial equilibrium, CH_3 is approximately proportional to $[CH_4]$ $[H]/[H_2]$ which translates into,

$$\mathrm{X_{def}}\ \alpha\ \frac{[\mathrm{CH_4}]}{[\mathrm{H}]^2\ [\mathrm{H}]^{\mathrm{n-2}}} \quad \text{(p)}$$

In general, n=2 is selected and

$$X_{def}\ \alpha\ \frac{[CH_4]}{[H]^2} \qquad (q)$$

Hence, from a qualitative viewpoint, higher atomic hydrogen improves film quality (lower sp^2 defects formation) however it also needs a low concentration of carbon rich gas species in the growth process. Some defects with sp^3 characteristics also form if the kinetics of bond formation between adjacent carbons is slower than the additional layer of carbon deposition due to a high gas flux of carbon rich gas [91].

5.5.2. Microwave plasma assisted CVD reactor

The very early approaches of low pressure CVD processes (Spitsyn, Derjaguin, 1980, Eversole 1962, Angus 1968) [92], [93] had low growth rates of a few nanometers/hr and hence they could not be applied to any industrial level growth. The major hurdle was that the gas temperatures were very low (600°C ~1200°C). The breakthrough appeared when the gas phase temperature and substrate temperature could be separately controlled. This idea allowed the creation of higher atomic hydrogen concentrations in the gas phase as well as an increase in the carbon growth species that allowed growth rate increases. The formation of a hot zone in the gas phase with a hot filament by Matsumoto et al. [9] from NIRIM led to a substantial higher growth rate and this process became a popular one in industrial applications. In the next year, 1983, after the success of HFCVD process Kamo et al. from the same institute, reported a methane/hydrogen plasma discharge formed with a 2.45 GHz microwave source that successfully deposited diamond films [94]. Later their reactor design became popular as the NIRIM type reactor, which used a silica tube that is attached to a rectangular waveguide to ignite the plasma. The typical operating conditions for these reactors are 80-100 Torr with microwave power range of 100W to 1.5 kW.

In 1987, P. K. Bachmann in joint work with Applied Science and Technology (ASTeX), designed a new type of 2.45 GHz CVD reactor by using a bell jar (dome shaped) with an inner diameter of 10 cm. The microwave power is guided through an antenna to the wave guide which contains the bell jar. The plasma is generated at the center of the bell jar where the field is maximum in strength. The design also had a scope of moving the substrate holder based upon a thermally floating stage or with an option of externally heated stage. Typical operating condition used for this reactor are 40-70 Torr with 1 kW power.

In 1992, an improved design of the bell jar reactor was announced by AsTeX, further known as High Pressure Microwave Source (HPMS) reactor. It was upgraded with a higher power 5kW magnetron power supply to increase the growth rate. Also, another major change was the bell jar was replaced by a silica microwave window. This advanced system could operate at a wider range of pressure including 10-120 Torr. Later AsTeX designed a 915 MHz system to enlarge the deposition area up to 30 cm diameter. At present some newer AsTeX 2.45 GHz reactors with power capability of 8kW and capable of covering an area of 50 mm diameter [95] have been developed.

In 1998, Funer et al. developed a microwave cavity, ellipsoidal in shape with microwave power fed from the top [78] via an antenna. The major outcome of this design was that the concentration of the field just above the surface of the substrate could be maximized with a very stable discharge. Both 2.45 GHz and 915 MHz systems were configured using this design. The systems were operated in a pressure range of 30-150 Torr with 2-6 kW power for 2.45 GHz and 20-60 kW for 915 MHz and were able to deposit uniformly on wafers with 2-6-inch diameter.

From 1986-1995, Michigan State University developed the microwave cavity plasma reactor (MCPR) and it was licensed by Wavemat/Norton [96]. A 2.45 GHz microwave generator

transmits the microwave energy to the cylindrical cavity through a rectangular waveguide via a coaxial waveguide transition and finally ending at an excitation probe. The cavity consists of cylindrical metal walls and a movable short plate defining the effective length of the cavity. At the end of the cavity a quartz dome encloses the discharge, which is hemispherical in shape. Since the entire deposition work of this thesis is carried out on an MSU reactor, the parameters related to this reactor will be discussed with more detail. A general design configuration of the MSU MCPR reactor is shown in the figure 5.6.

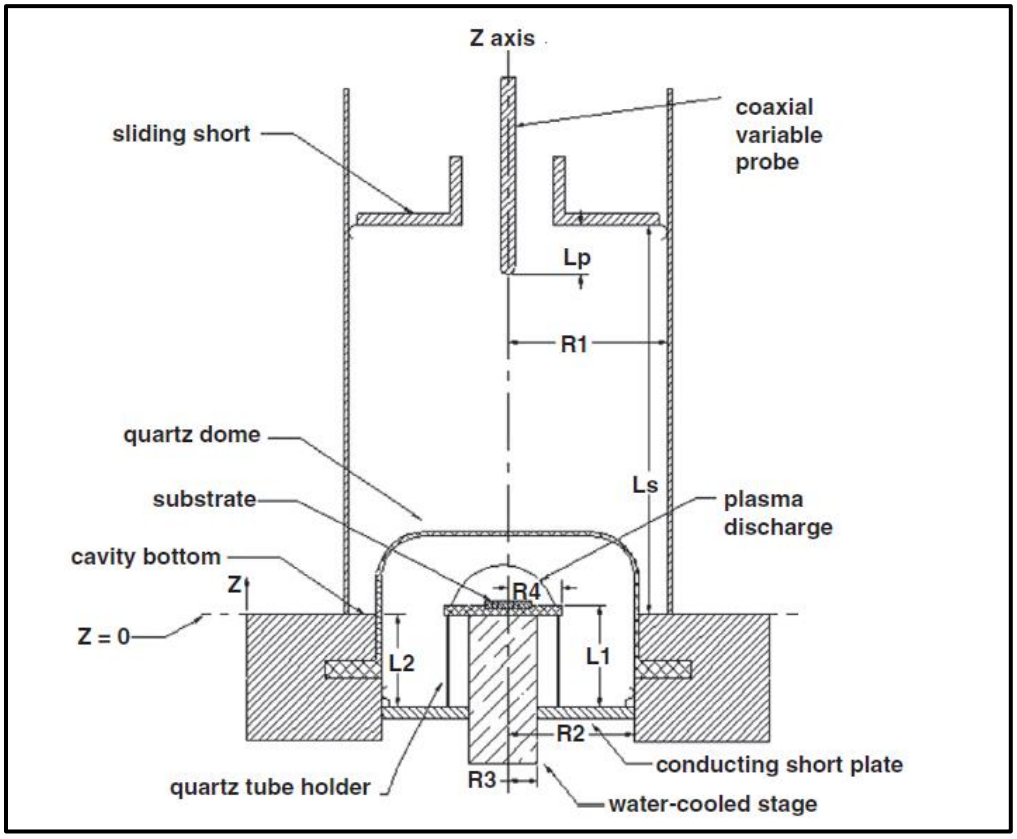

Figure 5.6. A cross-sectional view of a typical MSU designed reactor [97]

The physical parameters are defined as

Z=0: the plane that defines the boundary between cylindrical waveguide section (Z>0) and coaxial waveguide section (Z<0).

R1 & R2: cavity applicator radii, R3: Cooling stage radius, R4: substrate holder radius

Lp: probe length and Ls: short length

L1-L2: This defines the substrate position.

The substrate holder and cooling stage radii were modified at different stages of the reactor development and the design evolved to three different types of MCPR reactor. The initial design of the reactor evolved from a microwave plasma disk ion source in the 1980s and gradually through several years of work it was modified to MCPR reactor [96]. The first MCPR reactor design is designated as **Reactor A** and it has been used for polycrystalline deposition over the past two decades.[96] The major focus was to develop the experimental conditions to deposit polycrystalline diamond uniformly on Si substrate at pressures 80-140 Torr [38]. Later the operation was successfully scaled up to a deposition at 180 Torr over an area of 75 mm diameter [96].

However, to increase the growth rate and to move towards single crystal diamond deposition, reactor A (which was a generic design) was modified to operate at 180-260 Torr. The major changes happened to the diameter of the cooling stage (R3) and the diameter of the substrate holder (R4) with minor adjustments at the substrate height (i.e. adjusting L1 and L2). This new design allowed more concentrated plasma discharge (i.e. higher energy density) with higher growth rate but with a cost of shrinking coverage area. This new reactor design is named as **Reactor B.** This hybrid reactor`s (cylindrical for $z>0$ and coaxial waveguide for $z<0$) design allowed excitation of the TM_{013} and TEM_{001} modes simultaneously in the cylindrical and coaxial waveguide sections, as shown in the figure 5.7. Experimental work on PCD deposition and SCD deposition on this reactor B can be found in the thesis work of Kadek Hemawan, Jing Lu and Shreya Nad and associated publications [97–103].

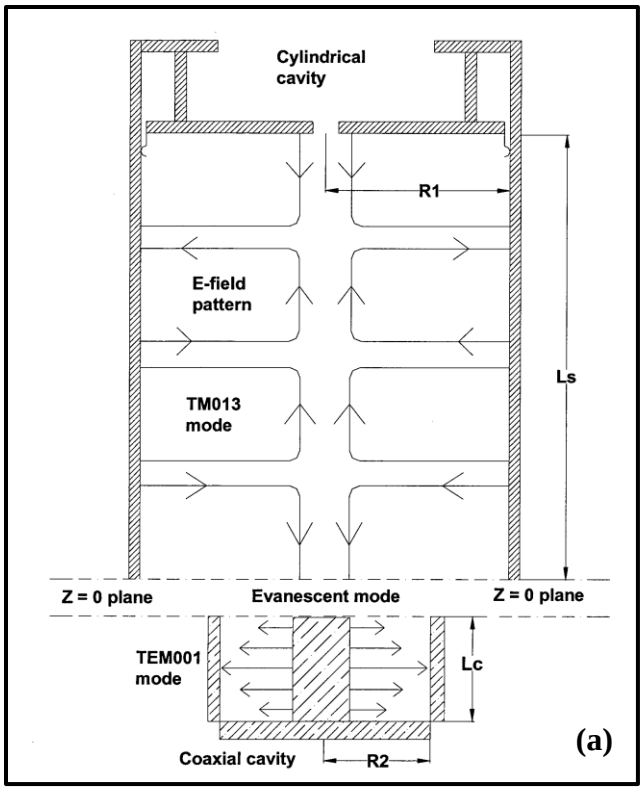

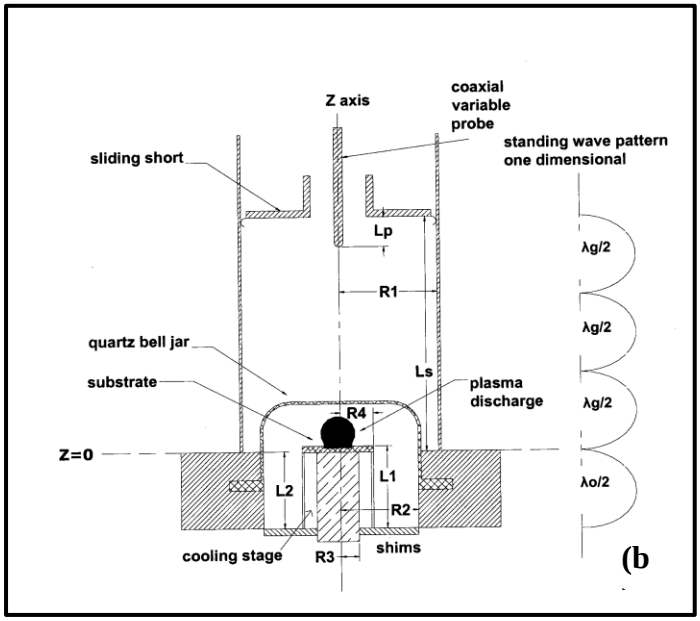

Figure 5.7. (a) Hybrid microwave cavity applicator (cross sectional view) with cylindrical and coaxial intersecting at z=0 plane (b) cross sectional view of standing wave pattern in Reactor B (smaller substrate holder) [104]

To visualize the field distribution inside the cavity it is helpful to have idea about the guided wavelength λ_g, which is the wavelength of the propagating wave inside the boundary of the cylindrical waveguide. Here λ_g is the could be defined as

$$\lambda_g = \frac{\lambda}{\sqrt{1 - \left(\frac{f_c}{f}\right)^2}} \qquad \text{(a)}$$

where f_c is the corresponding cutoff frequency of the TM (transverse magnetic) or the TE (transverse electric) modes in a cylindrical resonator, and $\lambda = c/f$, where c is the speed of light in free space and f is operating microwave frequency, i.e. f = 2.45 GHz here. In the cylindrical resonator a standing wave will be produced when the two ends are enclosed by conducting plates and separated by integer multiple of $\lambda_g/2$.

To further explore diamond growth in a higher-pressure regime, i.e. 220-300 Torr, a new design was established. The design evolved based on knowledge and operational experience of earlier reactors and it has been designated as **Reactor C** [105]. A detailed description of the background and developmental stages of this reactor can be found in the thesis work of Yajun Gu [106]. The generalized goal of this specific design was to develop an applicator which is a combination of different cylindrical coaxial and cylindrical waveguide sections. In addition, the adjustable probe and short plate capability were kept intact to have precise load matching control in order to minimize microwave power loss. The critical idea of the new cavity design is to properly guide the microwave power (i.e. to spatially focus, defocus and finally refocus) towards the substrate holder (z=0 plane) to get a more intense plasma. The radius of the cooling stage and the substrate holder remained unchanged in this reactor as compared to Reactor B. However, to compensate the power loss from the intense plasma being close to the quartz bell jar, the bell jar`s

diameter and height was increased from the earlier designs. A final prototype of the reactor design is shown in figure 5.8.

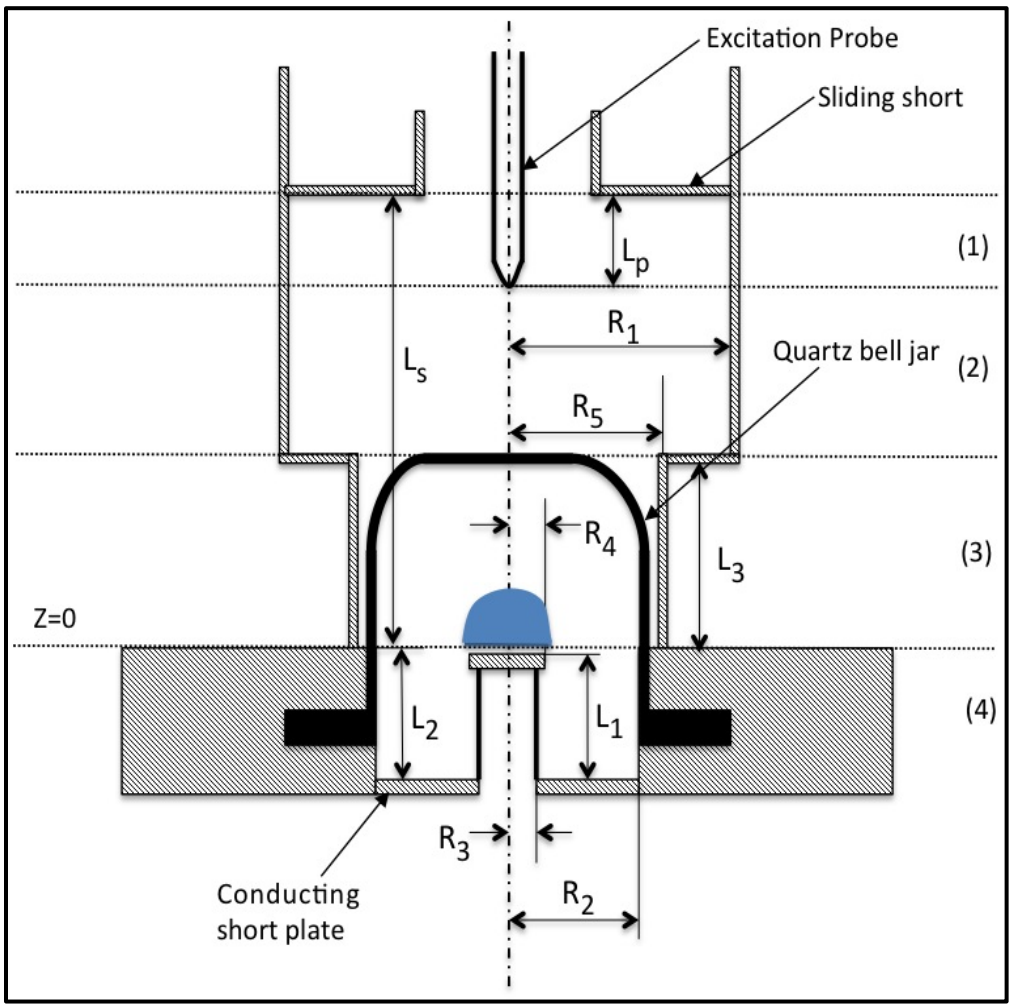

Figure 5.8. Cross section of generalized design of Reactor C [106]

A detailed description of the sections 1, 2, 3 and 4 shown on the right side of figure 5.8 can be found in reference [106]. In summary, this reactor excites different electromagnetic modes (as compared to reactors A and B) in different sections based on the dimensions selected for the design. Hence a new MCPR reactor became available from MSU that was capable of synthesizing single crystal diamond at a higher-pressure range. A summary of the different MCPR diamond deposition reactors is given in table 5.1.

Table 5.1. Differences in important design parameters between Reactor A, B and C (Adapted from reference [97]).

	Applicator dimensions (cm)		**Cooling stage dimensions (cm)**		**Substrate position (cm)**	**Quartz bell jar dimensions (cm)**		**Excitations modes**
	R1	**R2**	**R3**	**R4**	**Zs**	**Radius**	**Height**	
Reactor A	8.9	7.0	4.1	5.1	Fixed	13.0	9.5	TM_{013}
Reactor B	8.9	7.0	1.9	3.2	Variable	13.0	9.5	TM_{013} + TEM_{001}
Reactor C	15.2	10.2	1.9	3.2	Variable	21.6	10.9	TM_{01n}+ TEM_{001}

Operating Procedures of MPACVD reactor (Reactor B): This section will cover the detailed operation of the specific CVD reactor used to conduct the work in this thesis. This specific reactor is known as Diamond System 3 or DS-3 in the Fraunhofer-MSU center, which was established based on a MCPR reactor-B configuration and operated at a high pressure (240 Torr) regime. A brief coverage of the microwave cavity structure was already covered in the previous section. The other important necessary attachments to the cavity are; (a) microwave power supply and the power transmission waveguide, (b) the vacuum pump system and the pressure control system, (c) the gas flow mechanism, (d) the substrate holders and water flow system for necessary cooling and (e) a computer to run the automation program (LabVIEW) to control the entire deposition process. The following schematic in figure 5.9 shows a schematic of the entire CVD system for diamond growth, followed by a table (5.2.) showing all important attachments for the operation of the reactor.

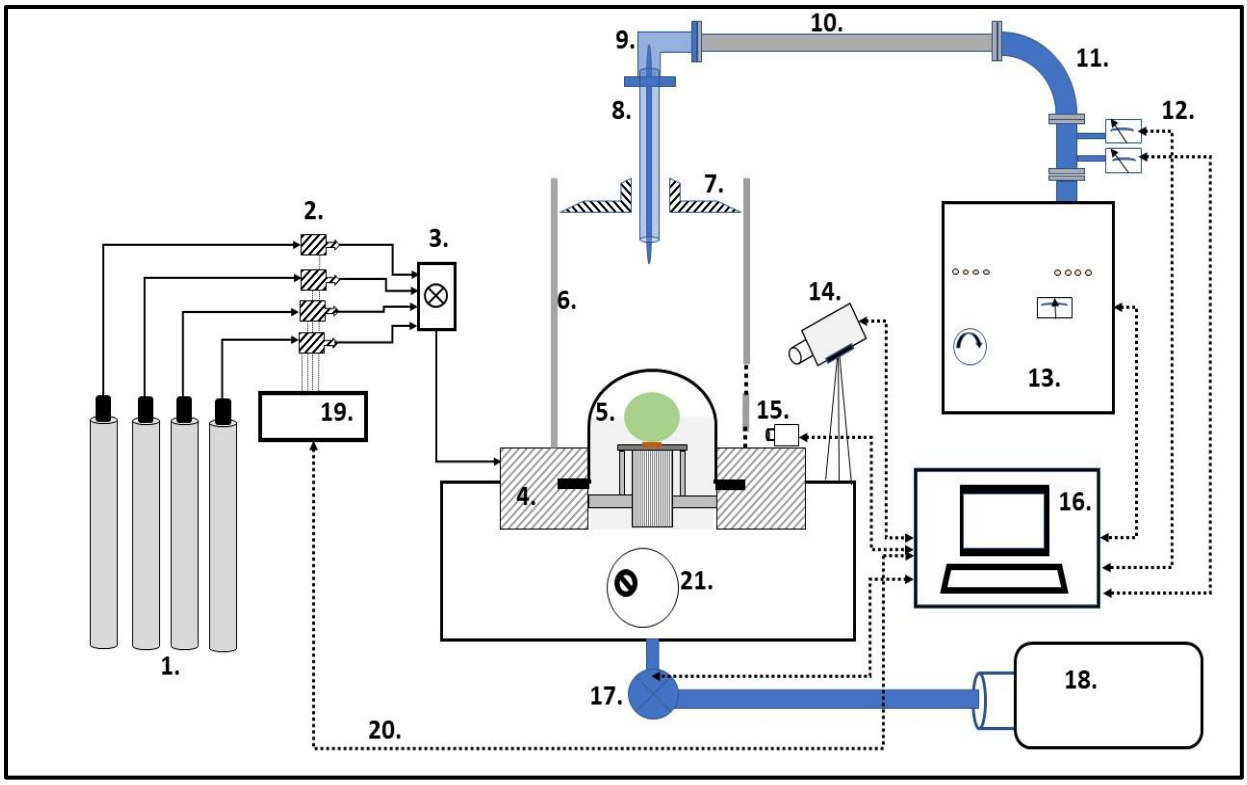

Figure 5.9. A schematic of the entire diamond deposition system based upon reactor B design

Table 5.2. Description of the different sections/attachments of reactor-B

1. Gas cylinders (Ar, H_2, CO_2 and CH_4).	7. Short plate.	13. 2.45 GHz, 6 kW Cober power supply.	19. Four channel Mass flow controller (MKS 247C)
2. Mass flow controllers for each gas cylinders.	8. Probe assembly.	14. One color pyrometer.	20. Dotted line represents all the communication cables from any instrument to computer.
3. Main gas needle valve to flow gas in the chamber.	9. Rectangular coaxial waveguide connector.	15. Sensor for dome temperature reading.	21. Vacuum chamber door.
4. Stainless steel baseplate.	10. Flexible waveguide.	16. Computer for running LabView.	
5. Quartz dome.	11. 90° bend wave guide	17. Baffle valve.	
6. Cylindrical microwave cavity.	12. 60 dB power meter.	18. Mechanical pump.	

(a) Microwave power supply & power transmission line subsystem: This section covers the functionalities of the microwave power supply and the process of microwave power transmission to ignite and maintain the discharge. A Cober power source (model S6F) is the 2.45 GHz microwave energy source. It has maximum power rating up to 6 kW. A circulator, a magnetron, a dummy load are the major parts of the microwave power supply which are enclosed inside the power supply cabinet. The circulator and the magnetron are continuously water cooled during its operation. The generated power is fed to the cavity through a series of wave guides, i.e. a S-band rigid rectangular waveguide, a bi-directional coupler (with 60 dB attenuation) which are also connected to two HP 8482H power sensors connected to HP 435 B power meters, a 90° bend waveguide, a flexible waveguide and finally an adapter to connect a coaxial waveguide. The two HP 435B power meters are used to measure the parameters; incident power (P_{inc}) and reflected

power (P_{refl}) which are used to determine the absorbed power in the reactor, as well as the power efficiency of the system and the power loss. Also, the reflected power is used to tune the reactor to operate it at maximized efficiency, which will be discussed in a later section.

(b) Vacuum and pressure control subsystem: The pressure inside the chamber is maintained with the combination of a vacuum pump and a throttle valve. The Alcatel 2010 SD pump is directly connected via a throttle valve and an oil trap. The chamber is normally evacuated for 8~12 hrs to reach a low pressure (3~5 mTorr). The pressure in the vacuum chamber is measured with two Baratron capacitance manometers (one measures 0.001 Torr to 10 Torr and another one from 10 Torr to 100 Torr) and they are read by an MKS-PDR-2C module. The operating pressure is maintained by the MKS-651 pressure controller, which remotely adjusts the throttle valve`s position to hold the set pressure (~ 240 Torr for most of the processes here) within ± 0.5 Torr of the set value. The pressure is created by allowing the feed gases H_2, CH_4, and O_2 to flow in the chamber at manually controlled flow rates and eventually computer-controlled rates, once the pressure reaches its set point. Generally, a leak check is conducted by closing the throttle valve and measuring the increase of pressure over a set amount of time. This is done to ensure no, or only very minimal external leaks exist. The DS-3 system is a tight system which has a leak rate of 30~40 mTorr/week. Another source of nitrogen getting into reactor when the chamber is center to atmosphere. Nitrogen gas is also used to dilute the hydrogen in the exhaust line from the pump to the external vent outside the building. This is done to minimize any chance of explosion.

(c) Gas flow subsystem: The gas flow in the system is controlled initially during a run by manual controlled flow and then finally computer-controlled flow by the MKS 627C (4 channel readout). The base pressure is monitored by the MKS 627B pressure controller which also adjusts the throttle valve position. During this study DS-3 had 4 gas cylinders attached to it, i.e. CH_4 (99.999% pure),

H_2 (research grade, 99.9995% pure), CO_2 and Ar gas. All four gas sources are connected through flexible metallic tubes to individual mass flow controllers (MFC) of different maximum flow ranges. Each MFCs are controlled by the MKS 627C which comes with 4 channels for read out. The CO_2 and Ar gases are generally used only for the quartz dome cleaning purpose or in some specific condition where the growth takes place with a little CO_2 added in the feed gas. H_2 gas is used both for the substrate etching (@ 180 Torr) or the growth process with 5% CH_4 added (@ 240 Torr). The output of the MFC`s meet at a common point which has a pin valve attached. The gases flow to the growth chamber through another flexible metallic tube only when the pin valve is opened. From the final gas tube, the feed gases enter the quartz dome through a single hole in the bottom steel plate and then flows through equally spaced small holes into the quartz bell jar through another supporting plate. The gas circulates inside the dome and flows out of the quartz dome through a base substrate holder with sixteen holes drilled close to its perimeter and next through a quartz tube of diameter ~ 60 mm, just seating on the cooling stage. The gas flow reaches the throttle valve and gets pumped out based upon the throttle valve`s position.

As earlier mentioned, the gas flow rate is controlled manually from the front panel of the MKS 247C to reach the target pressure through different stages. The pressure is put as a set value in the LabView program and the computer monitors the pressure. Once the pressure is reached, as read by the front panel of the MKS 627B as well as the MKS 627C are all turned to remote control mode so that the LabView can take full control of the operation for the entire growth time. Also, the program can shut down (turns off the microwave power supply) the process if there is a pressure fluctuation by more than 1 Torr. This is a safety procedure programmed for the operation along with some other safety procedures.

(d) The substrate holder and cooling subsystem: As the deposition process in the reactor takes place at high pressure and high-power density, the substrate holder and the diamond substrate itself gets very hot unless it is efficiently cooled. The reactor is connected with a Neslab CFT-300 water chiller. The circulated water is maintained at 18°C. From the main water flow line in the reactor, the line splits into two parts. One part goes to the base plate of the cavity. The other part goes to the sliding short plate through a flow meter (to ensure a standard flow rate for every operation). The water flow rate normally varies between 0.45 gal/min to 0.50 gal/min. As a matter of maintenance, if the water flow rate drops below 0.25 gal/min, then the whole water chiller and the flow lines are cleaned, and fresh distilled water is put into the tank. From the sliding short plate, the water flows into the cooled substrate holder stage (located inside the vacuum chamber) and then it returns to the water chiller. Hence the flow rate is also important to adjust the cooling stage temperature, which further controls the actual substrate temperature.

Apart from the substrate holder being water cooled, the inside of the microwave cavity is also cooled with an air blower. It blows in slightly above the quartz dome, where air flows through an inlet in the side of the microwave cavity so that the air swirls around the outside of the quartz dome and then flows out through the cavity windows with small drilled holes. There are two additional fans directed towards the outside walls of the cavity, one cools around the antenna probe and another flows air externally around the cavity.

Next, focusing on the cooling stage, figures 5.10 and 5.11 show the design of the cooling stage and the substrate holder configuration. The substrate holder seats on top of the cooling stage shown in figure 5.10. L1 and L2 decide the distance of the top of the substrate holder from Z=0 plane. The thickness of a shim that goes between the cooling stage base and the cavity base plate is used to adjust the substrate position, denoted by Zs (= L1-L2). The experiments for this work

were done using a shim with thickness 0.254 inches. The actual substrate holder that sits on the cooling stage is a combination of three molybdenum parts, a holder with 2.55 inches diameter, a supporting disc and the SCD recessed pocket holder (Fig. 5.11).

The entire cooling stage shown in figure 5.10, that the substrate holder sits on, is made of stainless steel. The inlet and the outlet line of water flow in the cooling stage have diameters of 0.375 inches. The conducting plate is used to act as a conduction path of the microwave field surface currents. It also defines the effective bottom cavity length to sustain the desired microwave mode. At the top of the cooling stage column there is a small indentation. This is to properly align the substrate holder on top of the cooling stage along the line of the probe. There are 8 holes drilled inside the circular conducting plate. The quartz tube that seats on this conducting plate holds the substrate holder and guides the gases to flow through the tube and finally to a lower chamber connected to the vacuum pump.

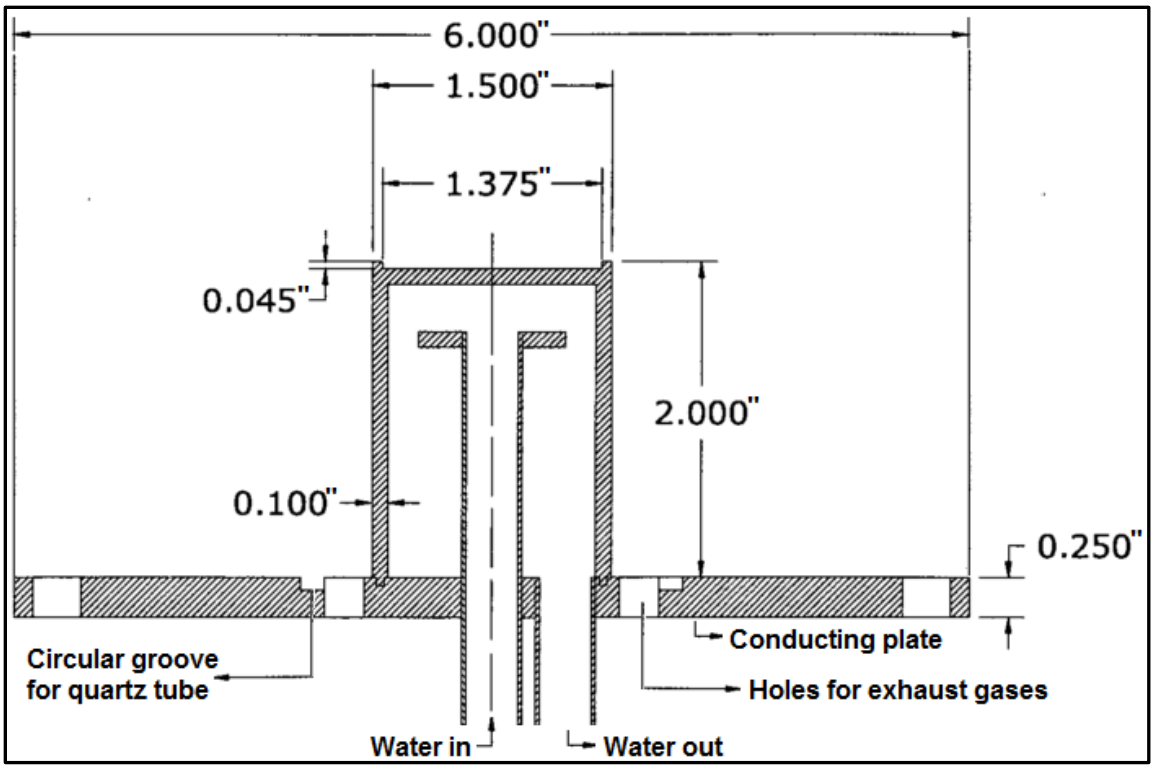

Figure 5.10. Design of the cooling stage for reactor B [107,108]

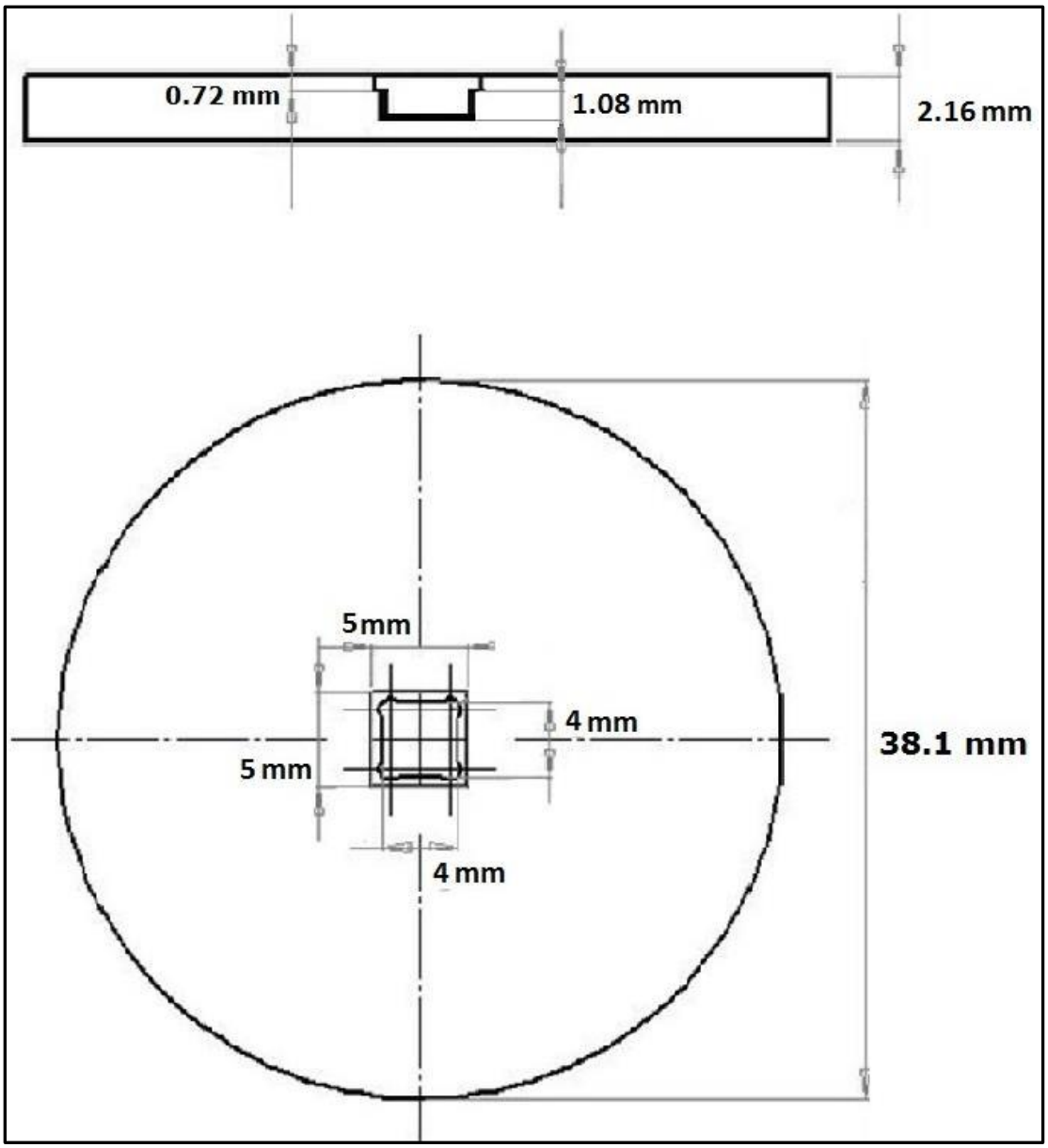

Figure 5.11. Dimensions of a 1.8 mm deep pocket holder [108]

(e) Computer control subsystem: LabView is installed on a computer to automate the whole deposition process. The program has access to the MKS 651 pressure control unit to monitor the pressure, the 4-channel read out to control the MFCs, a control to the microwave power supply to turn it on or off remotely, and access to the power meters to read (and store in a log file) the incident and the reflected powers. The reflected power is an important parameter, as its value is

the deciding factor for the tuning of the reactor. At the growth pressure, with the desired gas flow, microwave power, and standard probe length (Lp ~ 3.6 cm) set, the short plate position, i.e Ls, is adjusted to find the minimum reflected power position. This is also guided by the selection of L1 and L2. However, L1 and L2 cannot be continuously adjusted during the process. So, a selection of L1 and L2 needs to be done before the process initiates. With a fixed set of L1 and L2 selected, Lp and Ls are varied continuously to search for a point where the reflected power shows minimum value. For this work it is found that Ls ~ 21.5 cm allows a minimum reflected power point. More details about tuning process of the reactor could be found in reference [103]. Unless the process is not run with minimum reflected power it will add to more power loss. Also, if the reflected power is more than 25% of the incident power the computer control program is designed to shut off the process. There are many recipes developed through labView by former researchers in this group. The most commonly used processes are;

(a) a 180 Torr hydrogen plasma etch process

(b) a 240 Torr H_2/CH_4 gas discharge process for single crystal diamond deposition and

(c) a 60 Torr CO_2/Ar gas discharge process to clean the quartz dome.

As a standard sequence, processes (a) and (b) are always run in a sequential combination for a growth process. In process (a) the top surface of the diamond seed is etched to remove any polishing damage and any impurities on the surface. The process is run for 1.5 hr close to a temperature 1020°C ~ 1030°C with a pure hydrogen discharge. After completion of this process, the chamber is pumped down for at least an hour to get rid of all the residual gas in the chamber. The next process at 240 Torr is the one used for scd deposition. Any of these processes can be run for different times and at different pressures (these are the input parameters of the LabView program) unless other physical parameters of the reactors act as limitations. In process (b), multiple

steps are added in the LabView program and the user can add or remove steps with ease. In general, H_2 gas is flowed into the chamber to reach the growth pressure, and the power is also adjusted in steps to reach a temperature around 1050°C ~ 1060°C. Next the process continues at the stage for another 10 minutes for the temperature to settle down. Following this the methane is added in three stages. In stage-1, 1% methane is flowed for 3 min, then 2% methane for 3 min in stage-2, next, 3.5% methane for 3 min. in stage-3 and finally 5% methane for the rest of the process (either 2.5, 12 or 24 hrs.). All these parameters can be controlled from the LabView program. However, the power is gradually adjusted so that there are no abrupt power changes. This sequence for the addition of methane helps to avoid any sudden surge of methane and therefore any abrupt change in temperature. The growth process is conducted at 1080°C ~1100°C. Overall, this sequence allows the temperature to rise very gradually and with minimal adjustments in the source power control knob.

Substrate temperature measurement is done with an Arduino uno microcontroller programmed to record the temperature from the Ircon Pyrometer. The data is then fed to a raspberry-pi computer which continuously displays the substrate temperature and the dome temperature (with room temperature also as a reference). The raspberry-pi also collects pictures of the top surface of the diamond substrate from a camera and updates it every 5 minutes in the display screen. There is an additional camera that records live picture of the plasma through one of the viewing ports. Overall it generates a log file with all the variable parameters being updated every 5 minutes. The camera looking directly at the top surface of the substrate is attached to the view port of the infrared pyrometer. The operation of the pyrometer is fully controlled by the Arduino uno. There is another Arduino uno connected to the microwave power supply. This one is used to automatically ignite the plasma at 5 Torr pressures with 1 kW power. The uno adjusts

the position of a stepper motor which can move the power adjustment dial. For any further power adjustment, a rotary encoder is used to either jog or drop the power by moving the power adjustment dial through sending a signal from the uno.

Chapter 6. Single crystal diamond deposition on misoriented/offcut substrates

6.1. Overview of scd deposition on misoriented substrates

A major focus in the earlier section of this dissertation was on diamond detector`s performance. One aspect of this was addressing the performance of MSU lab grown diamond in comparison with the commercial electronic grade diamond. One of the major drawbacks of these MSU lab grown diamonds is their low charge collection distance (ccd) and therefore low charge collection efficiency (cce). As observed in section 3.2, in comparison to the commercial diamond plates (even after irradiation with heavy ion beams) the MSU lab grown diamond plates showed a narrower transient current response time at high electric fields. The lab grown diamond plates also had high birefringence i.e. higher strain in the samples. These problems mainly arise because the MSU diamond plates have higher nitrogen impurities (100 ppb~ few ppm), as nitrogen vacancies act as charge trapping centers. Also, the strain generated from the defects (threading dislocations) also severely affect the electronic properties (low breakdown voltages, high leakage current) [109]. Hence key factors towards growing plates for electronic/detector applications are (a) deposition of the SCD at very low nitrogen or controlled nitrogen environment and (b) controlled growth conditions to minimize defects on the grown layer.

While nitrogen is a detriment to the quality of diamond for electronic and detector applications, it has a critical influence on the growth of diamond. A small amount of nitrogen added in the gas phase helps to achieve growth with lower strain during deposition and it can enhance the growth rate [110], [111]. Watanabe et al. showed that an atomically flat epilayer of diamond with both low defects and impurities could be grown with a very low concentration of

methane (0.025%) in the feedgas to the plasma [112], [113]. However, to increase the growth rate from 50 nm/hr they used 0.15% to 0.5% methane which resulted in formation of uniepitaxial crystallites and pyramidal hillocks, as shown in figure 6.1. The defects formed during the early stages of diamond growth and for low methane levels (≤ 0.15%) the surface is smoother [114].

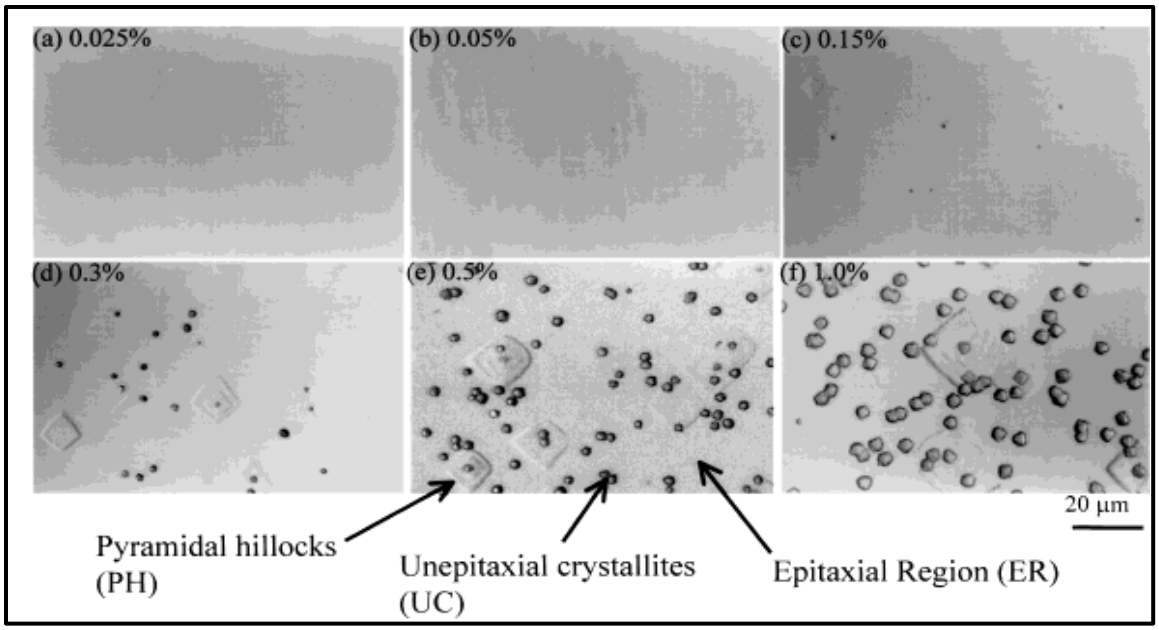

Figure 6.1. Appearance of defects on scd surfaces with very low percentage of CH_4 addition [114]

The authors claim that this ultra-low methane mix actually strikes a nice balance between etching of the surface defects as well as deposition of a high-quality layer. Further investigation in the defects shown that the defects were more localized at the unepitaxial defect regions. Similar non-epitaxial features and pyramidal hillocks were observed by Tsuno et al. [115] while growing a thick (~ 400 μm) layer. However, their growth condition had oxygen added in the feed gas. These non-epitaxial particles mostly formed due to small {111} facets forming on the {001} substrates during growth.

Bauer et al. [116] reported on growing high quality scd without any deliberate addition of nitrogen in the feed gas. In the process they added almost 10% of methane and raised the substrate temperature to 1200 °C to reach a growth rate of 30 μm/hr. The result was some of their initial growth on (001) oriented surfaces had non-epitaxial defects on the surface. Additionally, the edges of the grown samples had high PCD deposition, which blocked the lateral growth of the scd. The non-epitaxial particles laterally increased in size with longer duration of growth. Also, these structures grew at a higher rate compared to the epitaxial growth and hence they often extended further above the flat portion of the substrate into the deposition vapor allowing faster nucleation in their inclined surfaces compared to the nucleation on the non-tilted (flat) surface. Their conclusion was these particles may have been generated from impurities in the grown layer, rather than structural defects penetrating from the interface. Alternatively, the elevated growth temperature could create a growth condition which was non-favorable for the (001) growth.

Gaukroger et al. [117] studied X-ray topographs of CVD diamond grown on HPHT seeds to have a better explanation of clusters of dislocations that reach the surface and emanate from the seed-grown layer interface. They found that the majority of the dislocations have a direction near [100] line directions. Generally, such dislocations propagate along the growth direction as the process minimizes the lattice's total energy. Some defects can originate from polishing damage. These were observed as 45° mixed dislocations with a Burger`s vector parallel to polishing lines.

Overall X-ray topography is a powerful technique to understand the propagation of defects. It is also an effective method to understand growth of a sample at different stages during the growth process, however, topography requires a relatively thick layer for analysis. Microstructures of threading dislocations bundles were investigated using a combination of the etch pit method and cross sectional TEM by Tsubouchi et al. [118]. Cross sectional TEM allows better spatial

resolution as compared to X-ray topography. In the study by Tusbouchi the etch pits were guiding points for the locations where samples were carefully prepared for TEM analysis. The TEM micrographs showed the dislocation bundles were nearly parallel to film growth direction [001] and that they gradually diverged. In a different study from the same group [119], the authors focused on the evolution of threading dislocations during growth by performing an etch pit density analysis. High density dislocation bundles in the substrate generally act as the source of dislocation defects that propagate to the growth surface. These dislocation defect also show up during birefringence pattern measurement as a butterfly pattern. During growth, many of these dislocations propagate in the growth direction, however some of these show more lateral extensions. The importance of H_2 plasma etching and a detailed description of etch pit analysis could be found in the report by Ivanov et al.[120]. This technique is relatively less complex in comparison to X-ray topography or TEM analysis. Temperature and misorientation angle can strongly influence etching rate and etch-pit shapes. Figure 6.2 shows an AFM image of a typical etch pit shape created on a (100) plane, presented by Ivanov. et al. [120].

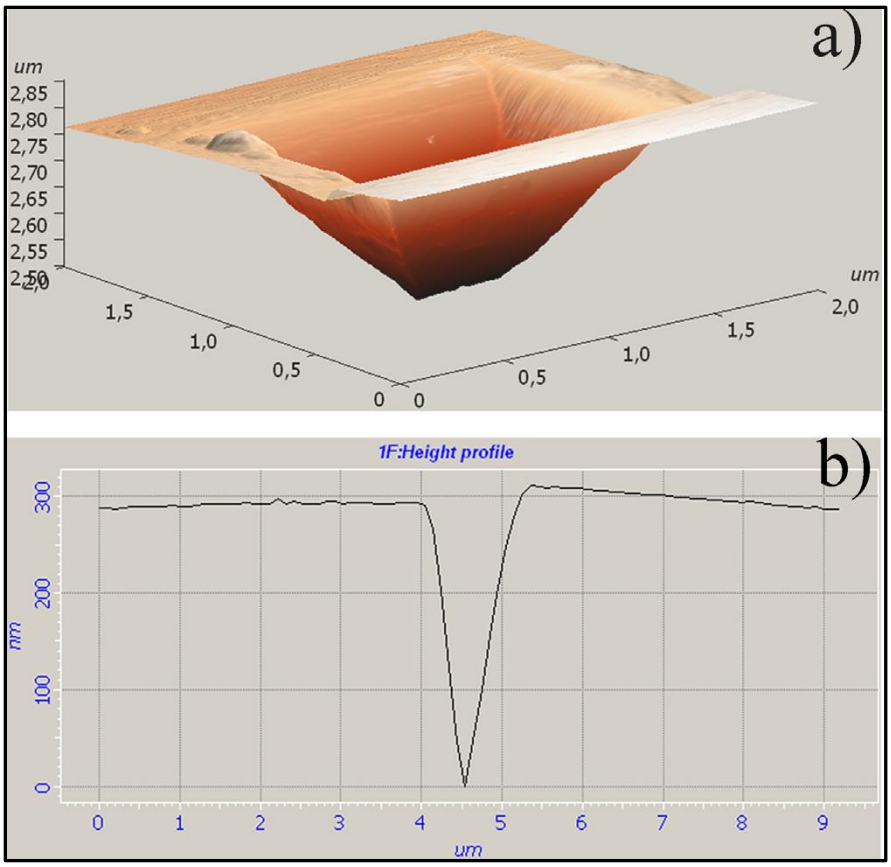

Figure 6.2. Appearance of an etch-pit, as viewed in AFM [120]

Tallaire et al. further explored the commonly appearing defects in CVD grown diamond layers by etching using a H_2/O_2 plasma (which can etch more effectively the defects) and then performing regrowth [121]. The three major types of defects that appeared during the process were unepitaxial crystals (UC), hillocks with flat top (FH) and the pyramidal hillocks (PH). A cross sectional TEM study by the authors of the grown layer revealed that UCs don`t have any direct root to the interface or the substrate, rather these defects nucleate on any contaminants (particles) that get into the layer during the growth process. The other two types, FHs and PHs are generate from extended crystallographic defects. The FHs and PHs contain (111) microfacets. If twinning occurs during the growth, then a twinned crystal will be formed on top of the hillock and steps will get generated from the twin and flow along the side facets. The authors also found that the short

H_2/O_2 etching method is a reliable and relatively easy technique to reveal dislocation defects and that it correlates with birefringence and cathode luminescence techniques. Further the etching technique also reveals shallow (both small and large) and deep (large) etch-pits. However, one has to estimate whether the etch pits or defects are fairly large as these shapes only relate to contaminants not the threading dislocations. The small square shaped etch pits (deep and shallow) could be correlated to mixed and edge dislocations propagating along <100> growth direction [122].

So, it is evident from the discussion above that the growth of electronic grade diamond with both low nitrogen content and low dislocation defect density poses a hurdle. The current state of art shows that most of the CVD grown diamond still comes with dislocation densities ~ $10^4/cm^2$ as well as nitrogen incorporation levels above a few ppb. Lowering these numbers requires a systematic approach starting with using higher purity feed gases, a tight control on the growth parameters, a proper maintenance of the reactor chamber, and proper quality control towards seed selection. However, none of these processes allows one to have a direct control over the defects especially during the initial nucleation stages. As mentioned earlier that an addition of nitrogen allows faster growth of diamond layers with fewer problems originating from the dislocation defects, but this is at the cost of poorer electronic properties due to the incorporated nitrogen. Hence a way is needed to serve both purposes, i.e. outgrowing CVD layers with low nitrogen without the formation of hillocks from the propagation of dislocations.

Takeuchi et al. proposed a roadmap explaining how misorientation angle and CH_4/H_2 ratio variation during PACVD could produce different textured surfaces over a small range of methane percentage (up to 2%) [123]. In their study the authors showed how to successfully grow atomically flat surface with a very minimal methane flow (~0.025%). However, to achieve a higher

growth rate they increased the methane (up to 0.5%) while keeping the other growth condition the same, but this ended up having more defects (UC, FHs and PHs) on the surface. The study results revealed that for low percentage methane flow (0.15~0.5%), UCs and PHs defects appear for low misorientation angles (<1.5°) of the top growth surface relative to the (001) crystallographic plane. They also found that with an increase in the misorientation angle, i.e. 2~3°, and by adding slightly more methane (up to1%), the growth occurred with more macro bunching steps but the surface was free of hillock features.

Tsuno et al. studied homoepitaxial film growth on misoriented substrates, especially the dependence of the surface texture and growth rate on off-cut angle. The influence of off-angle on growth rate was more evident at low methane concentration (~1%) than compared to higher methane concentration (~6%). Also, the growth rate variation was very minimal at low temperature (800°C) but showed an increase with low to high off-angle for deposition at higher temperature (1000°C) with 1% methane. On the other hand, a growth at 6% methane at lower temperature didn`t show much difference. The authors also achieved a smoother surface (hillock free) growth for a low offcut angle with growth conditions of a low methane concentration and higher deposition temperature.

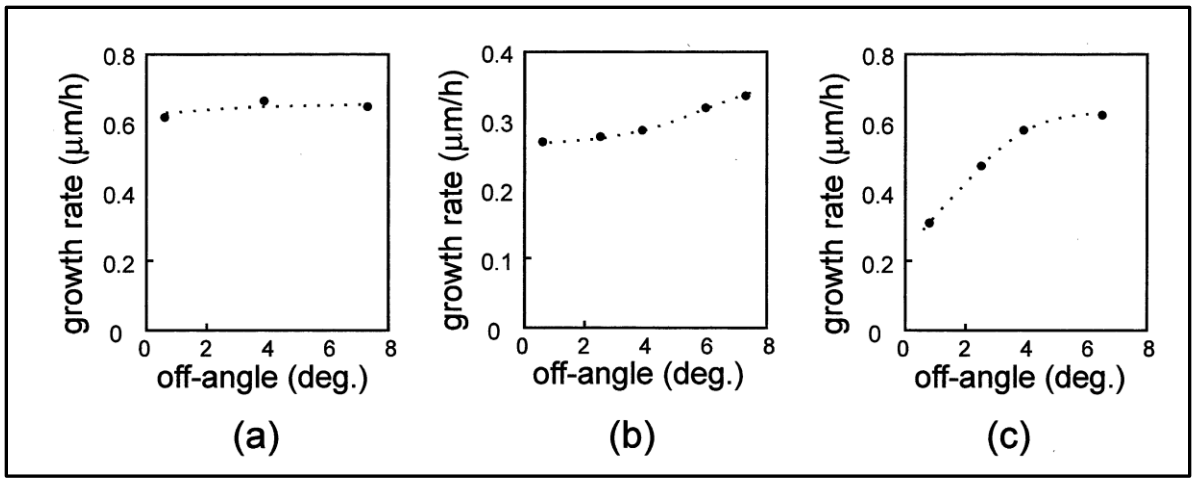

Figure 6.3. Growth rate vs misorientation angle toward [110] at (a) 6% CH_4 and 800°C, (b) 1% CH_4 and 800°C, and (c) 1% CH_4 and 1000°C as reported in reference [124]

As a key observation reported by the authors, at the low methane percent condition shown in figure 6.3 (c), a strong influence of the misorientation has been found. However, the influence is also dependent on temperature as shown in figure 6.3 (b) and (c). A lower temperature and the same methane percentage as in 6.3 (c) showed that the effect of misorientation is nominal. Finally, in figure 6.3 (a) the effect of misorientation angle remains very minimal even with higher methane flow (6%). A possible explanation by the authors for the observation in figure 6.3 (c) is that there might be two-dimensional nucleation rate that is smaller compared to dimer formation at low methane percentage, which changes with the misorientation. The surface migration eventually saturates at higher angles at this growth condition.

Lee and Badzian [125] looked into surface morphologies by varying the methane concentration from 1%, 2% and 6%. In deposition on misoriented samples (~ 15°) the authors found that the 2% film produced lowest surface roughness but had some pyramidal as well as flat head defects as seen in figure 6.4.

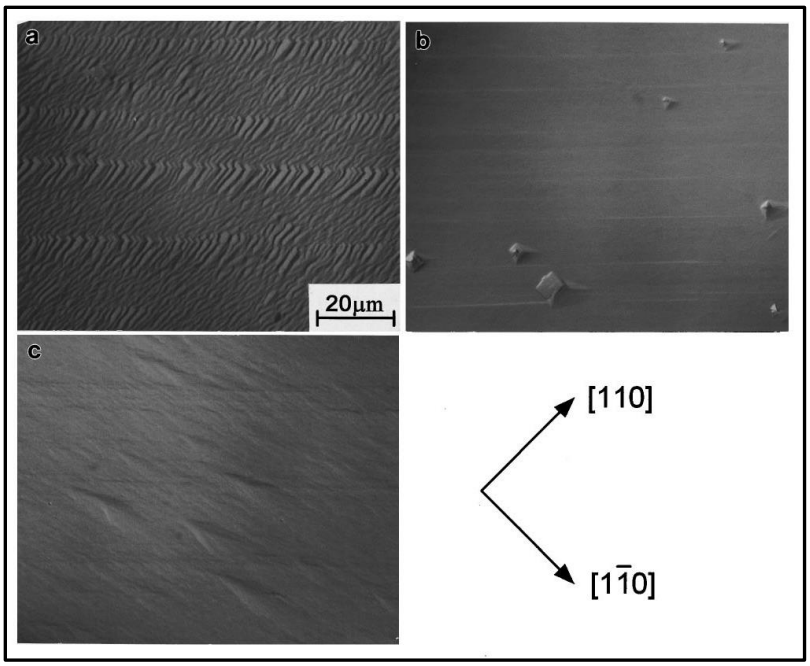

Figure 6.4. DICM images of the surface morphologies of (001) homoepitaxial diamond films grown for 5hr at 875°C with CH_4 concentrations of (a) 1%, ,(b) 2%, and (c) 6% in H_2.[125]

An increase in methane to 6% overgrew these defects but ended up in more random features with a general flow along the misorientation direction. The growth with 1% methane showed step flow growth as adsorbates mainly diffuse into steps since the diffusion length of adsorbates are longer than terrace width. A 2% methane adsorbates start to form stable clusters. With further increase in methane to 6%, the adsorbates have a much lower diffusion length and therefore random growth morphologies cover the entire surface.

Van Enckevort et al. performed a detailed study of diamond films deposited at misorientation angles relative to the [001] plane for diamond deposited by hot filament assisted CVD [126]. The authors concluded that homoepitaxial growth on [001] face is mostly guided by nucleation and propagation of <110> steps. However, in the process of (1) the nucleation happening on dislocation defect sites, or (2) non-epitaxial particles being on the surface, the deposition cannot give rise to large hillocks.

Theije et al. [127] studied the effect of nitrogen on step bunching for misoriented substrates (1.5° and 7°) directed towards [110]. The authors successfully verified their experimental observation by a simulation to reach a good agreement between experiment and simulation. According to their report, nitrogen`s presence causes a growth rate increase as well as step bunching. The step propagation on the surface becomes slower due to the nitrogen present on surface, however the sub-surface nitrogen enhances the growth by activating surface reconstruction bonds with N-donor electrons.

It was already discussed in reference [51] earlier about the hillock structures observed by Bauer et al. in their growth process on nominally [001] surfaces. In the same article, the authors further discussed on how growth on misoriented substrates (up to 8°) worked as a better solution in achieving a defect free surface. A surface with a certain inclination angle from the crystalline normal plane can act as a source of new crystal lattice planes. In presence of vicinal planes, the lateral spread of the planes can help towards overgrowth on top the defects and provide a higher quality layer. The quality of the layers grown on misoriented substrates were further confirmed by narrow full width half max value derived from rocking curve measurement.

In more recent work, Tallaire et al. extended their study on etching of misoriented substrate by using a H_2/O_2 plasma to understand new surface features. They created seeds with high offcut angles from the (100) plane (up to 20° offcut). The etching of diamond with a H_2/O_2 plasma forms clear etch pits (generally square in shape) when the surface being etched is close to the (100) crystal plane, however the etch pit shape changes and recognizable etch pits becomes challenging for the misoriented surfaces. As the etch rate on the misoriented surfaces are strongly influenced by the angle of miscut, the steady condition to create a regular etch pit shape cannot be attained. Instead, the etch process becomes highly directional and etches more along the [110] direction

which eventually appears as a series of “fish scale” like structures. But, on an interesting note the authors found that for samples with high misorientation along the <110> direction the etch process produces surfaces with low surface roughness. Based upon their observation of the etching of misoriented substrates, Tallaire et al. further continued to grow thick SCD layers on different misoriented samples, where the angle of misorientation varied from 3.5° to 20° from both [100]. and [110] and a thick layer of at least 500 μm were deposited. As an interesting outcome, none of the final grown layers had any impression carried from the misoriented substrate, which had different surface features due to etching. All the grown layers appeared smooth and defect free under the microscope, however the minimum thickness of growth to achieve a nearly flat surface varied largely with the misorientation angle (larger the misorientation the longer it is required to grow a flat surface). The thickness of the flat layer which directly correlates with the misorientation angle was further studied through a 3D modelling to idealize the growth parameters α, β and γ for different misorientation along [110] and [100] at different stages of growth. A detailed geometric modeling on the different growth shapes of CVD grown diamond in terms of growth rate of the main planes, [100], [110], [111] and [113] can be found in the report published by Silva et al. [128]. The model can be applied to growth of any crystal orientation to maximize deposition area. However, the model doesn`t address any defect growth that can deviate the process. The etch pit density of the CVD layers grown on the misoriented substrates by Tallaire et al. was quite high (10^6 ~ 10^7/cm^2) as compared to generally reported value for CVD layers (~10^4/cm^2). Also, the comparison between etch pits on along [110] and [100] misoriented study was not fully conclusive. Therefore, even though etch pits can reveal a defect rich zone of a CVD diamond layer and it can be correlated with higher birefringence layers grown on misoriented substrates.

6.2. Aim of current study

Deposition of single crystal diamond on the (100) surface is a complex process at low nitrogen environment as in most cases the surface gets covered with defects arising from dislocations and twinning present in the substrate. All these defects partially or fully slow down any lateral step flow growth on the surface. Hence the primary solution to tackle this problem is to grow single crystal diamond on misoriented substrates. A misoriented substrate with offcut direction along the <001> or <110> directions offers adsorbates steps to be absorbed at so that a lateral flow growth occurs. Hence the higher lateral growth rate ensures that the lateral step flow grows over the defects (hillocks, flat tops) and eventually ends up as a defect free surface. Although these surfaces will have different surface structures (step-terrace distribution, step bunching) unless grown quite thick (500 μm or more).

It is also found in literature that on a surface with steps and terraces that impurities generally incorporate more into steps than the terraces. This may affect the electronic properties of the grown layer. So, the main focus of this section of study is to understand the distribution (the mean values of step heights and terrace width) of step heights and terrace width with respect to different misorientation angles (2.5°, 5° and 10°) along <001> and <110> directions. According to the literature, this is expected to generate a wide range of step and terrace distributions with respect to the angle while keeping the other growth parameters fixed. These distributions or rather surfaces are very important to decide what kind of growth condition and misorientation angle one needs to pick up to achieve a dopant distribution for any specific device fabrication. This study only covers the effect of misorientation angle on step height and terrace width distributions, which otherwise could also get modified with methane percentage and temperature.

6.3. Experimental procedure

6.3.1. SCD deposition process

The single crystal diamond depositions performed in this study were conducted in a 2.45 GHz microwave cavity plasma reactor (MCPR). HPHT 1b type single crystal diamond substrates from Sumitomo Carbides were used for all the depositions. Initially all the substrates had dimension of 3.5×3.5×1.4 mm, with both sides polished. The substrates were checked with X-ray diffraction to ensure that their initial miscut angle from the (100) crystallographic place was below 1°. The samples were next cut and polished to the desired offcut shape as shown in figure 6.5. For bevel shape only, the top surface was cut (either along the [100] or the [110] direction) and polished to the desired angle. For the parallel substrate structure two sides were cut and polished. The final orientation of the crystallographic planes was verified again with a XRD measurement to ensure the desire offcut stays within ± 1°. The XRD measurements were carried out on a Bruker-AXS D8 instrument. The schematics of the different offcut substrates are shown in figure 6.5 with a desired orientation of the offcut angle plane. For offcut directions along [110] only a half of the surface was tilted as otherwise it is difficult to cut and polish the entire top surface along the diagonal. After the proper laser cut of the surface, the surface was polished to get an average surface roughness of 3 nm or less.

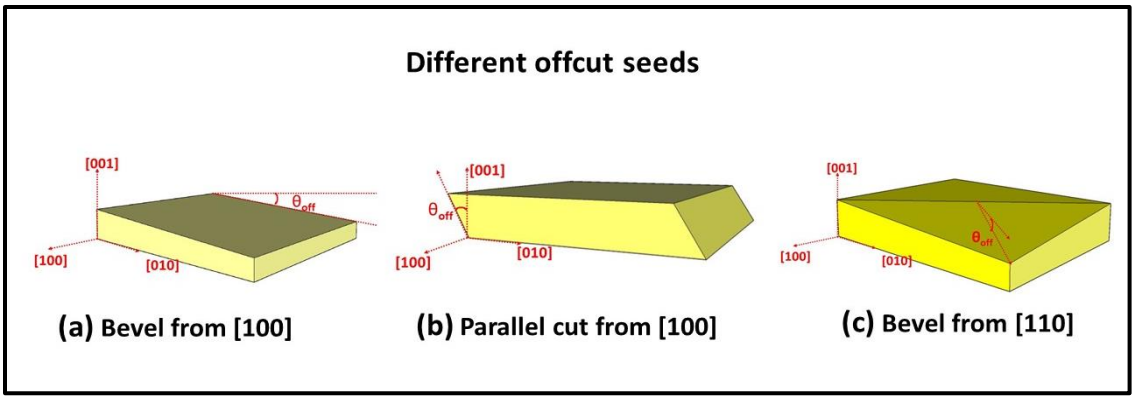

Figure 6.5. Orientations of offcut substrates along different directions from the (100) plane

The samples were next cleaned in boiling sulfuric and nitric acid mixture (1:1) for 20 minutes, hydrochloric acid for 20 minutes, followed by ultrasonication in acetone and methanol for 20 minutes each to remove any impurities from the surface. Next, the prepared samples were loaded in a pocket recess of a molybdenum substrate holder as shown in figure 6.6 and placed inside the MCPR. The holder is built to minimize polycrystalline growth along the rim of the substrate. The two different parameters, i.e. depth d of the substrate pocket recess below the top surface of the substrate holder and the gap w from the edge of the substrate to the edge of the pocket recess holding the substrate, are important to control the growth rate of diamond and minimize the growth of unwanted polycrystalline diamond. In these work the d values used were, 1.8 mm (for 24 hours long growth on bevels), 1.6 mm (for 2.5 hours short growth) and 0.9 mm (for parallel offcut substrates), whereas for all growths w was kept fixed at 1.5 mm. These holders are made from molybdenum and polished on both sides. The deposition reactor was pumped down to reach a low vacuum and the leak rate was checked for each run to minimize any external leak from the atmosphere to ensure that the growth takes place in a low nitrogen impurity environment.

As a pre-growth treatment, the substrate was plasma etched for 1-1.5 hour at 180 Torr by a hydrogen discharge to get rid of (a) any damage caused by mechanical polishing, and (b) any

impurities that could still be present on the surface. Some of the established etching methods to remove defects generated from polishing damage include reactive ion etching and hydrogen plasma etching. For the etching step, care needs to be taken to keep the surface relatively smooth. H_2/O_2 plasma has also been used as a pre-treatment method before growth [129], but occasionally this method leaves deep etch-pits formed on the surface. Hence in all our growth process we settled for a 90 minutes H_2 plasma etching process (at T ~ 1030º C) as a pretreatment. This resulted in the removal of close to 1 μm from the top surface. The growth chamber is then pumped down for at least an additional hour before moving to the actual growth process.

All depositions of single crystal diamonds for this work were conducted at 240 Torr. The microwave power is initiated to the reactor at ~5 Torr and the pressure/power is increased in suitable steps to reach a substrate temperature (1080°C~1100°C) range and maintained further to have a fixed temperature during the entire process. A short 10 min hydrogen plasma etch process at 240 Torr preceded the addition of methane that was then flowed into the deposition reactor. The methane was slowly added (1% for 2 min, 2% for 2 min, 3.5% for 3 min and 5% for the rest of the run) to avoid any sudden spike of methane flow at the initial stage of the growth. The deposition was then performed at a constant temperature, fixed total gas flow rate (5% CH_4 added to H_2 gas with the total flow rate of 420 sccm) and fixed pressure condition. The input power was maintained around 2 kW with minor adjustments to achieve the desired substrate temperature. The temperature was read by a one-color pyrometer (Ircon Ultimax, emissivity at 0.1).

The introduction of the methane often gives rise to temperature increases and therefore the power control dial needed to be frequently adjusted to get the right temperature during startup. This process suffered from having lack of good control over temperature. There were two approaches taken to fix this issue; (i) an Arduino uno was paired with a stepper motor and a rotary

encoder to precisely rotate the power dial and (ii) methane was fed into the chamber in a controlled amount as 1% for 2 minutes, 2% for 3 minutes, 3.5% for 3 minutes and then 5% for rest of the growth time. This recipe with a precise control in the dial has been quite successful in avoiding any sharp rise in temperature and allowing the temperature to slowly rose to its target value.

After completion of the deposition process, the final substrates were cleaned in boiling nitric and sulfuric acid mixture (1:1) for an hour followed by ultrasonication in acetone and methanol. Before and after each deposition the thickness of the substrates was measured by linear encoder (Solartron DR600) and were weighed using a micro balance (Mettler Toledo XS105DU, with accuracy of 0.0001 g). The thickness was measured by linear encoder near the edge of the substrate and at the center of the substrate before and after the growth process to estimate the distribution of the growth rate, especially for the bevel cut substrate offcut along the (100) direction. For (110) offcut direction substrates all the thickness was measured along the diagonal of the substrate. The same procedure was followed for thickness measurements in parallel offcut substrates. The deposition duration times used were 2.5 hrs, 12 hrs and 24 hrs. The growth rates at different points of the substrates were calculated by the average grown layer thickness divided by the growth duration. A Nikon ME600 optical microscope and an SZM stereo microscope are used to look for the surface texture and features. The surface textures were further quantified using a Dektak surface profilometer and Hitachi 5100N atomic force microscopy.

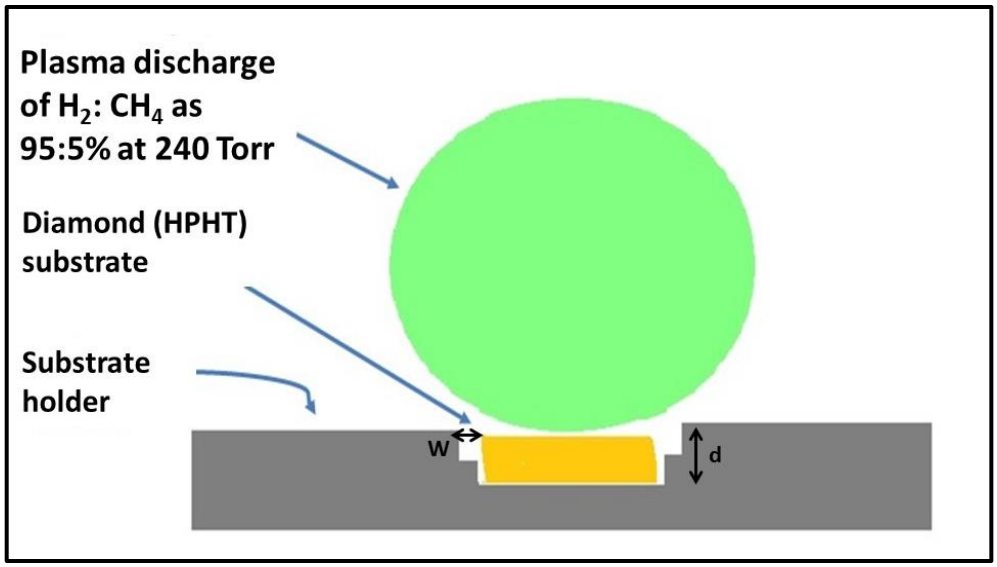

Figure 6.6. Schematic of a diamond deposition process showing the pocket recess that holds the diamond substrate

6.4. Optical characterization of offcut grown samples

6.4.1. Operation of optical microscope

An optical microscope is an important tool to analyze features that is present on the surface of the substrate or grown layer (when a snapshot of the top surface is collected from the light reflecting from the surface) or even the strain present inside a free-standing layer (through the light transmitting through the sample and its cross polarization). The first method is applied either for dark field imaging or bright field imaging or occasionally differential interference contrast imaging (DICM) where in all these cases, light is illuminated from the top of the sample through a selective lens and the reflected light is focused through the objective lens. For DICM a prism is brought in the pathway of the incident light which based on its position can split the beam into to partial beam separated by wavelength.

In the light transmission method, i.e. mostly for birefringence analysis, light from the bottom of the sample travels through it and two polarizers are placed with their polarization axis at 90° to each other on either side of the sample. Any non-refracted light will be blocked by the polarizers and will appear dark in the eyepiece or any captured image. However, any strain in the substrate/sample will result in additional refraction and therefore the refracted light will propagate through the second polarizer. These strained regions will appear very bright in the captured image. Quantitative birefringence analysis has not been conducted in this work, however qualitative images are used in some selected cases.

For the optical characterization into this work, a Nikkon eclipse ME600 optical microscope was used. This particular instrument is configured with 2.5X, 10X, 50X and 100X objective lenses. The following pair of schematics in figure 6.7 (a & b) show the two basic operational mode of the optical microscope. The first schematic shows how a birefringent prism (4) is adjusted to split the incident beam into two beams differed by wavelength. When the two beams strike a rough surface, due to their lateral displacement reflects back with a path difference. Once the beams are converged back through the prism and

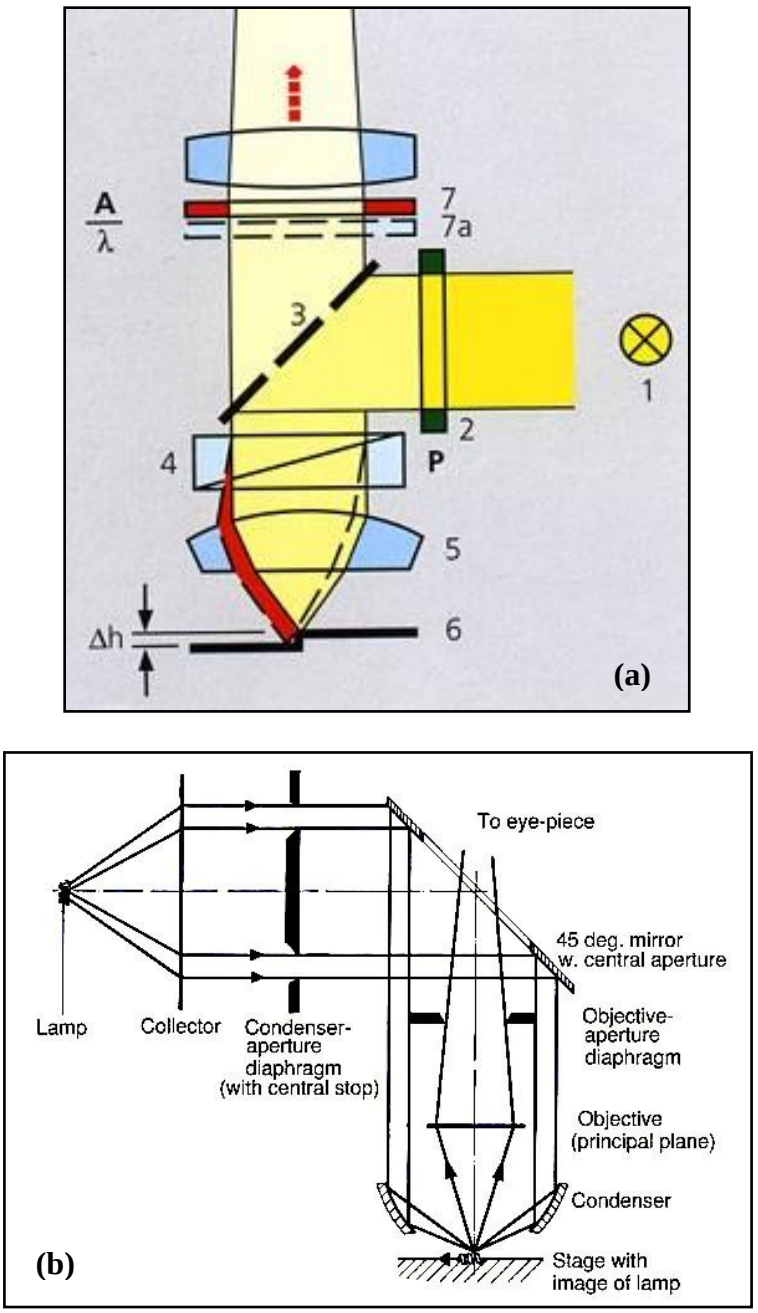

Figure 6.7. (a) Schematic of differential interference contrast imaging (DICM) mode (b) Dark field imaging mode [130]

the analyzer lens (7) the path difference gets converted into grey values and appears as distinct feature in the eyepiece or collected image. The auxiliary plate (7a) can be adjusted to change the

grey values into different colors. In the next schematic, i.e. Dark Field (DF) imaging, a condenser aperture is inserted to block the direct beam. A 45° mirror is used to focus the secondary beam on the object and then finally the reflected light enters the objective lens and is directed to the eyepiece or camera to capture the image.

6.4.2. Observations and discussions

A standard 3.5×3.5 mm^2 commercial HPHT substrate (from Sumitomo Carbide), and a commercially available CVD substrate are shown in figure 6.8 after the acid cleaning process. Generally, these substrates come with a thickness around 1.4 mm, however based upon the offcut preparation approach the thickness varied. These images show that the substrates are of good quality i.e. without any visible defects and properly polished along <100> or <110> directions. This image is captured with a 25X magnification setting (the white marker line represents 400μm.). The corresponding pair picture shows the birefringence image captured using the cross polarizer.

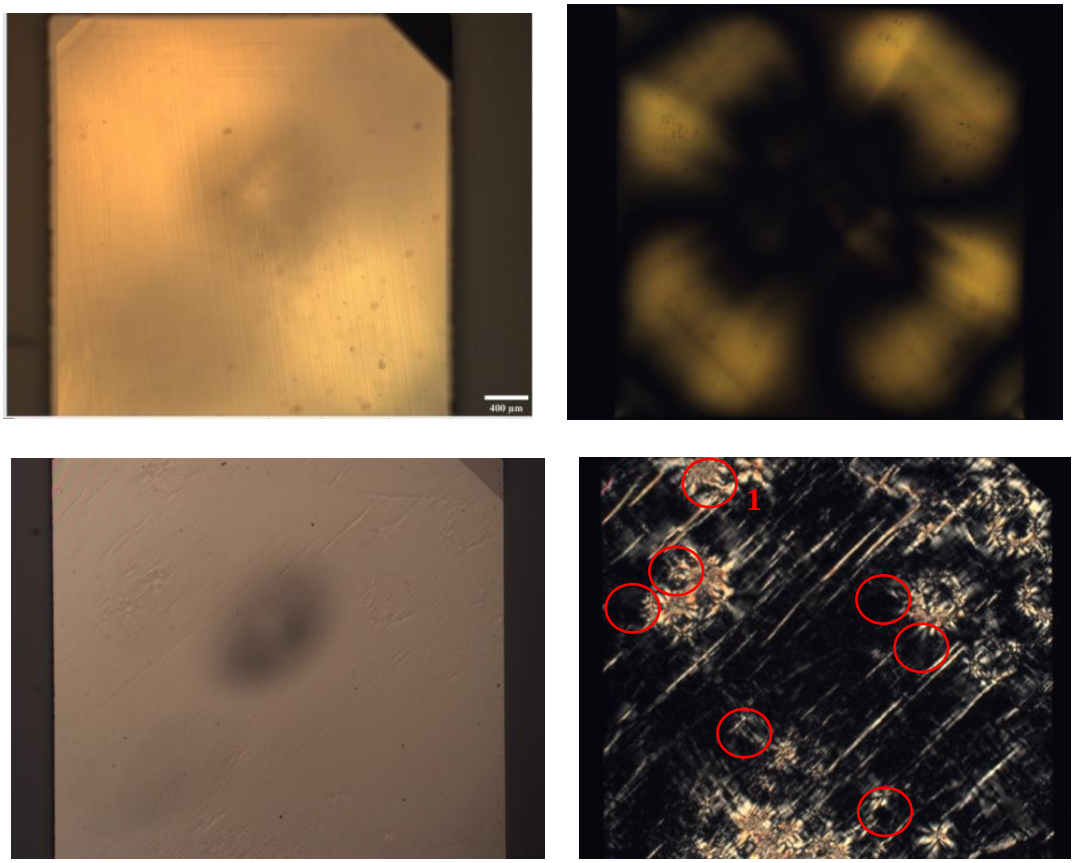

Figure 6.8. An image (25x) of a polished HPHT substrate and corresponding birefringence (top row) and image (25x) of commercial CVD plate and corresponding birefringence (bottom row)

It is evident from the bottom pair of pictures that surface damage occurred during polishing on the CVD plate (numerous scratches are found along the diagonal and this has also resulted into strain present closed to the surface (red circles). There are some threaded dislocations also seen on the surface (which appears almost like four lobes 90° apart, as seen in red circled locations). Altogether these pair of diagrams help one to decide about the feasibility of a substrate selection, and an expectation of a good quality of deposition.

However, there are other parameters that also play crucial roles during growth of a defect free thick diamond layer namely; substrate temperature, energy density of plasma, purity of feed gases as well as amount of nitrogen present in the growth environment. There have been multiple reports [111,131] that show how additional nitrogen in the growth process aids towards higher

quality of surface finishing as well as higher growth rates. However, any deliberate addition of nitrogen comes with the cost of a substantial deterioration of electronic properties in the crystal. Therefore, in this work we try to develop processes to grow thick diamond layer (~ 200 μm) in a low nitrogen environment. But growing thin epi-layer or thick layer of diamond in low nitrogen environment is challenging as the surface in most occasions gets filled up with defects, as seen in figure 6.9. Figure 6.9 (a) shows a 25X magnification and (b) shows 100X

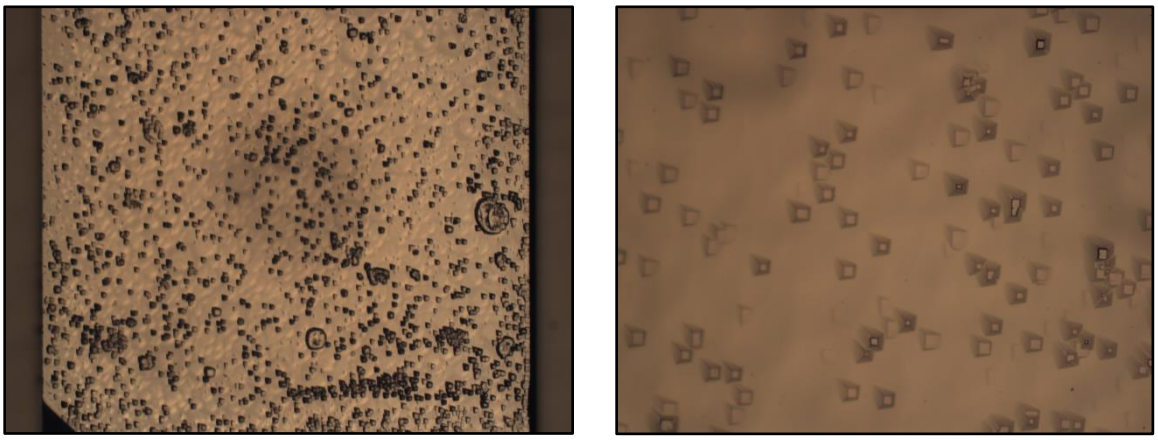

Figure 6.9. An optical micrograph (25X) of an epilayer deposited on a commercial CVD plate (left) and the same surface looked at higher magnification (100X)

magnification of a 30μm epi-layer deposited on a commercial CVD substrate. As evident from the higher magnified image the surface has pyramidal and flat top structures. The flat top structures or the pyramidal structures mainly appear from extended defects, i.e. edge dislocations [122]. In general, these defects propagate all the way to the grown layer especially when grown in a very low nitrogen impurity environment and they end up as a pyramidal or flat top type structures on the deposited layer. A remedy to this problem is to deposit diamond on a misoriented substrate. A growth mechanism on a misoriented surface versus an almost flat surface had been discussed by Lee at. al [132].

To avoid the pyramidal and flat top structures at low nitrogen growth conditions this study used offcut angles of 2.5, 5 and 10 degrees. The optical micrographs in figure 6.10 shows the surface profiles of substrates grown at different offcut angles for different durations.

	2.5°	5°	10°
2.5 hr	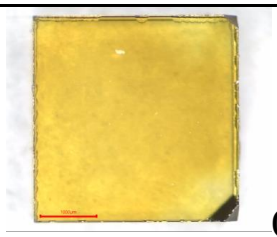 (a)	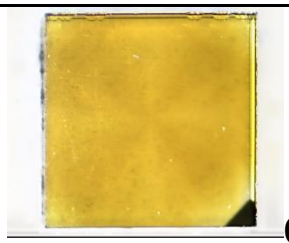 (b)	 (c)
12 hr	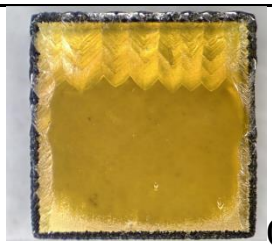 (d)	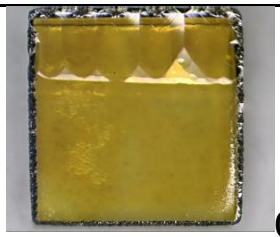 (e)	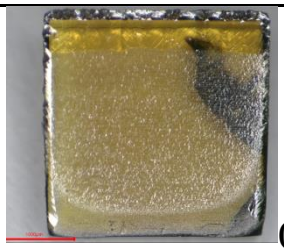 (f)
24 hr	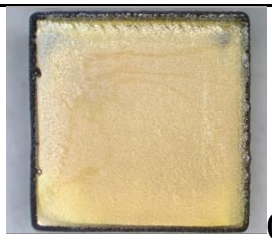 (g)	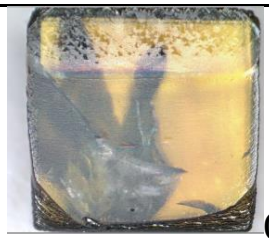 (h)	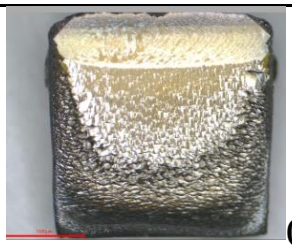 (i)

Figure 6.10. Top surface of SCD deposited layers for different offcut angles ([100] direction bevel) & different growth durations. The thinner edge of each beveled sample is facing the bottom of each micrograph

All the substrates in figure. 6.10 had very minimal polycrystalline diamond grown on the top surface or at the edges of the top surface. However different surface features evolved with longer duration of growth and higher offcut angle. Also, it is important to note that corners of substrates (a, b and c) were purposefully laser cut/marked and therefore the grown top surface`s appearance and the black corner are not related. However, there are two distinct features observed in the figures 6.10 (f) and 6.10 (h) where a dark structure has encroached partially in the grown sample. By

carefully adjusting the focusing on the microscope it was found that the dark patch is present close to the interface where the growth began, and not on the top growth surface. A possible explanation of this dark patch is that a layer of cracking starts at the edge of the sample and propagates inward. These darker patches do not appear to interfere with the diamond growth, so the cracking probably occurs at the end of the run when the substrate cools after the deposition. This phenomenon is not observed on the other substrates. Further depositions were carried out on two different types of offcut substrates as shown in figure 6.11, including (1) on substrates with a bevel structure offcut along the [110] direction (Figs. 6.11 (a) and (c)) and (2) on parallel cut substrates with the offcut along the [100] direction (Fig. 6.11 (b) and (d)). The thickness of these grown layers on the substrates was around 250 μm after a growth time of 24 hrs.

Off-cut type /Off-cut angle	**(110) bevel cut**	**(100) parallel plate**
5.0°	 **(a)**	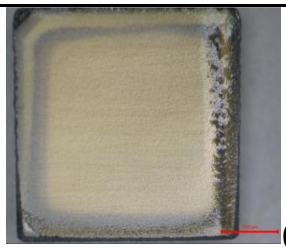 **(b)**
10.0°	 **(c)**	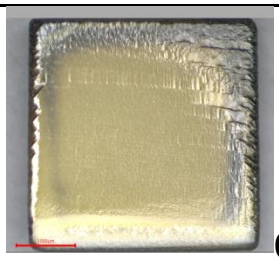 **(d)**

Figure 6.11. Top surface of deposited layer on [110] bevel and [100] parallel substrates

A feature is found along the thinner edge of 10° offcut bevel [110] direction and [100] direction substrates (figures. 6.11(c) and 6.10 (i)), i.e. the thinner edge appears rougher than the

rest of the samples. A possible cause could be that the plasma doesn`t cover the thinner edge uniformly during deposition. This effect is very minimal on the parallel substrate growth (figures. 6.11 (b) and 6.11(d)). An interesting feature that is observed on the top surface of all the bevel cut [100] samples is a patch of area that grows out flatter (closer to the (100) crystallographic plane) on the section that has the highest crystallographic planes. This indicates the addition of new crystal planes occurs slower than the lateral growth along the step-terrace region of the sloped offcut surface. Fig. 6.12 (a) & (b) shows the top and side views of 24 hours growth runs with the offcut of 2.5° at the top right corner to 10° at the bottom left. The lateral growth becomes more prominent on the side view of the surfaces.

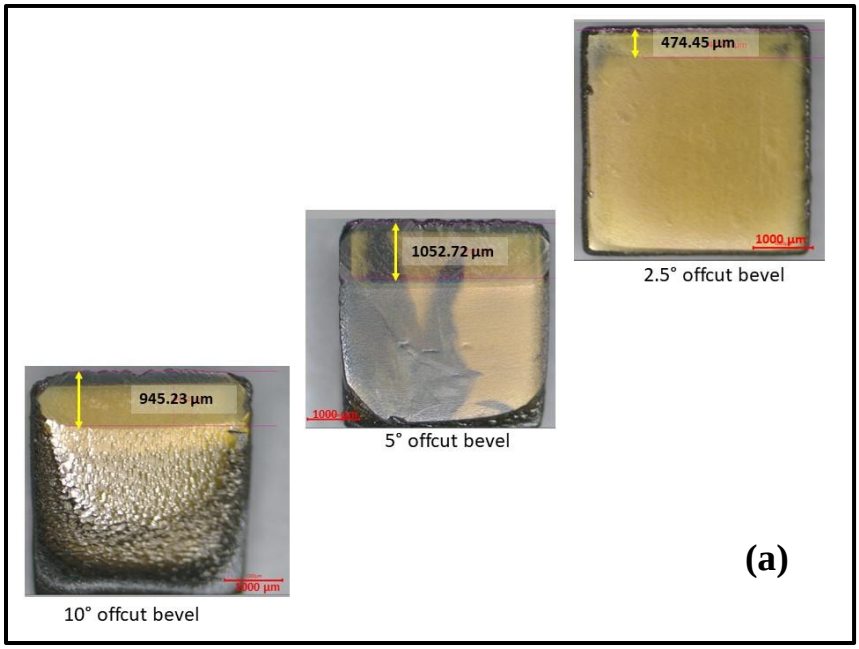

Figure 6.12. The top surface and side view (a & b) of three different offcut angles (2.5°, 5° and 10° along [100)] bevel) showing the lateral growth of the deposited layers. All pictures are for 24 hours growth

Figure 6.12 (cont`d)

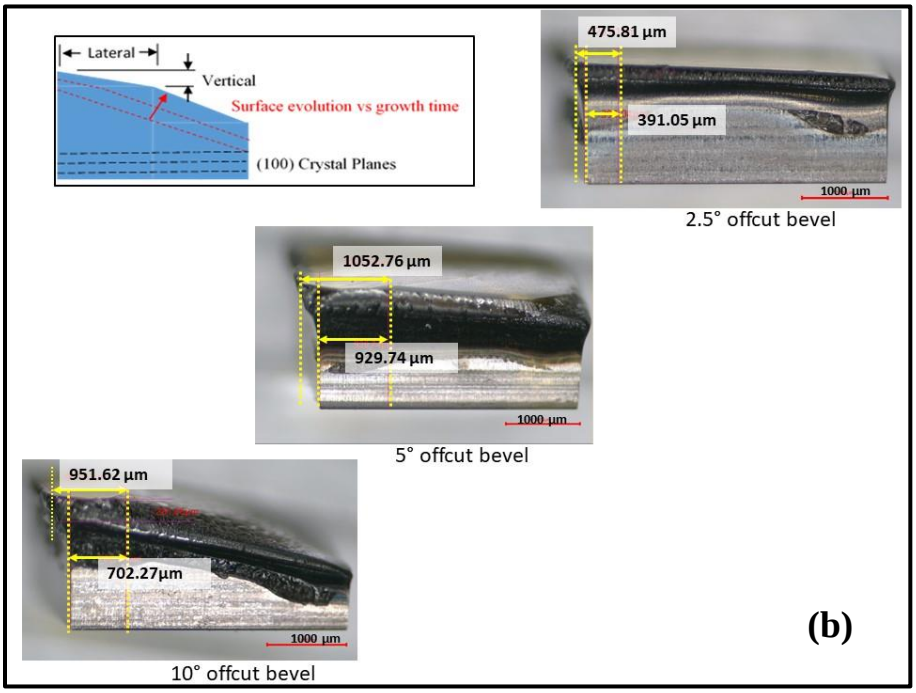

The lateral area also partially extends out from the substrate to the left in the figure 6.12 (b) pictures, which indicates an area gain from the original substrate top surface to the growth surface. The notion of lateral area growth/increase becomes clear from the magnified side view of all the grown surfaces as shown in figure. 6.12 (b). Referring to the top grown surface, the 2.5° shows a low lateral growth (half compared to the other offcut angles), which is possibly due to the substrate being 150 µm thinner compared to the other two substrates, i.e. it was slightly deeper inside the pocket recess of the holder as shown in figure 6.6. The other two offcut growth experiments in figure. 6.12 show nearly the same length of lateral growth (however different surface texture). We also looked into the vertical growth rate (V_P) and the lateral growth rate (V_L) of these three substrates.

Table 6.1. Lateral and vertical growths on different offcut angle substrates

Offcut angle	Lateral growth rate (V_L) in μm/hr	Vertical growth rate (V_p) in μm/hr	V_L/V_P
2.5°	16.3	8.0	2.03
5.0°	33.7	14.9	2.25
10.0°	29.4	14.6	2.02

To measure the lateral growth rate, the corresponding length of lateral expansion (from figure 6.12 (b)) is indicated on the top of the side view of the sample. A line was drawn from the tip of the length to the edge of the substrate to find the segment that had grown laterally. This length is used to estimate the lateral growth length and then the lateral growth rate. The ratio of lateral growth rate and the vertical growth rate shows a nearly constant value for this particular pocket depth as seen in table 6.1. Hence it can be stated that the ratio stays almost independent of the offcut angle for this set of growth conditions.

The overall vertical growth rates of the substrates with different offcut angles are summarized in figure 6.13. As mentioned earlier the thickness were measured by a Solartron DR600 linear encoder. For each substrate, data points were collected at multiple positions (all edges and the center for beveled [100] offcut direction substrates and along the diagonal for [110] offcut direction substrates) on the surface and averaged over three times at each location. This was done both before deposition and after deposition to get the growth rate at each point.

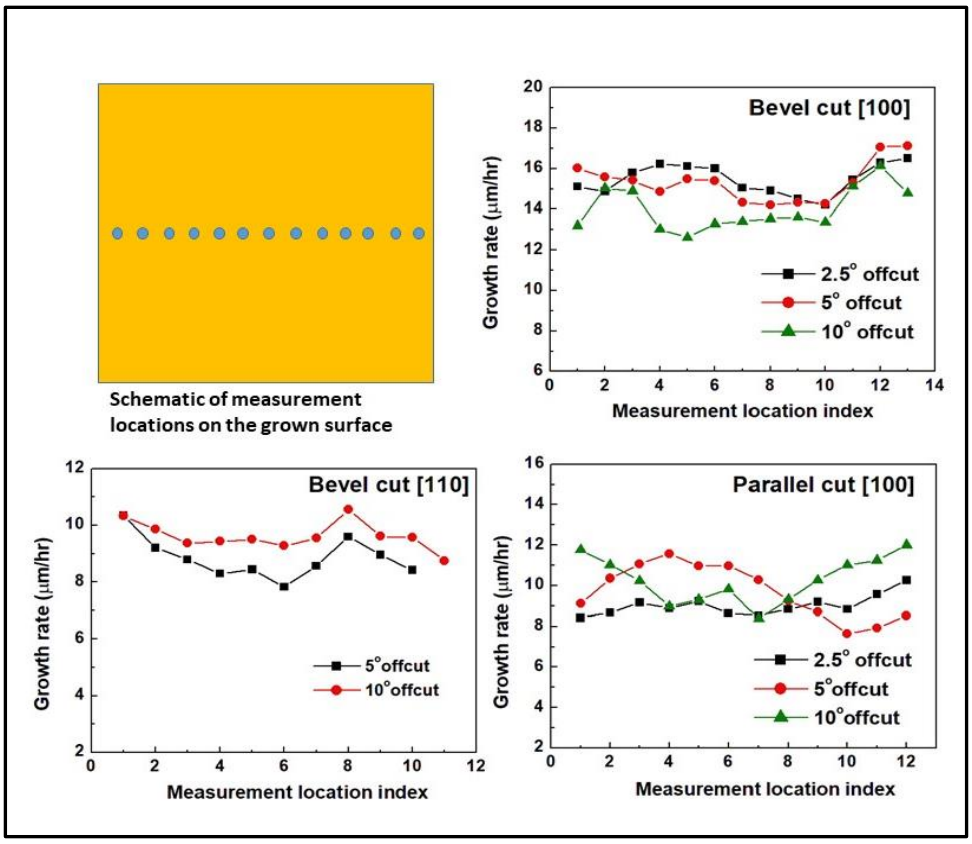

Figure 6.13. Vertical growth rate of deposited layer on different offcut samples measured at different locations for 24 hours deposition

Figure 6.13 shows there is minimal variation in the growth rates at different locations on the substrate. The slight variation in the growth rates are partially due to surface morphology arising from the angled substrate and the overall roughness. However, there is no large variation found in the growth rates within each individual substrate. One difference is the marginally higher growth rate is observed in the [100] bevel direction growths (top right plot in figure 6.13)). This possibly occurred because of a slightly higher N_2 presence in the plasma during deposition. The reactor, especially the gas flow system had gone through some minor upgrades after the [100] bevel direction runs and before the other runs. Typically, a slightly higher nitrogen impurity level in the deposition produces a higher growth rate if all other parameters are held unchanged.

6.5. Study of distribution of step and terrace growth

The growth of homoepitaxial (001) diamond is guided mainly by two processes, formation of new islands (planes or terraces) and propagation of steps at the end of crystal planes (terraces) [126]. It is noteworthy that the formation of new islands (planes) of diamond also is enhanced due to presence of defects. This island formation is at a faster rate in defect regions as compared to low defect concentration regions [133]. The defect region can be from either threading dislocations or from foreign particles present on the substrate surface. A surface with a low offcut angle (< 0.5°) is always prone to end up having pyramidal or hillock type defects since in such cases there are few steps, and the island growth from defects takes a dominant role. In general, the suppression of these hillock structures happens for offcut angles above 2°. In this section we look into how steps and terraces arise out of different offcut angles and the effect of the offcut angle on lateral growth (100) in comparison to perpendicular growth (001). Step and terrace structure appearance is a common phenomenon for crystalline samples. In general, any crystalline surface is comprised of both micro and macro steps. Macro steps mainly grow due to step bunching of micro steps. Also, the offcut from the (100) plane initiates the micro steps and based upon the angle of inclination and the exposure of the top surface to the plasma, the growth proceeds by further propagation of the steps in the [100] and [110] directions.

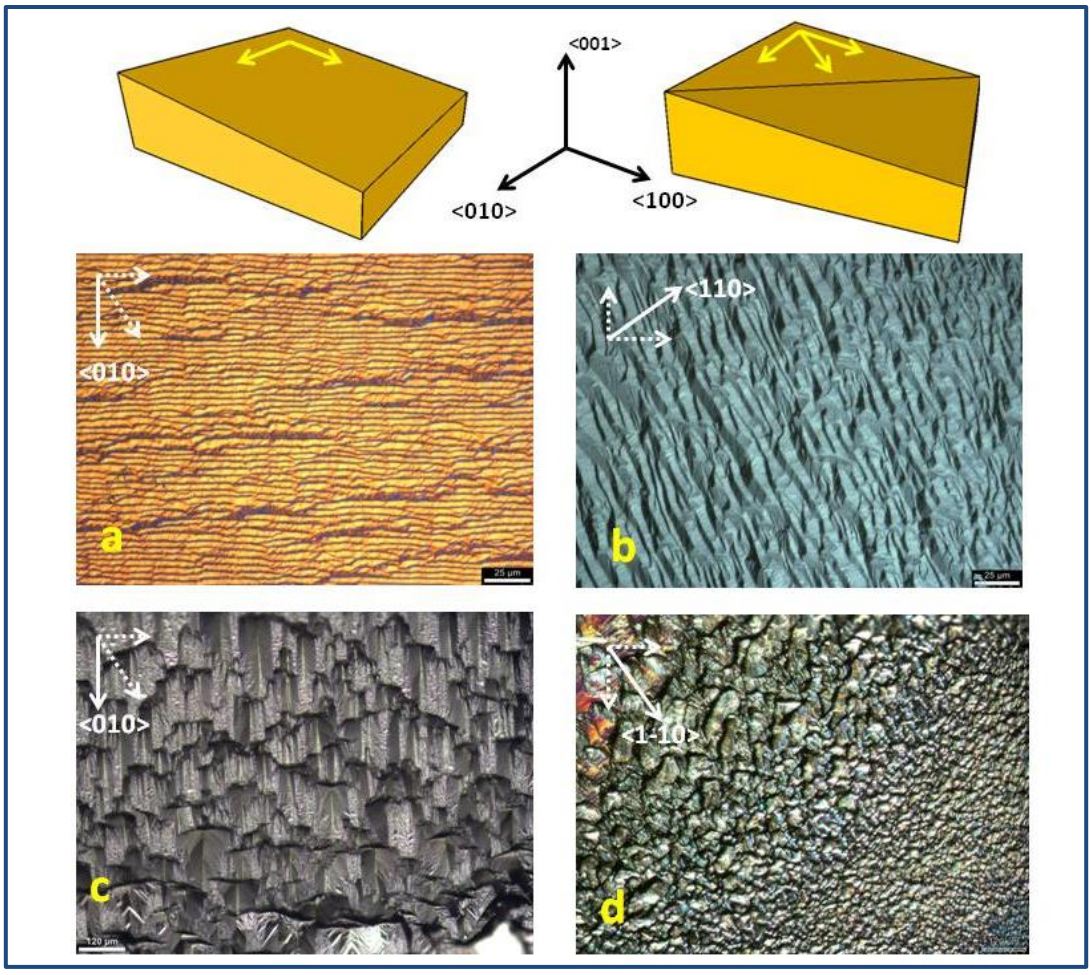

Figure 6.14. High magnification (500x) pictures of step-terrace formation (a) 5° bevel (c) 10° with the bevel along the [100] direction and the corresponding [110] direction bevel at (b) 5° and (d) 10°

The behavior of the step and terrace size distribution as well as the bunching is determined by the local growth conditions of the deposition plasma. This growth is affected by the shape of the top surface inside the pocket recess with respect to the deposition plasma, i.e. the bevel cut shown in figure 6.14 can experience different plasma conditions across its surface as compared to a parallel cut substrate due to non-uniform plasma interaction due to the slope. As evident from figure 6.14 an offcut angle close to 10° ends up to a very rough surface irrespective of its direction of inclination.

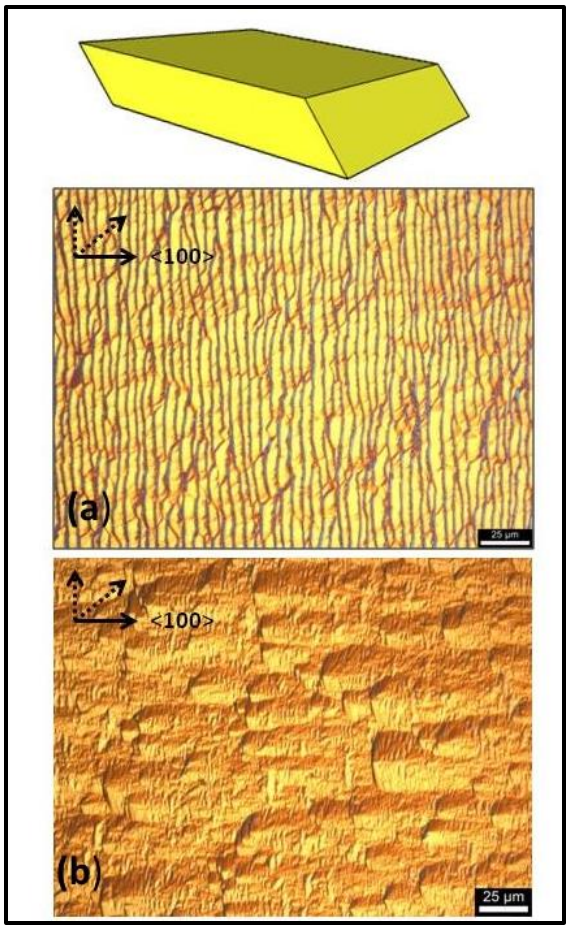

Figure 6.15. Step and terrace propagation along (a) 5° and (b) 10° offcut parallel substrate growth

However, looking into the surfaces of parallel substrates with offcut angles, it is evident that a uniform plasma-substrate interface creates a more uniform flow of steps and terraces. Although there is a significant difference among the two surfaces shown in figure 6.15, both show a steady terrace and step propagation along [100] direction across the entire surface. However, the separation of the terraces and their bunching looks much different in the 5° compared to 10°. The 10° offcut parallel substrate shows some micro-steps on top of macro structures. Also, the micro-steps are more densely situated in the 10° offcut sample. This makes the 10° offcut substrate having higher surface roughness compared to the 5° offcut substrate growth. Therefore, a collective observation of all these different kinds of offcut angle growths generates a keen interest to

understand more about the distribution of the steps and terraces with respect to the type of inclination of the surfaces. A quick observation of all the surfaces suggests that the terraces and steps grow very differently for bevel structures of different angles and therefore the local impurity/doping concentration variations in the grown layer may be dissimilar on all these different surfaces. Hence this section will focus on surface topography characterization to quantify the overall distribution of step heights and terrace widths. Figure 6.16 shows a first attempt to quantify the steps and terraces, an AFM scan of the thicker flat region of the sample in Fig. 6.10 (i). A Hitachi 5100N atomic force microscopy with 20 nm tip is used in DFM mode for this scan. A 20 X 20 μm^2 area is scanned on the flat part of the sample. The average surface roughness for this area is ~ 40 nm. In the same set, figure 6.16 shows the step and terrace distribution along selected line scans shown as red and blue lines. The step heights vary between 90 nm to 150 nm and the terrace widths are distributed around 4.5 μm. But these numbers are drawn over a short scan length only, which allows selected precise detection of steps and terraces but not a statistically significant full distribution. It was difficult to measure areas outside this flat region as the surface is too rough and sloped for the AFM instrument.

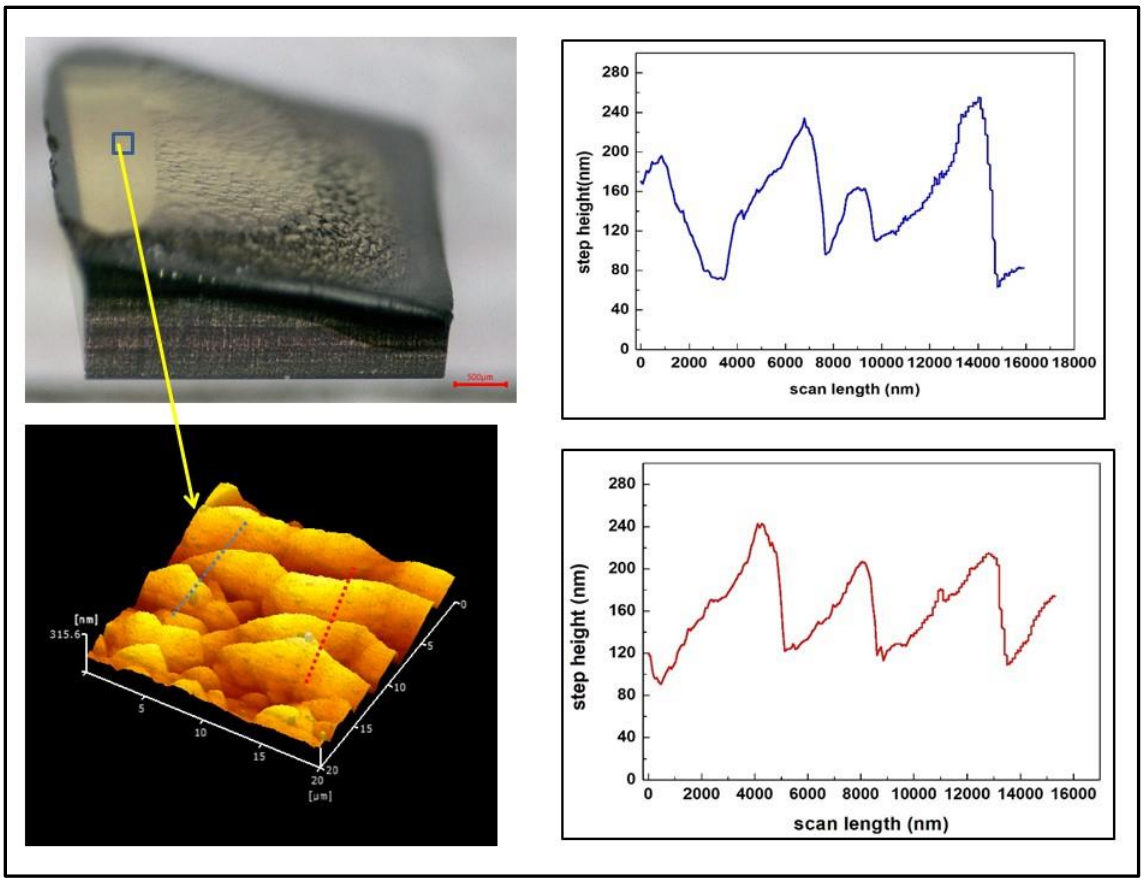

Figure 6.16. Surface roughness profile of a selected area (flat region) of 10° bevel growth

A Dektak profilometer was then used to measure the rougher surfaces. A Veeco Dektak 6M profilometer with a 5 μm diameter tip and 5 mg force was configured to measure a roughness scan. Before proceeding to the next part, it is important to have a brief discussion about how a stylus based DEKTAK profilometer works.

6.5.1. Basic operation of DEKTAK profilometer

The DEKTAK surface profilometer is a common instrument to analyze surface characteristics where a stylus with a small diameter, made mostly from diamond or other material moves over a selected scan length (in contact mode). The displacement of the spring loaded stylus

is translated to a Z variation (height measurement) of the features under study. An electro-mechanical transducer is attached to the stylus which converts any variation of mechanical force to electrical signal, better known as linear variable differential transformer [134]. Figure 6.17 shows a schematic of the basic

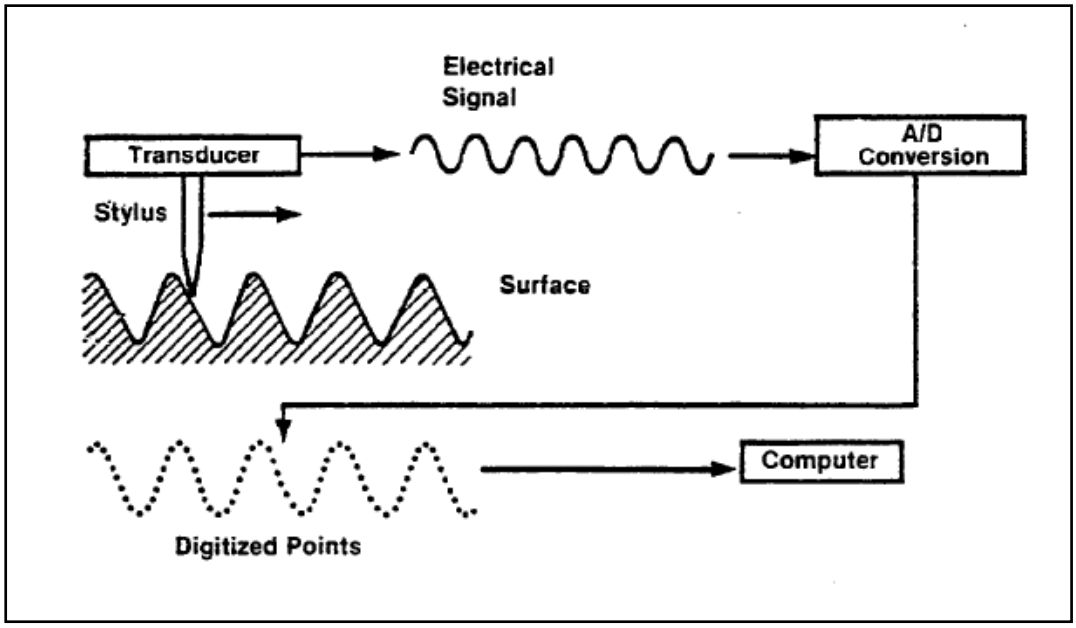

Figure 6.17. A schematic of the operation of stylus-based surface profilometer [134]

operation of the transducer. The sensitivity of the transducer is approximately 1 Å, where the stylus is attached to a ferrite core which ultimately forms an AC bridge. Any movement in the stylus causes change in the balance of the bridge. Any demodulation or amplification of the signal is converted to a voltage which is finally converted by analog to digital converter to read the value that is then stored by software. The sensitivity of the measurement largely depends on the stylus tip and the stylus force. Typical tip diameters are 2~10 μm and the force is set to 5~20 mg. Any broader tip otherwise will miss finer surface features and higher force could be detrimental both

for the film under measurement as well as lifespan of the tip. Figure 6.18 shows the adjustable stage and other controls of a Veeco 6M profilometer[135], which is used for this study.

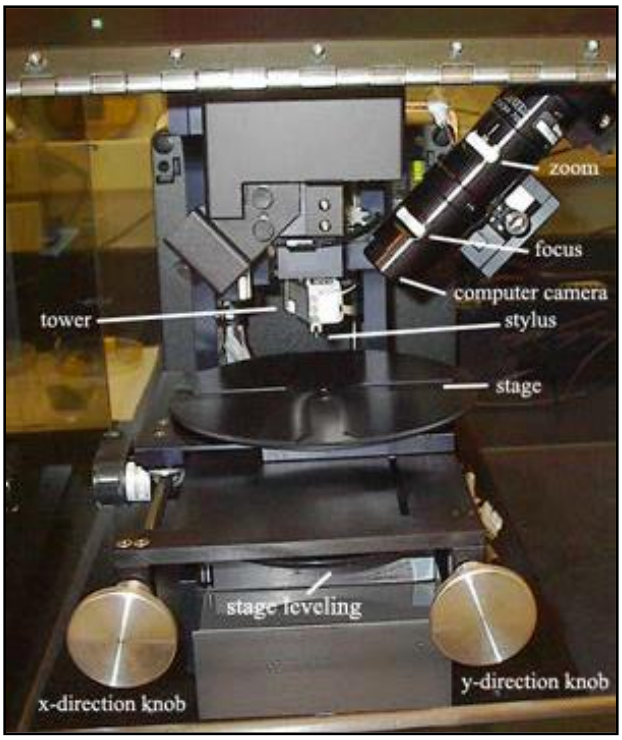

Figure 6.18. Image of the measurement stage of Veeco 6M profilometer [135]

A software allows the stylus to be lowered down to or raised up from a sample. The x/y-direction knobs help to center the sample (especially for small size samples). The scan length, scan time, and resolution can be adjusted by the software program. For the measurements of this project a scan length of 1000 μm is selected with the time of scan set to 140 sec to get the maximum resolution. The stylus force is set for 5 mg or 49μN.

6.5.2. Observations and discussions

A Veeco Dektak profilometer with a 5 μm diameter tip and 5 mg force was configured to measure a roughness scan. In most cases the scan length was restricted to 200~500 μm based on the inclination of the surface. The steps and terraces are scanned with the probe tip and then the step height and terrace width are calculated as shown in figure 6.19. This figure shows the scanning over a rougher area. Often the traced curved was leveled to identify and quantify the terraces and steps as shown in figure 6.19 (b). Measuring micro-steps was challenging for this tip, and therefore it looks primarily at terrace widths close to 5 μm and above due to the tip size. The DEKTAK32 software plots the raw data and the step and terrace sizes were determined from the plots manually. Figure 6.20 shows the distribution of terrace and steps over a small scanned range, from the sample with 10° offcut (same sample as shown in figure 6.10 (i)). This figure basically serves to illustrate the process followed for step/terrace tracing and their height and width calculations. Five scans at different spots of the sample (mostly at/near the center, unless specified) were performed and a distribution frequency of the step height and terrace width was constructed as shown in figure 6.20. Each bin in the x axis of figure 6.20 represents either a range of terrace widths or step heights. The y-axis shows the distribution frequency of the corresponding bin.

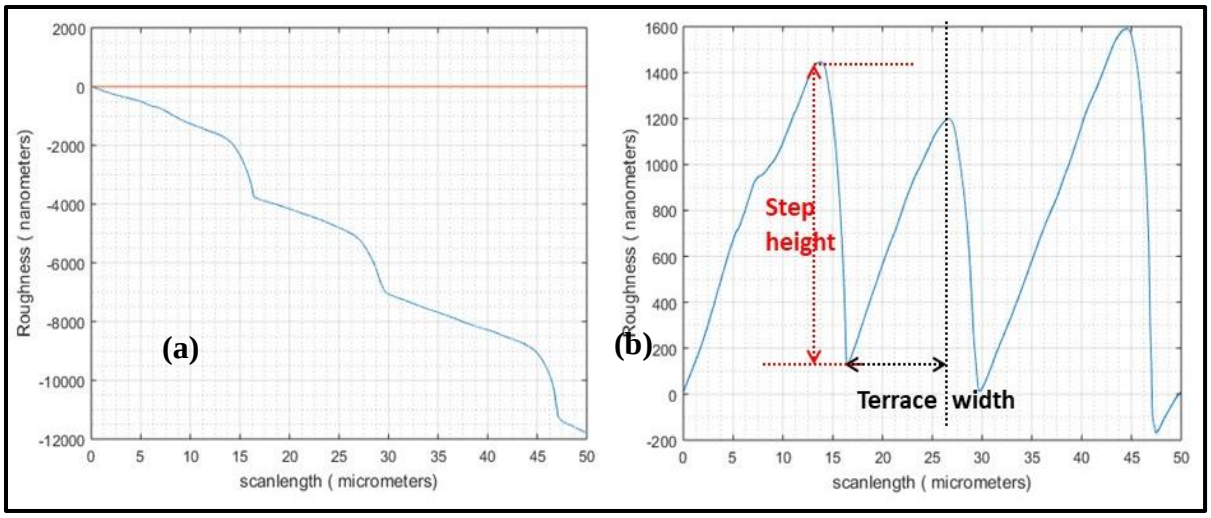

Figure 6.19. Schematic showing leveling (from (a) to (b)) and measurement of step height and terrace width on a 10° offcut bevel sample

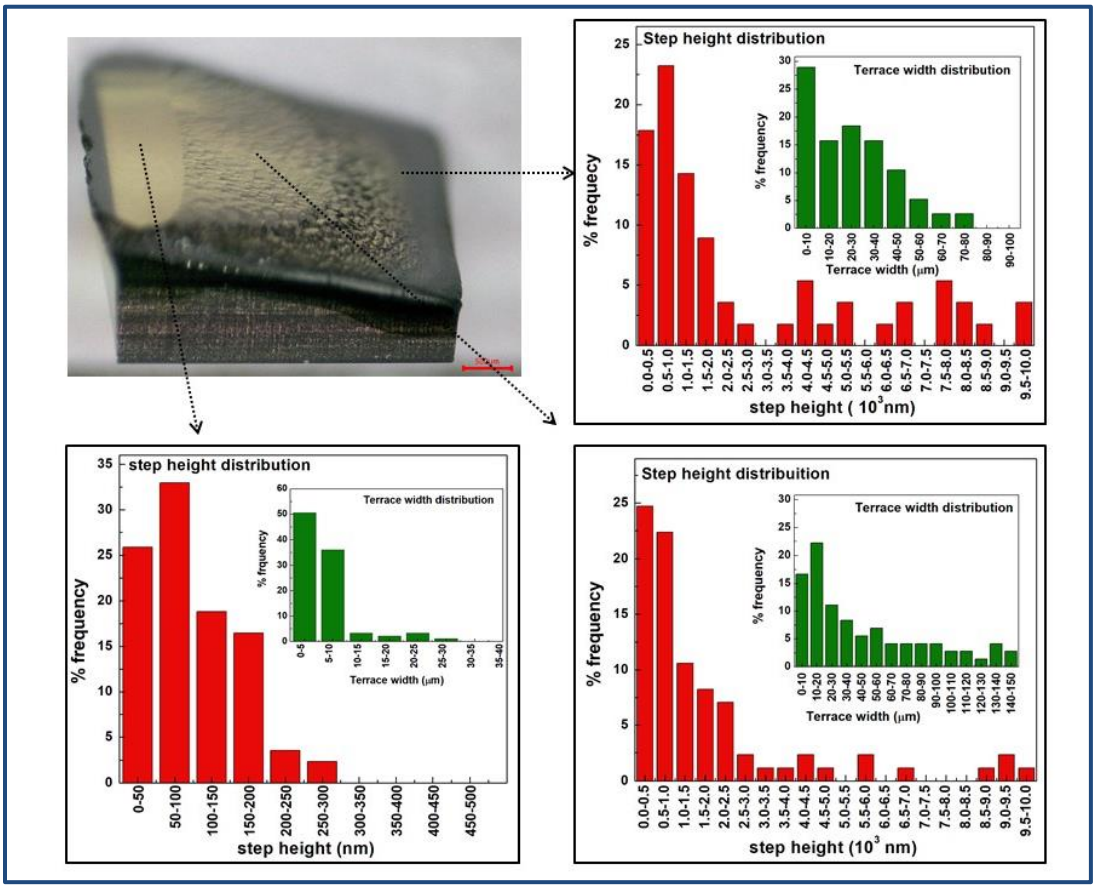

Figure 6.20. Step-terrace distributions (bar diagrams) at different sections of the 10° offcut [100] bevel direction grown layer

Figure 6.20 shows an example of the step height and terrace width distribution analyzed and represented in a diagram from different regions (as pointed by the arrows) of the substrate grown at a 10° offcut and beveled along the [100] direction. The microscope picture itself shows differences among the selected regions of the sample. As seen in the thicker and flatter portion of the substrate, the step heights are maximum around the 50~100 nm bin, and terrace widths have a distribution that is highest in the 0-5 μm bin (inset picture). The other two distribution plots required that the step height distribution scale be changed to the μm (10^3 nm) scale to accommodate all the distribution, which clearly indicates these regions are rougher. A notable feature is that comparing the mid region to the thin (right) region, one finds the bar diagram has wider distributed tail for the thin region (in other words, it is slightly rougher from the mid region). Also, the terrace widths in some cases are long (extending close to 50 μm) in the rougher regions. The overall distribution helps to quantify the observation from optical micrographs that a 10° offcut sample becomes rougher at the longer run times.

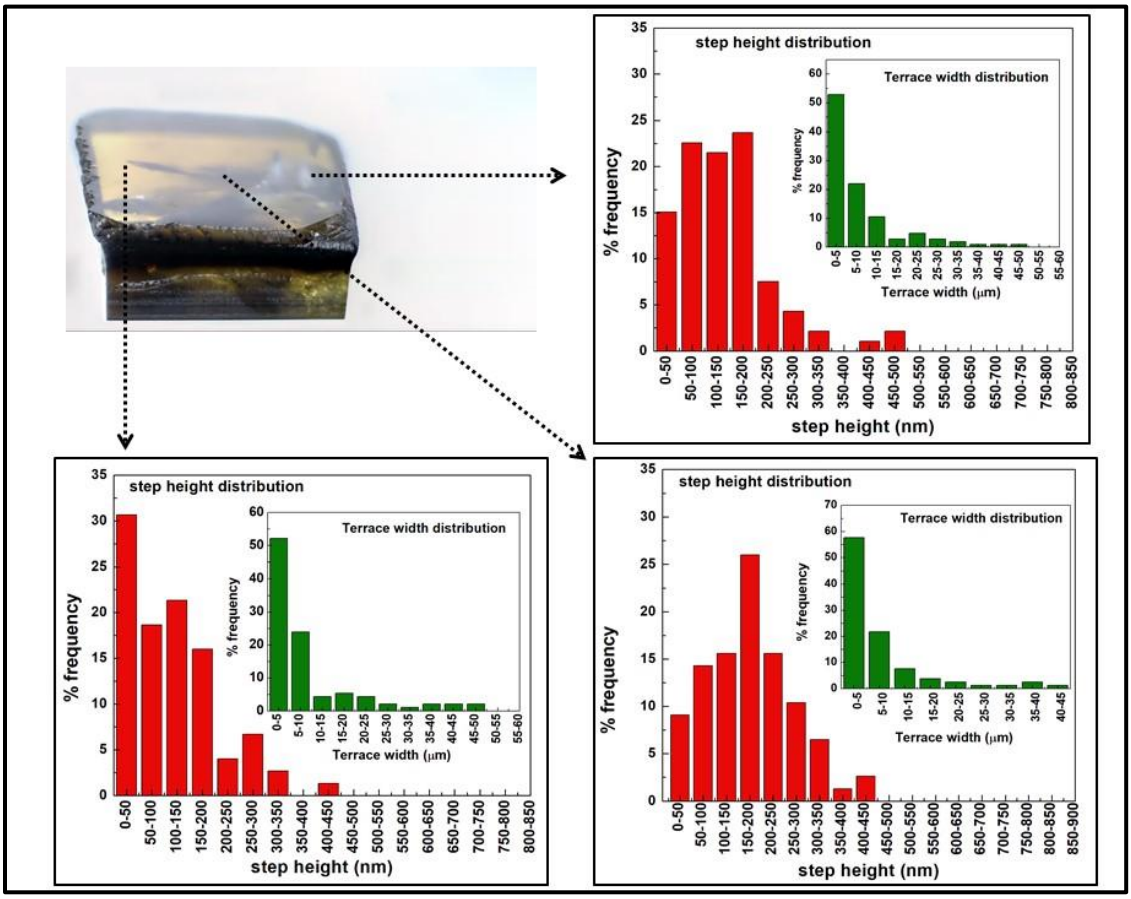

Figure 6.21. Step-terrace distributions (bar diagrams) at different sections of a for a 5° offcut [100] bevel grown layer

The distribution is different and more uniform when we investigate the 5° bevel offcut from the [100] direction substrate growth, as shown in figure 6.21. The same approach (i.e. looking into three regions of the sample) shows that the step height distribution marginally changes from the thicker edge, which otherwise makes the overall sample much smoother compared to the 10° offcut substrate. Also, this results in the terrace width distribution being more uniform. (except at the extreme corner on the thinner end). This general uniformity is likely due to the fact that in the pocket, for a 5° offcut bevel, the plasma can cover more uniformly the full sample and hence a better plasma-substrate interaction for diamond growth.

In figures 6.22 and 6.23 a comparison is made of the diamond growth for the [100] bevel direction, [110] bevel direction and [100] parallel substrates for 5° and 10° offcut angles. In the first set of optical micrographs in figure 6.22 the results for 5° offcut experiments are presented. The two substrates in Figure 6.22 (a) and (c) are both for an offcut direction of [100] with either a bevel or a parallel cut. They show basically the same step flow growth surface morphology, whereas figure 6.22 (b) shows a [110] oriented offcut growth with a slightly different morphology. Comparing the optical micrographs figures. 6.22 (a) and 6.22 (c), as well as their corresponding step-terrace distribution, it can be seen that the mean terrace height for both these surfaces are around 200 nm, whereas for the figure 6.22 (b) case it is close 300 nm, which makes the [110] offcut direction beveled surface slightly rougher. For the [100] and [110] oriented bevel structures (figure. 6.22 (a) & (b)) the terrace width distributions are centered around or less than 10 μm but for the [100] parallel substrate growth, terrace width distributions are slightly extended with a larger population around 15~20 μm.

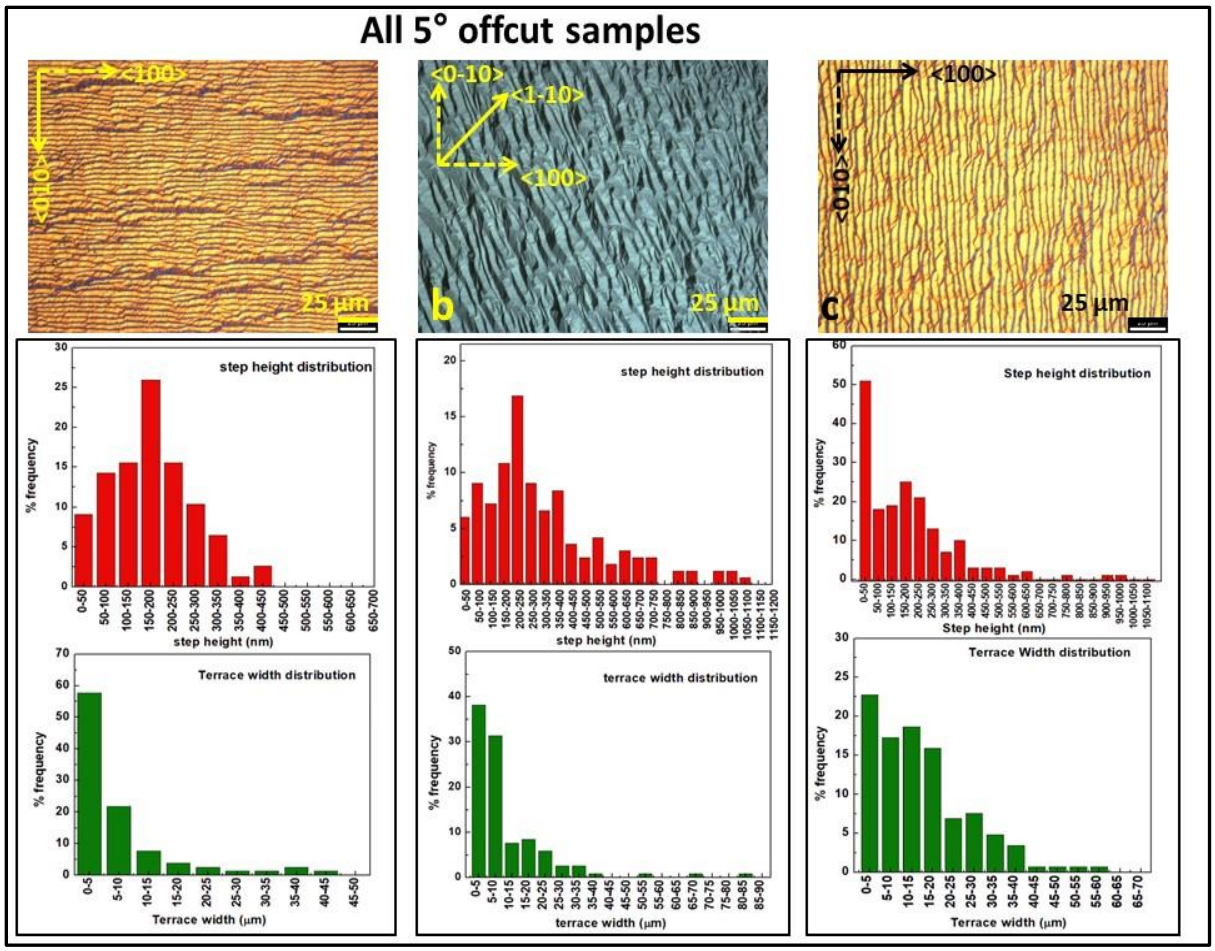

Figure 6.22. Step-terrace structures and their distributions (bar diagrams) for 5° offcut (a) (100) bevel (b) (110) bevel and (c) (100) parallel substrate thick growth

On the other hand, if we look at the 10° offcut samples in figure 6.23 arranged in the same sequence as the 5° offcut substrates in figure 6.22, a major difference is that the bevel offcut substrates in figure 6.23 (a) and (b) are very rough. Both of these grown layers have mean step height around 2 µm. The terraces are also long reaching to 50~60 µm lengths, altogether making the surfaces very rough. But the [100] parallel cut sample in figure 6.23 (c) is smoother. The mean step height drops back to 150~200nm, even though it has some long terraces but overall it is comparable with the 5° substrates. Further comparing, the [100] 5° parallel substrate (Fig. 6.22(c)) and [100] 10° parallel substrate (Fig. 6.23 (c)), both have nearly the same range of step height and

terrace width. In the case of 10° beveled substrates in figure 6.23 (a) and (b) the dominant effect is believed to be the non-uniform plasma-substrate interaction because of the sloped top surface of the diamond substrate. Again, it shows that up to 5° for these 3.5x3.5 mm substrates the effect of such non-uniformity is not that severe. One can also notice that although figures 6.22 (b) and 6.23 (b) represents growth on same kind of substrates (5° and 10° [110] bevel direction cut) however the result is very different. The 10° offcut growth (Fig. 6.23 (b)) doesn`t clearly follow any strong direction of lateral growth, whereas the 5° offcut (Fig. 6.22 (b)) shows a clear directional orientation of the step flow. The non-uniform plasma coverage might have affected the 10° [110] direction bevel as it could have done for the [100] direction 10° bevel growth (Fig. 6.23 (a)), which makes the current growth condition non-favorable for 10° or higher bevel cut in any direction.

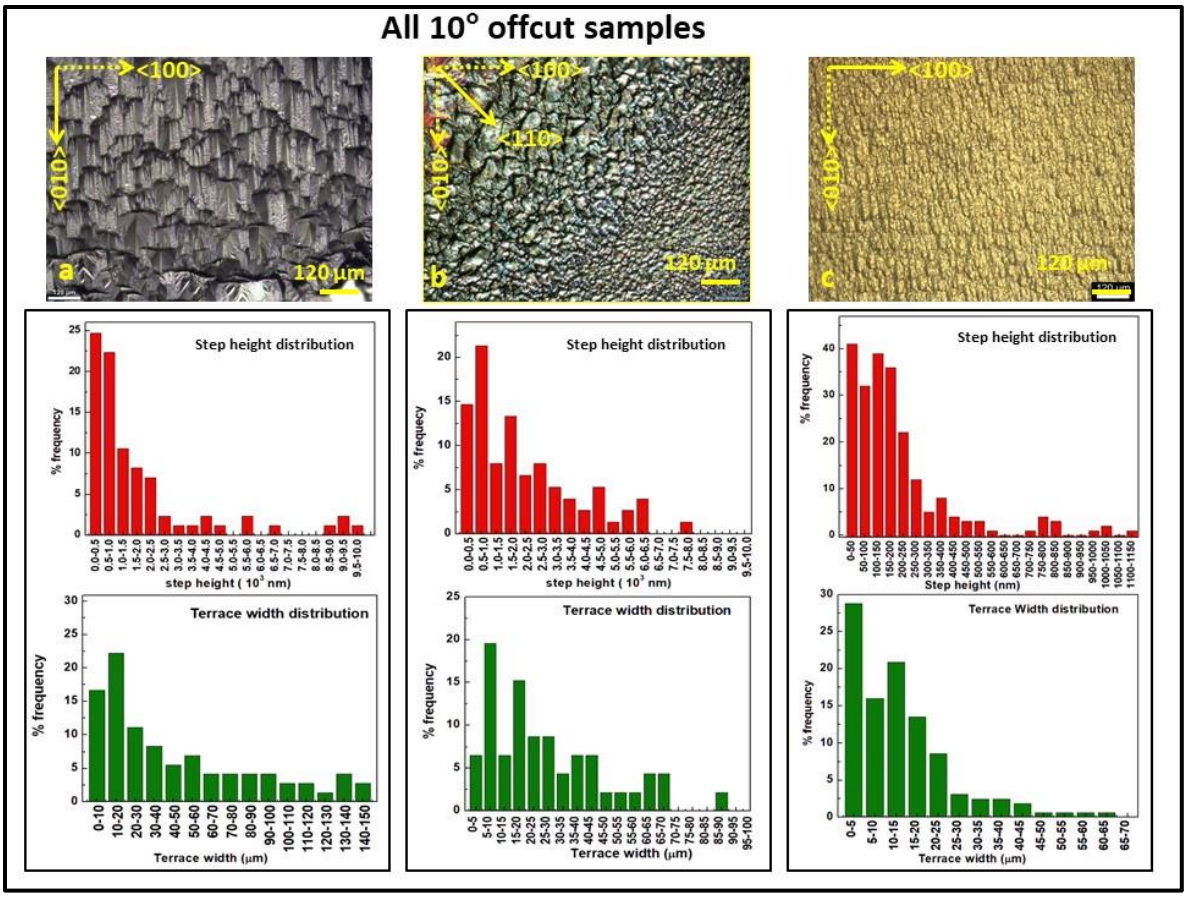

Figure 6.23. Step-terrace structures and their distributions (bar diagrams) for 10° offcut (a) (100) bevel (b) (110) bevel and (c) (100) parallel substrate thick growth

Finally, all the average step height and terrace width values for different depositions are listed in table 6.2. For the 2.5 ° offcut case, the [110] bevel and [100] parallel substrate experiments were not conducted since the 5° experiments for the different cases showed little difference. Both [100] and [110] bevel directions for the 10° offcut substrates ended up having very rough surfaces with mean step heights of 1~3 µm. Also, these two surfaces had long terraces. The terrace width also depends on the duration of growth, as it is seen that all of the 24 hr grown substrates have average terrace width ~10 µm. Overall in the current growth conditions, 5°offcut substrates show smoother surfaces (as step heights are generally less than 400 nm). The longer terrace width is an indication of lateral growth; however, accumulation of more micro steps decides whether it will

be rougher or smoother, which happened for the 10° bevel growths. Also, the numbers suggest that [110] bevel direction growth comes with slightly more surface roughness as compared to [100] bevel direction growth. The 5° and 10° parallel substrates grown samples (Figs. 6.22 (c) and 6.23 (c)) do not show any major differences in terms of the numbers and are relatively smooth.

Table 6.2. Average step height and terrace width distribution for different offcut growth

Offcut type & angle / **Growth durations**		**2.5°**	**5°**	**10°**
[100] bevel /2.5 hr	Step height	24 nm	8 nm	261 nm
	Terrace width	6.8 μm	5.6 μm	5.8 μm
[100] bevel /12 hr	Step height	53 nm	26 nm	234 nm
	Terrace width	7.8 μm	5.7 μm	4.9 μm
[100] bevel /24 hr	Step height	326 nm	176 nm	1.5 μm
	Terrace width	7.3 μm	9.5 μm	40.5 μm
[110] bevel /24 hr	Step height		317.1 nm	2.2 μm
	Terrace width		10.6 μm	27.1 μm
[100] parallel /24 hr	Step height		181.4 nm	202.6 nm
	Terrace width		14.8 μm	13.1 μm

Chapter 7. Conclusions and future directions

In first part of this work, the performance of detectors made of single crystal diamonds were tested by irradiating them with swift heavy ion (SHI) beams. These beams consisted of energetic ions from heavy nuclei with energy in the range of 100-150 MeV/nucleon. In such a harsh environment, established Si based detector technology will not survive for long when exposed to high fluence, hence diamond is a better choice as a detector material in such cases due to its outstanding material capability.

7.1. Conclusions

In this work we have looked into how gradual degradation of single crystal diamond happens while interacting with SHI beams. The generated response in the material to high energy particles is converted into a readable voltage through an external electrical circuit. A signal strength (amplitude) drop was observed versus particle fluence for detectors made from both commercial and MSU lab grown diamond. The major conclusions made from the degradation measurements are;

- The percentage of amplitude drop as a function of particle fluence followed a standard parametric equation (hyperbolic) of the same nature that followed the distribution of CCD vs particle fluence, proposed by the RD42 group [3].
- After irradiating with particle fluence up to 3×10^{13}/ cm^2 the detectors made of MSU lab grown diamond still retained 55% of the initial signal (amplitude) strength.

Post irradiation the diamond-based detectors were analyzed by their transient current response, where the charge transport of the lightly and heavily irradiated segments were compared. As a

standard reference the response of a commercially available non-irradiated electronic grade sample was used. The key observations made from this section are,

- The lightly irradiated and heavily irradiated segments of the commercial diamonds showed nearly the same charge drift time, however the amplitude of the transient current signals were slightly lower in the heavily irradiated segment.
- The carrier lifetime dropped to almost 40-60% in the heavily irradiated segment as compared to the lightly irradiated segment. This could be due to vacancies or traps created by the irradiation in that region of the diamond. No significant structural damage was measured. Hence it is concluded that structural damage happens at even higher fluence levels. It is also concluded that the performance degradation is mainly due to the creation of vacancies/traps.
- A measurement of dark current or leakage current showed that the leakage current is on the order of 10^{-12}A within the range of applied voltage ± 400 V. However, a non-linear rise in the current takes place above +400V. This behavior appears to be similar to leakage current observed for polycrystalline based pixel detectors. The non-linear rise could happen due some dislocation defects in the diamond.
- It was also observed that the leakage current varied in the presence of light from a red LED placed on top of the detector. In all the tests, a transient response occurred when the red LED was turned on i.e. there was a quick rise of the current which slowly decayed back to a normal value. The transient response decayed faster in the heavily irradiated segment than compared to the lightly irradiated segment. This could be possibly due to the presence of more charge traps/ vacancies present in the heavily irradiated segment.

To have any idea of degradation in terms of optical properties or structural in the irradiated samples, their optical response (% Transmission or absorbance) were measured by UV-Vis and FTIR spectroscopy. Generally, a type IIA single crystal diamond shows nearly 70% transmission in the visible and partly into the UV range other than a strong transition at the bandgap energy near 225 nm.

- As found from the % Transmission curve of both heavily irradiated segments, a strong absorption is found around 350 nm, which is due to formation of color centers in the diamond.
- None of these irradiated diamonds showed any additional absorption peaks in infrared region, other than the characteristic sp^3 peaks.

Further the samples were characterized in high resolution XRD (HRXRD) and Raman spectroscopy to understand if there had been any indication of structural damage in the samples. For HRXRD, any change in the (004) peak position could be related to as the onset of structural swelling or damage. As per our observations made in this section,

- There had been no appreciable change in the (004) peak position while measured across different spots in the lightly and heavily irradiated segments of the beam irradiated diamond plates. However, within the resolution of the beam spot dimension, a marginal increase in the full width half maximum (FWHM) of the (004)] peak was noticed in the heavily irradiated segment. However, this requires further investigation by adjusting to a better collimation in the X-ray source side to measure a smaller beam spot.
- For Raman spectroscopy, the initial state of a lab grown diamond was a strong 1332 cm^{-1} peak and some additional peaks around 1430 cm^{-1} and close to 1750 cm^{-1}. The peak around 1400 cm^{-1} could have appeared from some defective phases formation at the early stage of

CVD growth (also observed at polycrystalline CVD). There is another around either 1730 cm^{-1} or 1755 cm^{-1}. Any peak present in the first position is due to C=O peak which might have become stretched [136]. Any peak in the second position normally happens due to any defect during ion implantation process, however second case has almost very remote chance.

An overall observation from this work is that the MSU lab grown diamonds had higher nitrogen impurities than suitable for this detector application. Therefore, it was difficult to study the transient current response in these samples. Most of the generated charges got trapped resulting in a narrow transient current signal width. Therefore, for lab grown diamonds at MSU to be applicable for detector operation, the growth needs to be done in a lower nitrogen impurity environment. Hence for further growth of substrates for detectors, a reactor that has a very low external leakrate (30~40 mTorr/week) was selected and diamond was deposited. Some of the major outcomes from this section of the work are;

- It is extremely difficult to grow a scd layer on a substrate which has its top growth surface orientation very close to [001] crystallographic plane. Defects from dislocations and twinnings propagate perpendicularly and end up showing on the final layer as pyramidal structures and/or defects.
- Growth on misoriented substrates showed step flow growth and it allowed growth defect free thick layers of scd.
- The final surface of misoriented growth appears to have steps and terraces. Based upon the misorientation angle, methane percent, and growth temperature the step heights and terrace width will vary. In this work we studied the distribution in step height and terrace

width with varying misorientation angles from the (001) plane along the [100] and [110] directions.

- Also, it was found in literature that dopants like boron and phosphorus tend to settle and migrate to steps more than the terrace region.[137], [138]. This can lead to nonuniform doping and impurity distributions in the grown diamond. So, it may happen occasionally that, in presence of an external electric field there could be non-uniform charge transport across the sample. Especially if the terraces regions are far apart, then any device made from such layers could suffer from reduced/non-uniform breakdown voltage.

7.2. Future investigations

Electronic grade diamonds offer high charge collection efficiency and superior charge collection distance in high energy particle detectors. In order to grow the higher quality diamond the process involves optimization of different physical parameters, e.g. in the misoriented substrate process one needs to ensure that there will be reasonable vertical and lateral growth with steering of defects at the same time. Therefore, it is important to establish a systematic investigation of defect propagation with change in misoriented angle substrates. There are some limited studies already in the literature about how X-ray topography or TEM could guide such a study. However, both processes are quite complex. Hence etch-pit analysis comes as an easier solution. There are only a very few literature reports that have tried to analyze etch pit distribution with varying misorientation angle. This needs to be explored to understand how the etch pit densities change under different misorientation angle.

In terms of growing electronic grade diamond, it will be also an important study to check if the charge transport properties have any direct influence under misorientation angle. Hence one

immediate extension of this work will be to try to grow diamond for longer time to reach a point where the surface starts to appear flat, which depends upon the misorientation angle. Finally, for a superior quality of diamond, a substrate with four fold bevel cut (otherwise defined as pyramidal-shape substrate, [139] which is expected to steer the dislocations towards the edges, needs to be explored.

BIBLIOGRAPHY

BIBLIOGRAPHY

[1] https://www.puregrowndiamonds.com/blog/the-birth-of-a-diamond.

[2] R.S. Balmer, J.R. Brandon, S.L. Clewes, H.K. Dhillon, J.M. Dodson, I. Friel, et al., Chemical vapour deposition synthetic diamond: materials, technology and applications., J Phys Condens Matter. 21 (2009) 364221. doi:10.1088/0953-8984/21/36/364221.

[3] W. Trischuk, & RD42, Recent Advances in Diamond Detectors, (2008).

[4] M. ˇCerv, The ATLAS Diamond Beam Monitor, (2013).

[5] A. Oh, Diamond particle detectors systems in high energy physics, J. Inst. 10 (2015) C04038–C04038. doi:10.1088/1748-0221/10/04/C04038.

[6] D.K. Avasthi, Modification and Characterisation of Materials by Swift Heavy Ions, Defence Science Journal. 59 (2009) 401–412.

[7] Diamond Structures, Http://www.hardasrocks.info/diamond-structures.htm.

[8] J.J. Gracio, Q.H. Fan, J.C. Madaleno, Diamond growth by chemical vapour deposition, J. Phys. D, Appl. Phys. 43 (2010) 374017. doi:10.1088/0022-3727/43/37/374017.

[9] NRC: Radiation Basics, Radiation Basics, United States Nuclear Regulatory Commission. (2017). https://www.nrc.gov/about-nrc/radiation/health-effects/radiation-basics.html (accessed November 30, 2018).

[10] G.F. Knoll, Chapter 4. General properties of radiation detectors, in: Radiation Detection and Measurement , 3rd ed., 2000: pp. 103–119.

[11] Radiation Detectors and Dosimetry, http://www.physics.usyd.edu.au/super/ life_sciences/AN/AN5.pdf.

[12] Oregonstate.edu/instruct/ch374/ch418518/Chapter 18 Radiation Detectors.pdf.

[13] M. Marcel, Detectors of Radiation, oldweb.reak.bme.hu/Wigner_Course/2004/ WignerManuals/Bratislava/detectors.pdf.

[14] Interaction of radiation with matter,www.physics.edu.au/super/life-sciences/AN/AN4.pdf

[15] J.F. Ziegler, Stopping of energetic light ions in elemental matter, J. Appl. Phys. 85 (1999) 1249–1272. doi:10.1063/1.369844.

[16] T. Stefan, Interactions of Particles in Matter, S. Tavernier, ExperimentalTechniques in Nuclear and Particle Physics, 2010.

[17] The stopping of charged particles in matter, gapsing2.uniroma1.it/aschiavi/Pubblicazioni/ /PhD/Chapter_4.pdf.

[18] E. Garutti, The Physics of Particle Detectors, Lecture Notes, http://www.desy.de/~garutti/ LECTURES/ParticleDetectorSS12/L1_Introduction_HEPdetectors.pdf

[19] G.F. Knoll, Chapter 2. Radiation Interactions , in: Radiation Detection and Measurement, 3rd ed., 2000: pp. 29–57.

[20] K.A. Olive, Passage of particles through matter 1, (2014), http://pdg.lbl.gov/ 2014/ reviews/rpp2014-rev-passage-particles-matter.pdf.

[21] S. N. Ahmed, Section 2.4., Interaction of Heavy Charged Particles with Matter, in: Physics and Engineering of Radiation Detectors, 1st ed., 2007: pp. 105–121.

[22] S. Kumar, Proceedings of the DAE-BRNS Symp. on Nucl. Phys. 61 (2016)

[23] T.A. Grotjohn, J. Asmussen, Chapter 7. Microwave Plasma Assisted Diamond Film Deposition, in: J. Asmussen, D.K. Reinhard (Eds.), Diamond Films Handbook, MarcellDekker, Inc, United States of America, 2002: p. 211.

[24] C. J. H. Wort, R. S. Balmer, Diamond as an electronic material, Materials Today. 11 (2008) 22–28. doi:10.1016/S1369-7021(07)70349-8.

[25] K. E. Holbert, Radiation effects and damage, http:// holbert.faculty.asu.edu/eee560/ RadiationEfffectsDamage.pdf.

[26] D.M. Trucchi, P. Allegrini, P. Calvani, A. Galbiati, K. Oliver, G. Conte, Very Fast and Primingless Single-Crystal-Diamond X-Ray Dosimeters, IEEE Electron Device Lett. 33 (2012) 615–617. doi:10.1109/LED.2012.2185476.

[27] I. Ciancaglioni, R. Consorti, M.C. Rossi, G. Conte, Polycrystalline diamond detectors compared with silicon X-ray dosimeters for clinical use, in: IEEE Symposium Conference Record Nuclear Science 2004., IEEE, 2004: pp. 4445–4447. doi:10.1109/NSSMIC.2004.1466871.

[28] N. Tartoni, M. Angelone, M. Pillon, S. Almaviva, M. Marinelli, E. Milani, et al., X-Ray Detection by Using CVD Single Crystal Diamond Detector, IEEE Trans Nucl Sci. 56 (2009) 849–852. doi:10.1109/TNS.2008.2010705.

[29] J.W. Keister, J. Smedley, Single crystal diamond photodiode for soft X-ray radiometry, Nuclear Instruments and Methods in Physics Research Section A: Accelerators, Spectrometers, Detectors and Associated Equipment. 606 (2009) 774–779. doi:10.1016/j.nima.2009.04.044.

[30] A. Balducci, M. Bruzzi, A. De Sio, M.G. Donato, G. Faggio, M. Marinelli, et al., Diamond-based photoconductors for deep UV detection, Nuclear Instruments and Methods in Physics Research Section A: Accelerators, Spectrometers, Detectors and Associated Equipment. 567 (2006) 188–191. doi:10.1016/j.nima.2006.05.159.

[31] W. de Boer, J. Bol, A. Furgeri, S. Müller, C. Sander, E. Berdermann, et al., Radiation hardness of diamond and silicon sensors compared, Phys. Stat. Sol. (a). 204 (2007) 3004–3010. doi:10.1002/pssa.200776327.

[32] J.W. Tsung, M. Havranek, F. Hügging, H. Kagan, H. Krüger, N. Wermes, Signal and noise of diamond pixel detectors at high radiation fluences, J. Inst. 7 (2012) P09009–P09009. doi:10.1088/1748-0221/7/09/P09009.

[33] H. Kagan, Recent advances in diamond detector development, Nuclear Instruments and Methods in Physics Research Section A: Accelerators, Spectrometers, Detectors and Associated Equipment. 541 (2005) 221–227. doi:10.1016/j.nima.2005.01.060.

[34] H. Kagan, Diamond radiation detectors may be forever!, Nuclear Instruments and Methods in Physics Research Section A: Accelerators, Spectrometers, Detectors and Associated Equipment. 546 (2005) 222–227. doi:10.1016/j.nima.2005.03.128.

[35] W. Adam, W. de Boer, E. Borchi, M. Bruzzi, C. Colledani, P. D'Angelo, et al., Radiation hard diamond sensors for future tracking applications, Nuclear Instruments and Methods in Physics Research Section A: Accelerators, Spectrometers, Detectors and Associated Equipment. 565 (2006) 278–283. doi:10.1016/j.nima.2006.05.127.

[36] M. Pomorski, E. Berdermann, A. Caragheorgheopol, M. Ciobanu, M. Kiš, A. Martemiyanov, et al., Development of single-crystal CVD-diamond detectors for spectroscopy and timing, Phys. Stat. Sol. (a). 203 (2006) 3152–3160. doi:10.1002/pssa.200671127.

[37] D. Asner, M. Barbero, V. Bellini, V. Belyaev, J.M. Brom, M. Bruzzi, et al., Diamond pixel modules, Nuclear Instruments and Methods in Physics Research Section A: Accelerators, Spectrometers, Detectors and Associated Equipment. 636 (2011) S125–S129. doi:10.1016/j.nima.2010.04.096.

[38] A. Stolz, M. Behravan, M. Regmi, B. Golding, Heteroepitaxial diamond detectors for heavy ion beam tracking, Diamond and Related Materials. 15 (2006) 807–810. doi:10.1016/j.diamond.2005.12.019.

[39] J. Pietraszko, T. Galatyuk, V. Grilj, W. Koenig, S. Spataro, M. Träger, Radiation damage in single crystal CVD diamond material investigated with a high current relativistic 197Au beam, Nuclear Instruments and Methods in Physics Research Section A:

Accelerators, Spectrometers, Detectors and Associated Equipment. 763 (2014) 1–5. doi:10.1016/j.nima.2014.06.006.

[40] G. García, M. Díaz-Híjar, V. Tormo-Márquez, I. Preda, O. Peña-Rodríguez, J. Olivares, Structural damage on single-crystal diamond by swift heavy ion irradiation, Diamond and Related Materials. 58 (2015) 226–229. doi:10.1016/j.diamond.2015.08.014.

[41] A. Lohstroh, P.J. Sellin, S.G. Wang, A.W. Davies, J.M. Parkin, Mapping of polarization and detrapping effects in synthetic single crystal chemical vapor deposited diamond by ion beam induced charge imaging, J. Appl. Phys. 101 (2007) 063711. doi:10.1063/1.2653669.

[42] H. Pernegger, High mobility diamonds and particle detectors, Phys. Stat. Sol. (a). 203 (2006) 3299–3314. doi:10.1002/pssa.200671404.

[43] H. Pernegger, S. Roe, P. Weilhammer, V. Eremin, H. Frais-Kölbl, E. Griesmayer, et al., Charge-carrier properties in synthetic single-crystal diamond measured with the transient-current technique, J. Appl. Phys. 97 (2005) 073704. doi:10.1063/1.1863417.

[44] J. Isberg, M. Gabrysch, A. Tajani, D.J. Twitchen, Transient current electric field profiling of single crystal CVD diamond, Semicond. Sci. Technol. 21 (2006) 1193–1195. doi:10.1088/0268-1242/21/8/035.

[45] Y. Gu, J. Lu, T. Grotjohn, T. Schuelke, J. Asmussen, Microwave plasma reactor design for high pressure and high power density diamond synthesis, Diamond and Related Materials. 24 (2012) 210–214. doi:10.1016/j.diamond.2012.01.026.

[46] P. Moritz, E. Berdermann, K. Blasche, H. Stelzer, B. Voss, Broadband electronics for CVD-diamond detectors, Diamond and Related Materials. 10 (2001) 1765–1769. doi:10.1016/S0925-9635(01)00434-4.

[47] M. Guthoff, K. Afanaciev, A. Dabrowski, W. de Boer, W. Lange, W. Lohmann, et al., Radiation damage in the diamond based beam condition monitors of the CMS experiment at the Large Hadron Collider (LHC) at CERN, Nuclear Instruments and Methods in Physics Research Section A: Accelerators, Spectrometers, Detectors and Associated Equipment. 730 (2013) 168–173. doi:10.1016/j.nima.2013.05.041.

[48] R.M. Zain, D. Maneuski, V. O'Shea, R. Bates, A. Blue, L. Cunnigham, et al., Erratum: Leakage current measurements of a pixelated polycrystalline CVD diamond detector, J. Inst. 9 (2014) E03001–E03001. doi:10.1088/1748-0221/9/03/E03001.

[49] S. Müller, W. deBoer, M. Schneider, A. Sabellek, M. Schmanau, C. Rühle, et al., Study of leakage currents in PC CVD diamonds as function of the magnetic field, Phys. Stat. Sol. (a). 206 (2009) 2091–2097. doi:10.1002/pssa.200982221.

[50] www.wardsci.com/www.wardsci.com/images/BeerLamb_Colorimeter.pdf,

[51] M.E. Thomas, W.J. Tropf, Optical Properties of diamond, Johns Hopkins APL Tech Dig. (1993).

[52] Introduction to Fourier Transform Infrared Spectrometry, https://www.labx.com/product/nicolet-ftir

[53] R. Linares, P. Doering, Properties of large single crystal diamond, Diamond and Related Materials. 8 (1999) 909–915. doi:10.1016/S0925-9635(98)00382-3.

[54] Bruker-AXS High Resolution X-ray Diffractometer, W. M. Keck Microfabrication Facility, (n.d.). https://kmf.pa.msu.edu/KMF/Equipment/equip13.asp (accessed September 27, 2018).

[55] Evaluation of the crystallinity (tilt and twist distributions) of a GaN thin film by the X-ray rocking curve method | Rigaku, (n.d.). http://www.rigaku.com/en/products/xrd/smartlab/app025 (accessed October 3, 2018).

[56] Raman Spectroscopy | Science Facts Raman Spectroscopy – Science Facts, (2017). http://www.sciencefacts.net/raman-spectroscopy.html) (accessed October 3, 2018).

[57] M.G. Donato, G. Faggio, M. Marinelli, G. Messina, E. Milani, A. Paoletti, et al., High quality CVD diamond: a Raman scattering and photoluminescence study, Eur. Phys. J. B. 20 (2001) 133–139. doi:10.1007/s100510170291.

[58] S. Prawer, R.J. Nemanich, Raman spectroscopy of diamond and doped diamond., Philos. Trans. A, Math. Phys. Eng. Sci. 362 (2004) 2537–2565. doi:10.1098/rsta.2004.1451.

[59] R. Kalish, A. Reznik, S. Prawer, D. Saada, J. Adler, Ion-Implantation-Induced Defects in Diamond and Their Annealing: Experiment and Simulation, Physica Status Solidi (a). (1999).

[60] G. Yang, K. Livingston, R. Jones, F. Klein, High resolution X-ray diffraction study of single crystal diamond radiators, Phys. Stat. Sol. (a). 209 (2012) 1786–1791. doi:10.1002/pssa.201200017.

[61] J.C. Angus, Chapter 2. A short History of Diamond Synthesis, in: J. Asmussen, D.K. Reinhard (Eds.), Diamond Films Handbook, Marcel Dekker, Inc., United States of America, 2002: p. 17.

[62] P. W. Bridgman, Synthetic Diamonds, Scientific American 193 (1955) 42-47.

[63] M. Simpson, Materials with Diamond Touch, New Sci. (1988).

[64] H.P. Bovenkerk, F.P. Bundy, H.T. Hall, H.M. Strong, R.H. Wentorf, Preparation of Diamond, Nature. 184 (1959) 1094–1098. doi:10.1038/1841094a0.

[65] W.G. Eversole, Synthesis of Diamond, 3030187, 1962.

[66] B.V. Spitsyn, Origin, State of the Art and Some Prospects of the Diamond CVD , Brazilian Journal of Physics. (2000). http://dx.doi.org/10.1590/S0103-97332000000300002 (accessed July 2, 2018).

[67] B.V. Deryagin, B.V. Spitsyn, A Technique of Diamond Growth on a Diamond Face, 339134, 1980.

[68] J.C. Angus, H.A. Will, W.S. Stanko, Growth of diamond seed crystals by vapor deposition, J. Appl. Phys. 39 (1968) 2915–2922. doi:10.1063/1.1656693.

[69] S. Matsumoto, Y. Sato, M. Kamo, N. Setaka, Vapor Deposition of Diamond Particles from Methane, Jpn. J. Appl. Phys. 21 (1982) L183–L185. doi:10.1143/JJAP.21.L183.

[70] G.-R. Lai, E.N. Farabaugh, A. Feldman, L.H. Robins, Deposition of diamond films in a closed hot filament CVD system., J Res Natl Inst Stand Technol. 100 (1995) 43–49. doi:10.6028/jres.100.004.

[71] H. Liu, D.S. Dandy, Chapter 3. Diamond CVD Techniques, in: Diamond Chemical Vapor Deposition , 1995: p. 14.

[72] http://www.chm.bris.ac.uk/pt/diamond/jamespthesis/chapter1.htm.

[73] M. Konuma, Film Deposition By Plasma Techniques, Springer-Verlag, New York, 1992.

[74] Y.F. Li, J.J. Su, Y.Q. Liu, M.H. Ding, X.L. Li, G. Wang, et al., Design of a new TM021 mode cavity type MPCVD reactor for diamond film deposition, Diamond and Related Materials. 44 (2014) 88–94. doi:10.1016/j.diamond.2014.02.010.

[75] CSIR – Central Glass & Ceramics Research Institute, 196 Raja S C Mullick Road, Kolkata, 700032, West Bengal, India, A. Mallik, Microwave plasma CVD grown single crystal diamonds – A review, J. Coat. Sci. Technol. 3 (2016) 75–99. doi:10.6000/2369-3355.2016.03.02.4.

[76] T.A. Grotjohn, J. Asmussen, Microwave plasma-assisted diamond film deposition, Diamond Films Handbook. (2002).

[77] F. Silva, K. Hassouni, X. Bonnin, A. Gicquel, Microwave engineering of plasma-assisted CVD reactors for diamond deposition., J Phys Condens Matter. 21 (2009) 364202. doi:10.1088/0953-8984/21/36/364202.

[78] M. Füner, C. Wild, P. Koidl, Novel microwave plasma reactor for diamond synthesis, Appl. Phys. Lett. 72 (1998) 1149–1151. doi:10.1063/1.120997.

[79] J.E. Butler, Y.A. Mankelevich, A. Cheesman, J. Ma, M.N.R. Ashfold, Understanding the chemical vapor deposition of diamond: recent progress., J Phys Condens Matter. 21 (2009) 364201. doi:10.1088/0953-8984/21/36/364201.

[80] M. Schwander, K. Partes, A review of diamond synthesis by CVD processes, Diamond and Related Materials. 20 (2011) 1287–1301. doi:10.1016/j.diamond.2011.08.005.

[81] A. Gicquel, K. Hassouni, F. Silva, J. Achard, CVD diamond films: from growth to applications, Current Applied Physics. 1 (2001) 479–496. doi:10.1016/S1567-1739(01)00061-X.

[82] R.A. Khmelnitskiy, Prospects for the synthesis of large single-crystal diamonds, Phys.-Usp. 58 (2015) 134–149. doi:10.3367/UFNe.0185.201502b.0143.

[83] T. Teraji, Chemical vapor deposition of homoepitaxial diamond films, Phys. Stat. Sol. (a). 203 (2006) 3324–3357. doi:10.1002/pssa.200671408.

[84] J.E. Butler, R.L. Woodin, Thin film diamond growth mechanisms, Philos. Trans. R. Soc. Lond. A. (1993).

[85] P.K. Bachmann, H.-J. Hagemann, H. Lade, D. Leers, F. Picht, D.U. Wiechert, et al., Diamond Chemical Vapor Deposition: Gas Compositions and film Properties, MRS Proc. 339 (1994) 267. doi:10.1557/PROC-339-267.

[86] K.E. Spear, M. Frenklach, High-temperature chemistry of CVD (chemical vapor deposition) diamond growth, Pure Appl. Chem. 66 (1994) 1773–1782. doi:10.1351/pac199466091773.

[87] M. Frenklach, H. Wang, Detailed surface and gas-phase chemical kinetics of diamond deposition, Phys. Rev. B. 43 (1991) 1520–1545. doi:10.1103/PhysRevB.43.1520.

[88] D.T. Stibbe, J. Tennyson, Near-threshold electron impact dissociation of H_2 within the adiabatic nuclei approximation, New J Phys. 1 (1999) 2–2. doi:10.1088/1367-2630/1/1/002.

[89] D.T. Stibbe, J. Tennyson, Rates for the electron impact dissociation of molecular hydrogen, Astrophys. J. 513 (1999) L147–L150. doi:10.1086/311918.

[90] D.G. Goodwin, Scaling laws for diamond chemical-vapor deposition. I. Diamond surface chemistry, J. Appl. Phys. 74 (1993) 6888–6894. doi:10.1063/1.355063.

[91] D.G. Goodwin, Theory of Diamond Chemical Vapor Deposition, in: M.A. Prelas, G. Popovici, L.K. Bigelow (Eds.), Handbook of Industrial Diamonds and Diamond Films, Marcel Deker, Inc., 1998: p. 527.

[92] J.C. Angus, Diamond synthesis by chemical vapor deposition: The early years, Diamond and Related Materials. 49 (2014) 77–86. doi:10.1016/j.diamond.2014.08.004.

[93] R.M. Hazen, The Diamond Makers , Cambridge University Press, 2003.

[94] M. Kamo, Y. Sato, S. Matsumoto, N. Setaka, Diamond synthesis from gas phase in microwave plasma, J. Cryst. Growth. 62 (1983) 642–644. doi:10.1016/0022-0248(83)90411-6.

[95] Seocal | Seki-ASTeX: Diamond CVD, Carbon Nanotube, Laser Spectrometer, (n.d.). http://www.seocal.com/seki_products_detail.html (accessed July 4, 2018).

[96] S.S. Zuo, MICROWAVE PLASMA-ASSISTED CVD POLYCRYSTALLINE DIAMONDFILMS DEPOSITION AT HIGHER PRESSURE CONDITIONS, Michigan State University, 2009.

[97] J. Lu, Y. Gu, T.A. Grotjohn, T. Schuelke, J. Asmussen, Experimentally defining the safe and efficient, high pressure microwave plasma assisted CVD operating regime for single crystal diamond synthesis, Diamond and Related Materials. 37 (2013) 17–28. doi:10.1016/j.diamond.2013.04.007.

[98] K.-P. Kuo, J. Asmussen, An experimental study of high pressure synthesis of diamond films using microwave cavity plasma reactor, Diamond and Related Materials 6 (1997) 1097-1105.

[99] S.S. Zuo, M.K. Yaran, T.A. Grotjohn, D.K. Reinhard, J. Asmussen, Investigation of diamond deposition uniformity and quality for freestanding film and substrate applications, Diamond and Related Materials. 17 (2008) 300–305. doi:10.1016/j.diamond.2007.12.069.

[100] K.W. Hemawan, T.A. Grotjohn, D.K. Reinhard, J. Asmussen, Improved microwave plasma cavity reactor for diamond synthesis at high-pressure and high power density, Diamond and Related Materials. 19 (2010) 1446–1452. doi:10.1016/j.diamond.2010.07.005.

[101] S. Nad, J. Asmussen, Analyses of single crystal diamond substrates grown in a pocket substrate holder via MPACVD, Diamond and Related Materials. 66 (2016) 36–46. doi:10.1016/j.diamond.2016.03.007.

[102] S. Nad, Y. Gu, J. Asmussen, Growth strategies for large and high quality single crystal diamond substrates, Diamond and Related Materials. 60 (2015) 26–34. doi:10.1016/j.diamond.2015.09.018.

[103] S. Nad, Y. Gu, J. Asmussen, Determining the microwave coupling and operational efficiencies of a microwave plasma assisted chemical vapor deposition reactor under high pressure diamond synthesis operating conditions., Rev. Sci. Instrum. 86 (2015) 074701. doi:10.1063/1.4923092.

[104] K.W. Hemawan, INVESTIGATION OF MICROWAVE CAVITY APPLICATORS FOR PLASMAASSISTED CVD DIAMOND SYNTHESIS AND PLASMA ASSISTEDCOMBUSTION, Doctoral dissertation, Michigan State University, 2010.

[105] J. Asmussen, Y. Gu, T.A. Grotjohn, MICROWAVE PLASMA REACTORS, PCT/US12/37555, 2013.

[106] Y. Gu, THE NEW GENERATION MICROWAVE PLASMA ASSISTED CVD REACTOR FOR DIAMOND SYNTHESIS , Doctoral dissertation, Michigan State University, 2011.

[107] J. Lu, SINGLE CRYSTAL MICROWAVE PLASMA ASSISTED CHEMICAL VAPORDIAMOND SYNTHESIS AT HIGH PRESSURES AND HIGH POWERDENSITIES, Doctoral dissertation, Michigan State Universty, 2013.

[108] S. Nad, GROWTH AND CHARACTERIZATION OF LARGE, HIGH QUALITY SINGLE CRYSTAL DIAMOND SUBSTRATES VIA MICROWAVE PLASMA ASSISTED CHEMICAL VAPOR DEPOSITION, Doctoral dissertation, Michigan State University, 2016.

[109] N. Tatsumi, K. Ikeda, H. Umezawa, S. Shikata, Development of Diamond Schottky Barrier Diode, SEI Technical Review 68 (2009) 54-61.

[110] W. Müller-Sebert, E. Wörner, F. Fuchs, C. Wild, P. Koidl, Nitrogen induced increase of growth rate in chemical vapor deposition of diamond, Appl. Phys. Lett. 68 (1996) 759–760. doi:10.1063/1.116733.

[111] C.-S. Yan, Y.K. Vohra, H.-K. Mao, R.J. Hemley, Very high growth rate chemical vapor deposition of single-crystal diamond., Proc. Natl. Acad. Sci. USA. 99 (2002) 12523–12525.

[112] H. Watanabe, S.-G. Ri, S. Yamanaka, D. Takeuchi, H. Okushi, High-Quality Homoepitaxial Diamond Film Growth, (n.d.).

[113] H. Watanabe, D. Takeuchi, S. Yamanaka, H. Okushi, K. Kajimura, T. Sekiguchi, Homoepitaxial diamond film with an atomically flat surface over a large area, Diamond and Related Materials. 8 (1999) 1272–1276. doi:10.1016/S0925-9635(99)00126-0.

[114] Takeuchi, Watanabe, Yamanaka, Okushi, Kajimura, Defects in Device Grade Homoepitaxial Diamond Thin Films Grown with Ultra-Low CH4/H2 Conditions by Microwave-Plasma Chemical Vapor Deposition, (n.d.).

[115] T. Tsuno, T. Imai, N. Fujimori, Twinning structure and growth hillock on diamond (001) epitaxial film, Jpn. J. Appl. Phys. 33 (1994) 4039–4043. doi:10.1143/JJAP.33.4039.

[116] T. Bauer, M. Schreck, H. Sternschulte, B. Stritzker, High growth rate homoepitaxial diamond deposition on off-axis substrates, Diamond and Related Materials. 14 (2005) 266–271. doi:10.1016/j.diamond.2004.10.043.

[117] M.P. Gaukroger, P.M. Martineau, M.J. Crowder, I. Friel, S.D. Williams, D.J. Twitchen, X-ray topography studies of dislocations in single crystal CVD diamond, Diamond and Related Materials. 17 (2008) 262–269. doi:10.1016/j.diamond.2007.12.036.

[118] N. Tsubouchi, Y. Mokuno, Microstructures of threading dislocation bundles included in CVD homoepitaxial diamond plates, Diamond and Related Materials. 78 (2017) 44–48. doi:10.1016/j.diamond.2017.07.007.

[119] N. Tsubouchi, S. Shikata, Evaluation method for grown-in dislocations in CVD single crystal diamond using plasma surface treatment, Jpn. J. Appl. Phys. 53 (2014) 068010. doi:10.7567/JJAP.53.068010.

[120] O.A. Ivanov, A.B. Muchnikov, V.V. Chernov, S.A. Bogdanov, A.L. Vikharev, J.E. Butler, Experimental study of hydrogen plasma etching of (100) single crystal diamond in a MPACVD reactor, Mater Lett. 151 (2015) 115–118. doi:10.1016/j.matlet.2015.03.073.

[121] A. Tallaire, M. Kasu, K. Ueda, T. Makimoto, Origin of growth defects in CVD diamond epitaxial films, Diamond and Related Materials. 17 (2008) 60–65. doi:10.1016/j.diamond.2007.10.003.

[122] A. Tallaire, T. Ouisse, A. Lantreibecq, R. Cours, M. Legros, H. Bensalah, et al., Identification of dislocations in synthetic chemically vapor deposited diamond single crystals, Cryst. Growth Des. 16 (2016) 2741–2746. doi:10.1021/acs.cgd.6b00053.

[123] Takeuchi, Watanabe, Yamanaka, Okushi, Kajimura, Homoepitaxial diamond films grown by step-flow mode in various misorientation angles of diamond substrates, (n.d.).

[124] T. Tsuno, H. Shiomi, Y. Kumazawa, S. Shikata, S. Akai, Growth rate and surface morphology of diamond homoepitaxial films on misoriented (001) substrates, Jpn. J. Appl. Phys. 35 (1996) 4724–4727. doi:10.1143/JJAP.35.4724.

[125] N. Lee, A. Badzian, Effect of methane concentrations on surface morphologies and surface structures of (001) homoepitaxial diamond thin films, Appl. Phys. Lett. 67 (1995) 2011–2013. doi:10.1063/1.114770.

[126] W. J. P. van Enckevort, Janssen, Schermer, Giling, Step-related growth phenomena on exact and misoriented {001} surfaces of CVD-grown single-crystal diamonds, Diamond and Related Materials 4 (1995) 250-255.

[127] F.K. de Theije, J.J. Schermer, W.J.P. van Enckevort, Effects of nitrogen impurities on the CVD growth of diamond: step bunching in theory and experiment, Diamond and Related Materials. 9 (2000) 1439–1449. doi:10.1016/S0925-9635(00)00261-2.

[128] F. Silva, X. Bonnin, J. Achard, O. Brinza, A. Michau, A. Gicquel, Geometric modeling of homoepitaxial CVD diamond growth: I. The {100}{111}{110}{113} system, J. Cryst. Growth. 310 (2008) 187–203. doi:10.1016/j.jcrysgro.2007.09.044.

[129] A. Tallaire, J. Barjon, O. Brinza, J. Achard, F. Silva, V. Mille, et al., Dislocations and impurities introduced from etch-pits at the epitaxial growth resumption of diamond, Diamond and Related Materials. 20 (2011) 875–881. doi:10.1016/j.diamond.2011.04.015.

[130] Optical Microscope – Nikon Eclipse ME600 | PoliFAB, (n.d.). http://www.polifab.polimi.it/equipments/nikon-eclipse-me600-optical-microscope/ (accessed October 3, 2018).

[131] A. Chayahara, Y. Mokuno, Y. Horino, Y. Takasu, H. Kato, H. Yoshikawa, et al., The effect of nitrogen addition during high-rate homoepitaxial growth of diamond by microwave plasma CVD, Diamond and Related Materials. 13 (2004) 1954–1958. doi:10.1016/j.diamond.2004.07.007.

[132] N. Lee, A. Badzian, A study on surface morphologies of (001) homoepitaxial diamond films, Diamond and Related Materials. 6 (1997) 130–145. doi:10.1016/S0925-9635(96)00698-X.

[133] M.P. Everson, M.A. Tamor, Investigation of growth rates and morphology for diamond growth by chemical vapor deposition, J Mater Res. 7 (1992) 1438–1444. doi:10.1557/JMR.1992.1438.

[134] R.M. Silver, J.A. Soons, J.F. Song, A.X. Zheng, T. Brian Renegar, T.V. Vorburger, NIST SURFACE ROUGHNESS AND STEP HEIGHT CALIBRATIONS, Measurement Conditions and Sources of Uncertainty , (n.d.).

[135] Veeco Dektak 6M Profilometer, https://www.cnfusers.cornell.edu/sites/default/files/Equipment-Resources/Veeco%20Dektak%206M%20protocol%20102011.pdf (accessed December 12, 2018).

[136] A.M. Zaitsev, 4.2. Raman Scattering , in: Optical Properties of Diamond, A Data Handbook, 2001: pp. 69–131.

[137] M. Ogura, H. Kato, T. Makino, H. Okushi, S. Yamasaki, Misorientation-angle dependence of boron incorporation into (001)-oriented chemical-vapor-deposited (CVD) diamond, J. Cryst. Growth. 317 (2011) 60–63. doi:10.1016/j.jcrysgro.2011.01.010.

[138] M.A. Pinault-Thaury, T. Tillocher, D. Kobor, N. Habka, F. Jomard, J. Chevallier, et al., Phosphorus donor incorporation in (100) homoepitaxial diamond: Role of the lateral growth, J. Cryst. Growth. 335 (2011) 31–36. doi:10.1016/j.jcrysgro.2011.06.007.

[139] A. Tallaire, J. Achard, O. Brinza, V. Mille, M. Naamoun, F. Silva, et al., Growth strategy for controlling dislocation densities and crystal morphologies of single crystal diamond by using pyramidal-shape substrates, Diamond and Related Materials. 33 (2013) 71–77. doi: 10.1016/j.diamond.2013.01.006.